Imaging of Temperature Variations in the Near-Wall Region of an Optical Reciprocating Engine using Laser-Induced Fluorescence

by

Mohammad Alzuabi

A dissertation submitted in partial fulfillment
of the requirements for the degree of
Doctor of Philosophy
(Mechanical Engineering)
in the University of Michigan
2020

Doctoral Committee:

Professor Volker Sick, Chair
Professor Luis P. Bernal
Professor Andre L. Boehman
Dr. David L. Reuss

Mohammad Alzuabi

malzuabi@umich.edu

ORCID iD: 0000-0002-3287-5229

Dedication

To my dear family and friends.

Acknowledgements

I wish to express my sincere appreciation to my academic advisor, Professor Volker Sick, for his continuous support, patience, and guidance during my graduate studies. I am forever grateful to him for giving me this opportunity that pushed my intellectual limits and personal growth far beyond what I first imagined. I would like to acknowledge Dr. David Reuss for refining my engineering skills through many inspirational discussions that were essential to the progress of my experimental work. I would like to thank both Professor Andre Boehman and Professer Luis Bernal for their valuable feedback and comments throughout the course of this project.

This work would not have been possible without the support of my colleagues at the Quantitative Laser Diagnostics Laboratory (QLDL). I was so fortunate to work beside Dr. Peter Lillo, Dr. Philipp Schiffmann, Dr. Mark Greene, Martin Lichtl, Dr. Ivan Tibavinsky, Dr. Ahmet Mazacioglu, Dr. Hao Chen, Dr. Michael Gross, Dr. Fahad Alzahrani, Lucca Henrion, Angela Wu, Allison Gibson, and James Elkins. I very much appreciate their assistance and encouragement.

I would like to acknowledge the financial support from Kuwait University that allowed me to pursue my graduate studies in experimental thermal and fluid science while covering my tuition and stipend. This work was also partially funded by Kuwait Foundation for the Advancement of Sciences (KFAS) under project code CB18-65EM-01.

Last but not least, I would like to thank my dear family and friends for their unparalleled love, help and support. This journey would not have been possible if not for them, and I dedicate this milestone in my life to them.

Table of Contents

List of Tables

List of Figures

Abstract

Understanding engine heat transfer can enable the design of more efficient engines with advanced operational strategies that reduce net carbon emissions. However, accurate predictions of in-cylinder heat transfer processes require a significant investigation into the transient thermal boundary layer effects within the near-wall region (NWR). This work investigates the development of thermal stratification at two measurement locations near the cylinder head surface of an optical reciprocating engine using laser-induced fluorescence (LIF). Temperature images are obtained from high-speed toluene LIF measurements using the one-color detection technique, and the calibration procedure is based on predicted in-cylinder temperature from an engine simulation software (GT-Power). Precision uncertainty is assessed within a 1 x 1 mm^2 calibration region, and found to be within ±2 K. First measurements examine temperature variations within a 20 x 12 mm^2 field-of-view that includes the cylinder head and the piston top surfaces under motored operating conditions, while a second set of measurements examine temperature variations within an 8 x 6 mm^2 field-of-view at the cylinder head surface under motored and fired operating conditions and at two different engine speeds. The near-wall temperature measurements of this work provide unique insights into the spatial and temporal temperature variations in the NWR of an optical reciprocating engine, which were enabled by a rigorous experimental effort and attentive post-processing steps to quantitatively process the LIF images to yield temperature fields. These measurements add to continuous effort to extend the fundamental understanding of near wall engine heat transfer, and aid in achieving a more comprehensive characterization of the NWR by

complementing previously-collected near wall velocity measurements and a parallel effort in Large Eddy Simulations (LES) that focus on wall heat transfer. Future work should address improvements to the experimental methodology to better resolve the region within 0.5 mm from the surface, and perform simultaneous velocity field and surface temperature imaging to fully quantify turbulent heat fluxes, which are critical to understand heat transfer under transient high-pressure, high-temperature conditions.

Chapter 1 Introduction

The dissertation at hand addresses the need for characterizing near-wall heat transfer in internal combustion (IC) engines in order to enable the implementation of advanced combustion strategies. Chapter 1 presents the basic background for this research need, and provides an overview on this experimental effort.

1.1 Background and Motivation

The invention of the internal combustion (IC) engine at the end of the 19th century has transformed the fields of power, propulsion, and energy in a way that altered most means of transportation. Nowadays, transportation is one of the largest consumers of energy, accounting for most use of petroleum worldwide. Most of the transportation energy is derived from combustion in gasoline engines, Diesel engines, and jet turbines, and it is consuming millions of gallons of petroleum each minute of the day. This widespread application of IC engines in power generation and transportation has introduced many pressing issues of air pollution and fuel cost, which have led to significant efforts dedicated to tightening global emission standards and mandating minimum fuel economy requirements for automobile manufacturers.

Needless to say, improving the efficiency of engines is a subject of extreme importance. IC engines will continue to dominate the fleet for decades, and improving their efficiency is critical to meeting the fuel economy and emission standards. More efficient engines consume less fuel, and emit less pollutants. One primary direction to improve the efficiency of IC engines is through

advanced combustion strategies. However, designing engines to run more efficiently requires a vastly improved understanding of numerous physical and chemical processes within engines.

The next-generation of IC engines are projected to be very lean, low-temperature combustion. Compared to current engines, combustion processes in next-generation engines are likely to be characterized by much higher pressures, lower temperatures, and higher levels of dilution and/or excess air. Combustion processes under these ragged-edge conditions are unknown to a profound extent. Furthermore, the combination of unexplored thermodynamic environments and uncharted physical and chemical fuel properties results in complex interactions that are also poorly understood even at a fundamental level.

This calls for extending the current understanding of the fundamentals of such combustion systems, which requires better investigative diagnostics capabilities in order to provide new insights of the combustion process. Additionally, this extended understanding would support the development of predictive simulation tools, and accelerate the implementation of the next-generation engines of high-efficiency and low-emissions. Being able to do predictive simulations on the combustion process of these advanced strategies would allow engineers to get near that full potential of combustion within IC engines.

Significant opportunities exist for improving IC engines. Advanced combustion strategies, such as the various low-temperature combustion (LTC) modes are being researched as feasible solutions to achieve increased fuel efficiency without producing harmful emissions. LTC engines burn cool enough (low flame temperature) and lean enough (low equivalence ratio) to stay out of the high soot and NO_x formation zones, as depicted in Figure 1-1, while maintaining higher thermal efficiency.

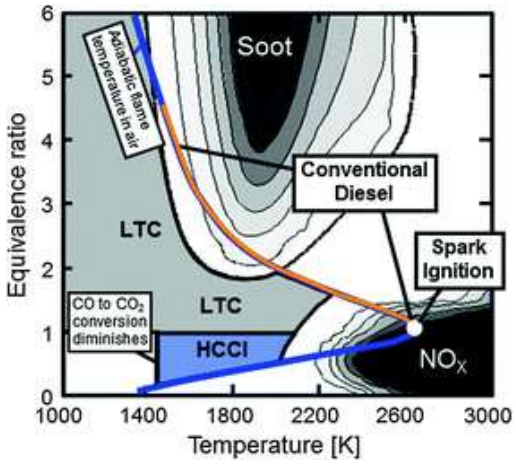

Figure 1-1. Soot and NO_x formation zones relation to flame temperature and equivalence ratio [1].

In recent decades, different engine strategies have been employed to reduce exhaust emissions and to enhance thermal efficiency, with many collaborative efforts to investigate the performance, emission and combustion characteristics of LTC modes engines. The LTC can be achieved by various combustion modes like partially premixed LTC (PPLTC), homogeneous charge compression ignition (HCCI), premixed charge compression ignition (PCCI), reactivity controlled compression ignition (RCCI), high-efficiency clean combustion (HECC) and stratification charge compression ignition (SCCI) [2].

However, the commercial implementation of LTC modes in engines has many significant technical challenges including unburned HC emission, lower operating range, unstable control in the start of combustion, transient output response and cycle to cycle variations [2-4]. This presents a need to investigate the fuel requirements, charge preparation methods, and the influence of operating parameters in LTC engines. Exhaust gas recirculation, variable valve timing, advanced fuel injection technologies are utilized to achieve LTC modes in IC engine to get improved outcomes, but controlling the gas temperature becomes crucially vital in attaining the desired combustion behavior.

1.2 Statement of the Problem

Lean-burn and low-temperature combustion (LTC) strategies have the potential to increase fuel economy and reduce exhaust emissions in IC engines. However, the implementation of LTC strategies in engines face several technical challenges. This include the need to extend low- and high-load limits, achieve stable combustion under fuel-lean conditions, control combustion phasing, and utilize flexible fuel mixtures. The underlying processes of these challenges are critically dependent on the in-cylinder heat losses and boundary layer effects. For instance, thermal stratification near the in-cylinder walls has a prominent effect on LTC strategies because of the strong temperature-dependence of LTC [1, 5]. Also, stratification of temperature has been indicated to be one possible way of extending the burn duration in HCCI, and thus enable higher load limits without excessive pressure derivatives [6]. Furthermore, the characterization of combustion-phasing, emissions, and pressure-rise requires accurate description of the near-wall flow structure, where the boundary layer behavior has direct influence on thermal stratification [7, 8]. It is clear that meeting the challenges of advanced combustion strategies requires a significant investigation into the heat transfer processes associated with in-cylinder near-wall region (NWR) [9].

Consequently, managing the heat transfer becomes substantially important since it directly affects the performance of compression-ignition in terms of timing and efficiency, and reducing heat losses can increase the efficiency of extracting the fuel's energy [10, 11]. However, the properties of the thermo-viscous NWR in IC engines remain poorly understood in spite of its substantial impact on the performance of IC engines [12, 13]. The continuous changes in pressure, temperature, and in-cylinder core flow within engines cause highly dynamic variations in the thermo-viscous fluid properties. And the cyclic compression, combustion, expansion, and charge

exchange in engines do not allow the development of a well-established boundary layer flow in the NWR.

To elucidate the physics of the near-wall engine heat transfer, significant advances must be made in high spatial- and temporal-resolution diagnostics to investigate the NWR within IC engines, as well as diagnostics to perform simultaneous in-situ characterization of the boundary layer flow. The impact of that research effort will be substantial on both scientific knowledge and practical technologies. Improved knowledge of the physics governing the near-wall engine heat transfer will facilitate the development of more accurate predictive near-wall models for engine heat transfer.

This dissertation addresses the need to extend the fundamental understanding of engine heat transfer, and investigates the transient thermal boundary layer flows within the NWR of an optical reciprocating engine. It provides improved quantitative characterization of wall heat transfer in engines that is necessary for the successful implementation of advanced combustion strategies.

1.3 Purpose of the Study

The overall objective is to investigate the transient thermal boundary layer structure in IC engines in order to improve the current understanding about heat transfer, thermal stratification, and unsteady effects in the near-wall region (NWR) of IC engines. An experimental investigation approach is taken to address these fundamental issues with the potential to advance modeling capabilities when combined with other approaches of physical modeling and computational analysis. The main focus is to conduct detailed temperature measurements in the near-wall region (NWR) of an operating IC engine over a range of conditions. Using this experimental data, fundamental questions regarding the boundary layer structure, unsteady effects, wall-heat-transfer,

and dynamic interaction between near-wall region and engine core can be investigated. A special interest will be paid to the prominent influence of the walls on flow and temperature variations.

1.4 Overview

Experiments were conducted in an optical four-stroke engine using advanced laser techniques and equipment that were demonstrated in the Quantitative Laser Diagnostics Laboratory (QLDL) research group. Temperature images were taken simultaneously with measurements of pressure and wall heat fluxes with crank-angle resolution including toluene Planar Laser-Induced Fluorescence (PLIF) for the temperature imaging at sub-millimeter (<500μm) spatial resolution. Special emphasis were attributed to the analysis of experimental uncertainties and comprehensive characterization of the inflow and boundary conditions to provide well-defined conditions for possible future wall-model validation.

The remainder of this thesis is organized as follows. Chapter 2 gives brief review of the importance of near-wall engine heat transfer. Chapter 3 describes the imaging diagnostic and the experimental test cell. Chapter 4 investigates thermal stratification in the NWR under motored conditions, while Chapter 5 focuses on near-wall temperature variations under motored and fired conditions at two different engine speeds. Chapter 6 gives a summary with conclusions and future considerations.

Chapter 2 Background on Engine Heat Transfer

Heat losses remain a limiting factor in improving the efficiency of internal combustion (IC) engines. Chapter 2 presents a brief background on the fundamentals of engine heat transfer and relevant topics from the boundary layer theory. It concludes with a summary of major engine heat transfer research, in addition to prior near-wall studies in IC engines.

2.1 Importance of Heat Transfer

Heat transfer plays an important role in the design and development of internal combustion (IC) engines. It affects engine performance, efficiency, and emissions. For instance, higher heat transfer from a given mass of fuel within the cylinder to the combustion chamber wall will lower the average combustion gas temperature and pressure, and reduce the work per cycle transferred to the piston. Furthermore, heat transfer between the unburned gas and the chamber walls in spark-ignition engines affects the onset of knock, which influences power and efficiency by limiting the compression ratio. Also, changes in gas temperature due to heat transfer have impact on emission formation processes. Besides, friction is affected by engine heat transfer, and factors in the coolant load. And the cylinder liner temperature governs the piston and ring lubricating oil film temperature, and hence its viscosity. Thus, there is no doubt that improving the fundamental understanding of engine heat transfer is critically important in order to advance the development of clean and efficient engines [14, 15].

Analyzing engine heat transfer processes is a major design task. The heat flux varies substantially in engines with location, where regions of the chamber that are contacted by rapidly moving high temperatures burned gases generally experiences the highest fluxes in the order of 10 MW/m^2. The peak in-cylinder burned gas temperatures are in the neighborhood of 2,500 K in spark-ignition engines, while the maximum metal temperatures for the inside of the combustion

chamber space are limited to much lower values to maintain the strength of the materials, maintain clearances, and prevent the lubricant from breaking down. Also, cooling for the cylinder head including the valves, cylinder liner, and piston must be provided, or they will melt. In addition, overheated spark plug electrodes or exhaust valves could cause knock and pre-ignition problems. Nevertheless, only as much cooling as necessary should be provided to maintain the thermal efficiency as any heat removed represents a loss of energy. Although heat losses are such a substantial part of the fuel energy input, elimination of heat losses would only allow a fraction of the heat transferred to the combustion chamber walls to be converted to useful work. The remainder would leave the engine as sensible exhaust enthalpy [14, 15].

2.2 Variations of Heat Transfer Rate

Heat transfer takes place under conditions of varying gas pressure and temperature in IC engines, where local velocities vary more or less rapidly depending on intake port and combustion chamber configuration. The rate of heat transfer continuously varies, locally and temporally, throughout the four-stroke operating cycle that are shown in Figure 2-1 for a spark-ignition engine, and the surface area of the combustion chamber varies too. The enormous variation of the in-cylinder charge temperature relative to both the wall temperature and the flow field have a major influence on heat transfer. During the intake process, the incoming charge is usually cooler than the walls and the flow velocities are high. During compression, the charge temperature rises above the wall temperature, and gas velocities decreases. Heat transfer is now from the cylinder gases to the chamber walls. During combustion, gas temperatures increase substantially, and the gas expansion, which occurs at combustion, produces increased gas motion. This is the period when heat-transfer rates to the walls are highest. Also, as the cylinder pressure rises, a small fraction of the cylinder charge is forced into crevice regions, resulting in additional heat transfer. During

expansion, gas temperatures decreases so heat-transfer rates decreases. When the exhaust valve opens, however, the blowdown process produces high velocities within the cylinder, past the exhaust valve, and in the exhaust port. Substantial heat transfer from the exhausting gases to the valve, port, and (to a lesser extent) manifold occurs during the exhaust process [14, 15].

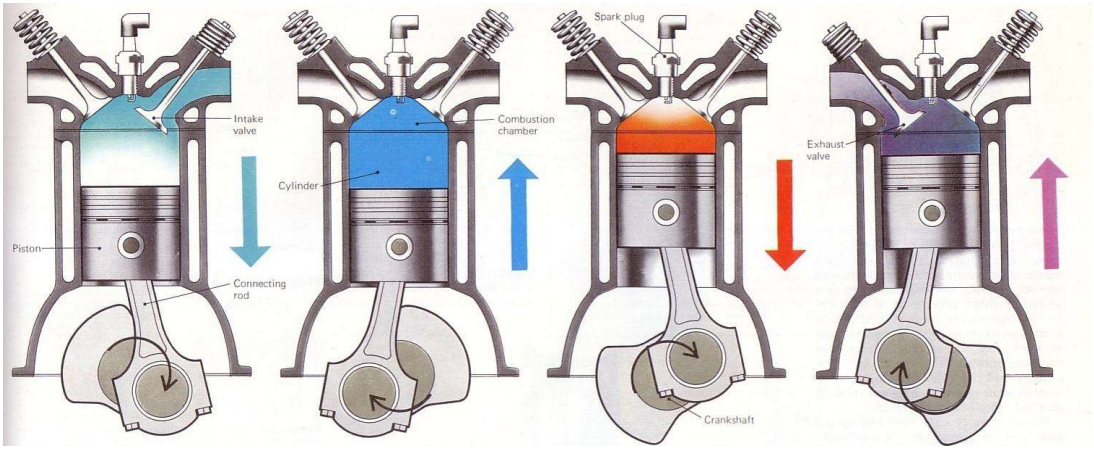

Figure 2-1. Four-stroke operating cycle of a spark-ignition engine [16].

The ability to predict the magnitude of the heat transfer between the working fluid, the walls of the intake system, combustion chamber, and exhaust system, and to the coolant is essential for engine design and development, but accurate predictions requires a deep understanding of the behavior of the boundary layer flows in IC engines that have substantial impact on heat exchange, and combustion phasing.

2.3 Modes of Heat Transfer

All modes of heat transfer are important in engines. Heat is transferred by conduction through the cylinder head, cylinder walls, and piston, and it is transferred by forced convection between the in-cylinder gases and the cylinder head, valves, cylinder walls, and piston during the engine cycle. Heat transfer by radiation occurs from the high-temperature combustion gases and the flame region to the combustion chamber walls [17].

The heat flux from the gases within the cylinder through the combustion chamber wall has both a convective and a radiation component. The importance of thermal radiation in engines has generally been ignored or assumed to be insignificant relative to convective heat transfer, but its importance in turbulent flames is being realized recently after an improved understanding that radiation is affected by turbulence in much the same way as convection [18].

2.4 Near-Wall Region (NWR)

Throughout each engine operating cycle, the heat transfer takes place under conditions of varying gas pressure and temperature resulting in continuous changes in the heat flux into all of the containing walls of the combustion chamber. And the heat flux into each wall has both convective and radiation components. It is then conducted through the wall, and convected from the wall to the coolant [19]. But the gas in the combustion chamber is in turbulent motion, and the core flow is unsteady, and often swirling and tumbling. This motion transfers heat several orders of magnitude better than molecular transport [15]. Figure 2-2 shows a qualitative picture of the near-wall region (NWR), where l is the size of a typical eddy, and u is a typical fluctuating velocity. The effective convective thermal conductivity in this case is proportional to the effective turbulent thermometric diffusivity. Because the gas is being well-mixed by turbulence, the mean temperature is expected to be fairly uniform in the chamber, except near the wall.

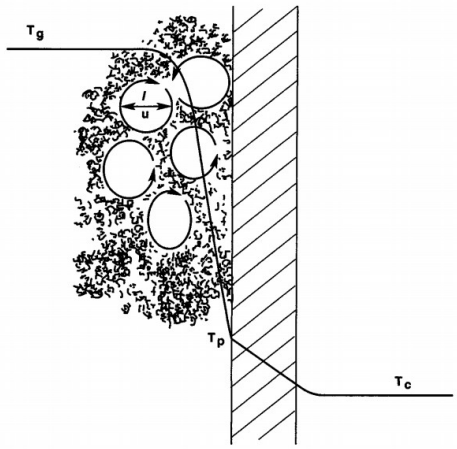

Figure 2-2. Qualitative picture of turbulent heat transfer in the cylinder [15].

The structure of the engine near-wall layers is a subject of high interest. Heat transfer from the gas side to the wall happens within the thermal boundary layer, which develops, at the wall when the surface and the fluid are at different temperatures. It is the region of the fluid where the temperature varies from the cooled wall temperature to the outer core flow temperature. And these engine near-wall layers are driven by turbulent flow in the core-region that is generated by the piston motion during the intake and compression strokes. This unsteady environment in the cylinder, in addition to the rising and falling gas temperature throughout each cycle and the erratic flame propagation direction do not allow for the development of a well-established boundary layer flow, but an unconventional one.

2.5 Boundary Layer Flows

The in-cylinder core-flow exhibits a wide range of spatio-temporal scales, as it undergoes recurring compression, combustion, expansion, and charge-exchange processes. This highly unsteady nature of in-cylinder flows, in return, affects the near-wall region (NWR) as it dynamically responds to intermittent and impulsive flow, besides pressure gradients and thermal

stratification. The boundary layer that develops at the wall within IC engines under these conditions is unconventional i.e. unlike the traditional flat plate boundary layers with a constant free-stream velocity and temperature, as seen in Figure 2-3. The incompressible boundary layer on a flat plate in the absence of a pressure gradient is usually referred to as the Blasius boundary layer. It is then important to distinguish between the boundary layer at the engine head, where it is expected to be a low-velocity and quasi-planar boundary layer of the Blasius-type, and at the cylinder side-wall, where it is oscillating because of the piston movement.

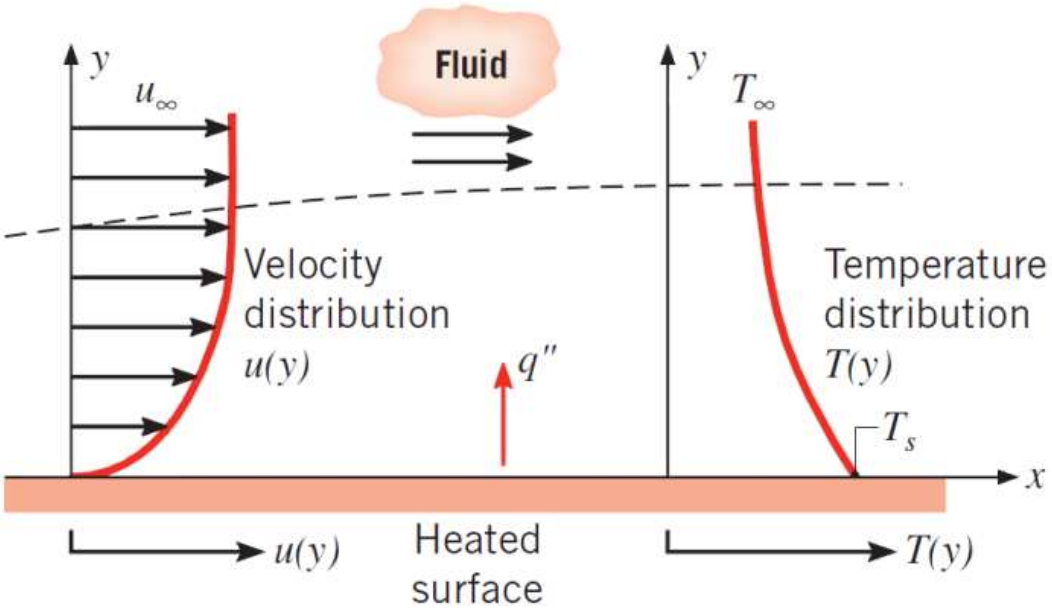

Figure 2-3. Boundary layer development in convection heat transfer [20].

Also, it is important to note the differences between laminar and turbulent boundary layers. A laminar boundary layer is characterized by non-intersecting layers, and any exchange of mass or momentum takes place between adjacent layers on a microscopic scale. On the other hand, a turbulent boundary layer is characterized by mixing across several layers on a macroscopic scale, which yields a steep gradient of velocity at the wall. Typical laminar and turbulent boundary layer profiles are shown in Figure 2-4. The primary difference is the presence of higher speed fluid close

to the surface and greater surface shear stress in the turbulent boundary layer. Laminar boundary layers are found when the Reynolds numbers are small, while turbulent boundary layers form only at larger Reynolds numbers [21].

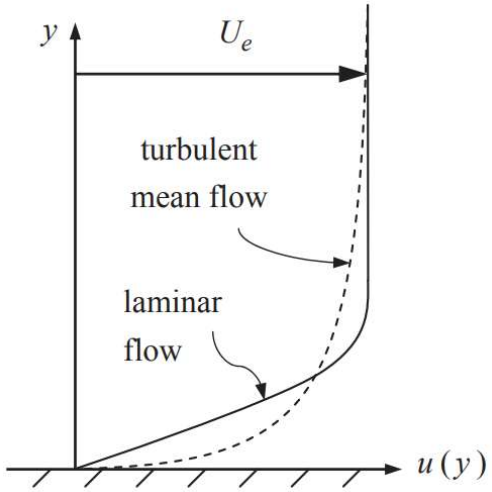

Figure 2-4. Typical velocity profiles for laminar and turbulent boundary layers [21].

A laminar flow over a flat plate is transitioned to a turbulent flow at some finite Reynolds number, as shown in Figure 2-5 -where increasing x is synonymous with increasing Reynolds number-. An initial instability appears in the laminar regime, but gets damped out by the effects of viscosity. With increasing Reynolds number, momentum overcomes the effects of viscosity causing the fluctuations to increase in strength. Following this breakdown of laminar flow through amplification of infinitesimal instabilities, the flow becomes increasingly chaotic and irregular. When the fluctuations come to their rapid growth, the flow is said to be fully turbulent. First occurrence of growth of fluctuations happens around a Reynolds number of 10^6 [21].

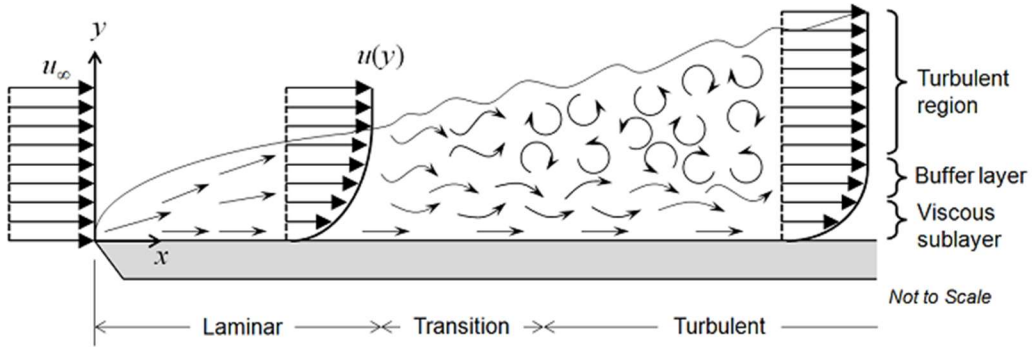

Figure 2-5. Schematic of the transition process of a fluid flow over a semi-infinite flat plate [22].

The scale of mixing in a turbulent boundary layer is on a much bigger scale compared to a laminar one. It cannot be handled by molecular viscosity alone, but also turbulence or eddy viscosity. And the turbulence dissipation usually dominates over viscous dissipation everywhere in the turbulent region, except for the viscous sublayer close to the wall, where viscous effects limit various flow quantities.

Turbulent flat plate boundary layers are often described using the law-of-the-wall, in which the turbulent flow near a flat wall can be divided into multiple regions, as shown in Figure 2-6. At the wall, the fluid velocity is zero because of the no-slip condition. In the viscous sublayer, the flow velocity is linear with distance from the wall. In the buffer layer, turbulence stresses begin to dominate over viscous stresses. In the log-wall region, the flow is fully turbulent and the average flow velocity is related to the log of the distance to the wall. And further away from the wall, the flow transitions to the free-stream region. The viscous and buffer layers are very thin, and if the distance to the end of the buffer layer is δ, then the log-law region will extend about 100δ away from the wall [22].

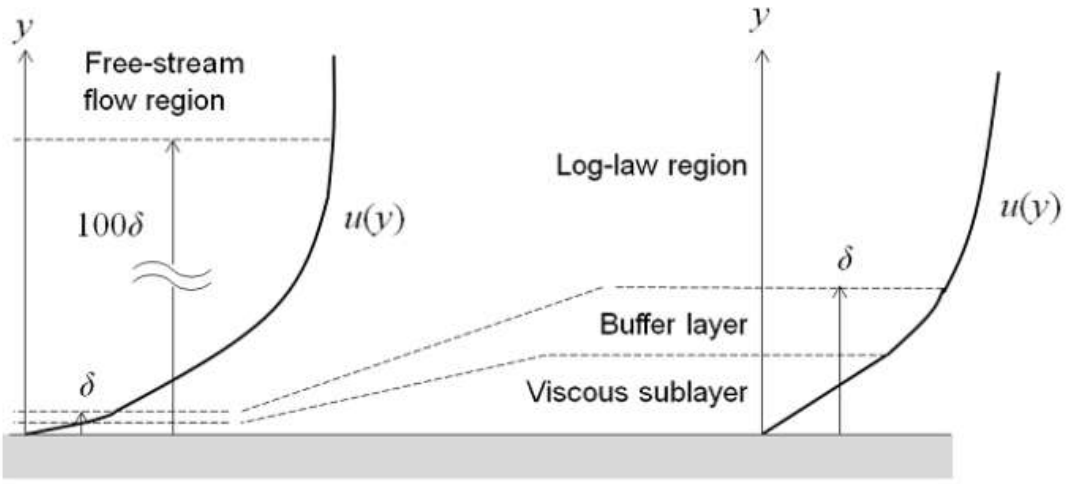

Figure 2-6. Schematic of the law-of-the-wall in the close proximty of a wall [22].

The profile of average streamwise velocity in the wall coordinates in the vicinity of a solid wall is shown in Figure 2-7. Here $u^+ = u/u_t$ and $y^+ = \frac{y\,u_t}{v}$ denote the non-dimensional velocity and normal distance from the wall, respectively. u_t denotes the friction velocity and is given as

$$u_\tau = \sqrt{\frac{\tau_w}{\rho}} \tag{2-1}$$

Here τ_w denotes the wall shear stress. In the innermost viscous layer from $y^+ = 0$ to $y^+ = 5$, the non-dimensional velocity profile varies linearly

$$u^+ = y^+ \tag{2-2}$$

From y^+ equal to 30 to nearly $\frac{y}{\delta} = 0.1$ termed as the overlap layer or logarithmic layer, the profile follows the logarithmic behavior

$$u^+ = \frac{1}{k}\, ln\, y^+ + B \tag{2-3}$$

Here k is the von Karman constant = 0.41. The profile in the outer region $\frac{y}{\delta}$ from 0.1 to 1.0 depends on the pressure gradient and Reynolds number. It may be noted that for y^+ from 5 to 30, a smooth transition between linear behaviour and logarithmic behavior is observed.

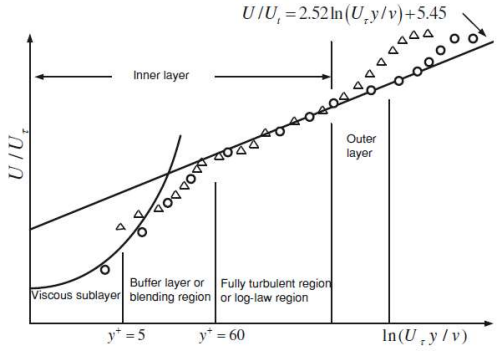

Figure 2-7. Velocity profile in the wall coordinates in the presence of a solid wall [23].

Mean temperature in the wall coordinates also behaves similar to the mean velocity, as shown in Figure 2-8. Right in the vicinity of the solid wall, the mean temperature profile is linear in the thermal sublayer:

$$T^+ = \mathrm{Pr}\, y^+ \tag{2-4}$$

Where Pr denotes the Prandtl number and T^+denotes the mean temperature in wall coordinates. It is defined as,

$$T^+ = \frac{T_w - \bar{T}}{T^*} \text{ where } T^* = \frac{q_w}{\rho\, C_p\, u_\tau} \tag{2-5}$$

Further away a logarithmic behavior is observed in the form of,

$$T^+ = \frac{Pr_t}{k}\, lny^+ + A(\mathrm{Pr}) \tag{2-6}$$

Here T^* denotes the wall conduction temperature and is equivalent of the friction velocity and denotes the mean temperature. The last term in Eq. (2-6) is a strong function of Prandtl number (Pr).

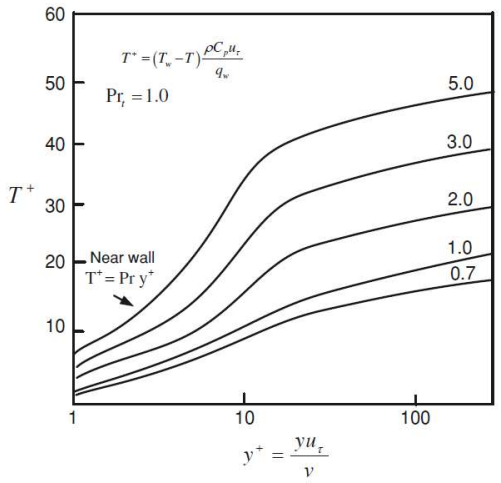

Figure 2-8. Mean temperature profile in the wall coordinates in the presence of a solid wall [23].

The law-of-the-wall has been used mostly to describe the near-wall region (NWR) for flat-plate configurations. Nevertheless, it is inadequate in describing the unsteady NWR of IC engines because it was derived for assumptions not suitable for engine flow conditions. In engines, the bulk flow outside the boundary layer is turbulent and not exclusively wall-parallel. Additionally, the hot burned gas region expands rapidly post the combustion event, and compresses the unburnt gas ahead of the flame. Hence, the compressibility effects are important to include when determining the flow properties near the wall. Moreover, the reciprocating piston motion creates a pulsatile flow. While the boundary layer is constantly restarting in some regions at the side in-cylinder walls, the one developing at the in-cylinder head is undergoing a high degree of compression by both the piston motion and flame propagation.

Boundary layer flows in engines are neither classically laminar nor wholly turbulent. Experimental studies of the near-wall region (NWR) in engines showed deviations of measured boundary layer structure form the law-of-the-wall [24-26]. Before diving into the complexity of near-wall measurements in IC engines, it is worth mentioning the steady impinging jet boundary layer for its similar engine-like physics, such as wall-normal flow.

In-cylinder boundary layers are unlike most of the canonical flows. The development of in-cylinder boundary layers are affected by free-stream vertical structures, and cannot be solely characterized by significant wall-shear generated turbulence production as most bounded turbulent flows. The investigation of in-cylinder boundary layers should consider the most relevant canonical flows to engines, which include mainly the impinging turbulent jet and the turbulent wall jet. Both of these flows exhibit some resemblance to engines boundary layers as they can also be characterized by advected turbulence entering the viscous region [27].

The near-wall region of interest in this work is adjacent to the in-cylinder head, which is most similar to the impinging jet. The steady impinging flow structure on an indefinite plate can be summarized into three regions, as shown in Figure 2-9. The free jet region is formed as the jet exits with a $V(r)$ velocity distribution, the stagnation region is formed upon jet impact and deflection, and the wall jet region is formed upon re-acceleration of the flow along the confining surface [28].

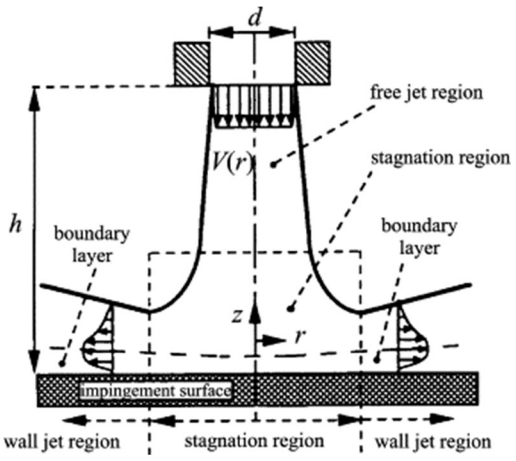

Figure 2-9. Flow regions for an impinging free-surface jet [28].

The stagnation region consists of an impingement boundary layer at the impingement surface, and an inviscid impingement region further away [29]. The inner temperature profile over the impingement plate was shown by Geurra *et al.* [30] to follow a logarithmic solution. Loureiro and Freire [29] utilized the experimental data set of Geurra *et al.* [30] to propose a Weibull distribution of the full mean temperature profile for the wall jet region, as shown in Figure 2-10.

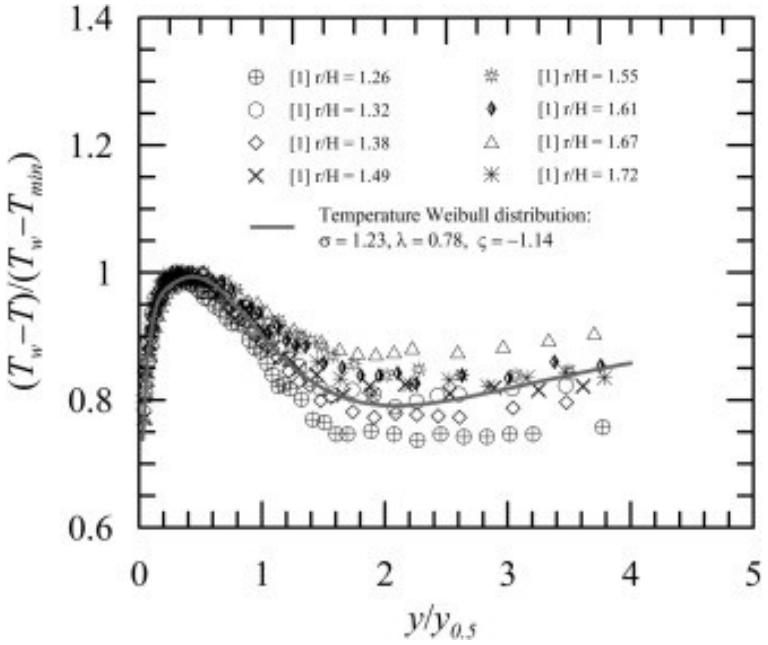

Figure 2-10. Weibull distribution for the radial mean temperature profiles of Geurra et al. [29].

The flow downstream of the stagnation region can experience growing boundary layers as they transition from being laminar near the stagnation zone to being turbulent further downstream, as shown in Figure 2-11 for a liquid jet experiment.

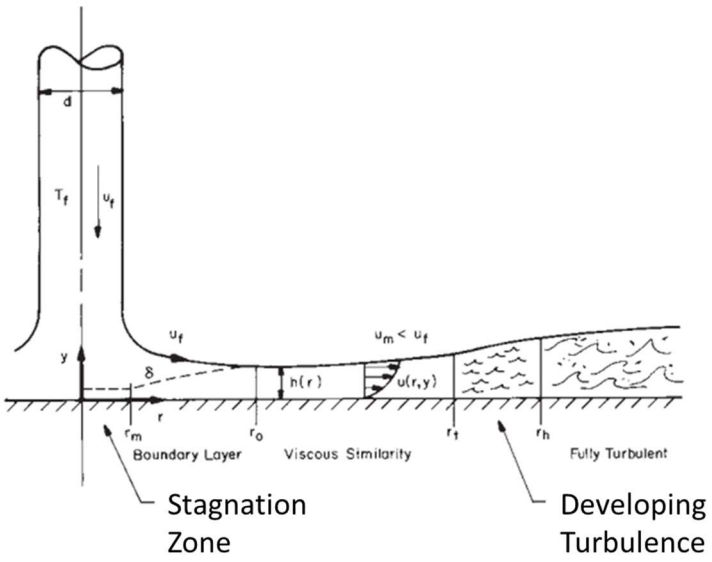

Figure 2-11. Downstream development of an axisymmetric impinging jet [31].

Research in engine in-cylinder heat transfer has gradually developed from global heat rejection studies to detailed microscopic measurements of the thermos-viscous region at the combustion chamber walls. Next sections lists the progress in engine heat transfer research.

2.6 Review of Engine Heat Transfer Research

The design and development of internal combustion (IC) engines largely depend on the ability to predict in-cylinder heat transfer processes due to their impact on performance, efficiency, and emissions [14]. This has motivated many studies to investigate engine heat transfer, which yielded significant progress in quantitative prediction tools as summarized in [12, 32].

The earliest studies utilized indicator diagrams that plot the engine P-V diagrams mechanically to investigate engine heat transfer. Janeway [33, 34] calculated the heat loss from

the cylinder by analyzing the indicator diagram. The mean bulk temperature was estimated from polytropic compression calculations, where the wall temperature was assumed. Likewise, Lanchester [35] performed similar analyses to calculate heat losses to the cooling jacket, but noted the need for higher speed diagnostics.

Subsequent studies incorporated thermocouples to directly measure wall temperatures both inside the cylinder and in the cooling channels in order to calculate the heat flux out of the cylinder. Eichelberg [36] took temperature measurements at the in-cylinder engine head walls and the piston top, and was able to calculate periodical heat flux by an empirical correlation. The Eichelberg equation was used for several decades for practical modeling of engine heat transfer because of its simplicity. However, the equation was found to be inadequate in reflecting the increased heat transfer for higher in-cylinder gas velocities. As a result, revisions were proposed by Pflaum [37-39] to increase the sensitivity of the speed-dependent term and to account for changes in the intake manifold air pressure.

The advantages of presenting correlations in terms of dimensionless groups became apparent later for scaling of engine geometry. Elser [40] used thermocouples under surfaces in two- and four-stroke diesel engines to develop his non-dimensional correlation. However, the correlation was found to only match the experimental data of the two-stroke engine. Consequently, results of heat transfer measurements that focused on total heat rejected from the engine by looking at the cooling water were presented in terms dimensionless quantities [41]. Then, Taylor *et al.* [42] combined the use of gas- and water-side thermocouples with total heat rejection measurements to obtain improved correlations of dimensionless values for the purpose of estimating engine cooling needs with greater accuracy. Oguri [36, 43] conducted experiments similar to Eichelberg's

utilizing thermocouples better-placed at the actual surface in a four-stroke SI engine, and used the data to present improvements on the Esler's dimensionless equation.

Overbye *et al.* [39, 44] utlizied these true surface thermocouples to obtain cycle-resolved measurements of gas temperature and heat flux, but with a phase-lag. The data was among the first analyzed on a digital computer, and that was a notable contribution. Taking advantage of digital computers, Williams [45] performed simulations using tabulated heat transfer coefficients versos crank-angle. McAulay [46] performed a more detailed simulation of a diesel engine using th Eichelberg formula.

Previous heat transfer models were inadequate beyond their calibration test conditions so a heat transfer correlation with improved dimensionality and physical derivation was needed. Annand [39] incorporated convective and radiative terms similar to what was presented by Chirkov and Stefanovski [47] to derive a new correlation. His work was validated through comparison to previous cycle-resolved experiments of Elser [40] and Overbye [44], in addition to time-averaged experiments by Zipkin and Sanders [48] and Ku [49]. The resulted correlation requires different constants depending on flow intensities, cycle phase, and the ignition type. Subsequently, Woschni [50] presented the most established in-cylinder heat transfer model with independent terms for the heat transfer due to piston motion, and that due to forced convection. Then, Woschni [14, 51] presented a modification to better include the effect of swirl in high swirl engines by changing the constants to become functions of the piston and swirl velocities. Decades later, Hohenberg [32, 52] proposed another modification to replace the characteristic length with the instantaneous cylinder volume instead of the bore. These proposed correlations found widespread adaption for their simplicity, relative accuracy, and universal form across engine architectures.

Unlike bulky thermocouples used in early in-cylinder temperature measurements, Annand and Ma [53] developed a technique to install thin-film surface thermocouples on any location on the head. Heat flux between these new surface thermocouples and traditional thermocouples installed on the coolant side of the head were calculated in a diesel engine. Compared to the earlier work by Annand, the developed correlation had an additional time-derivative term to account for the unsteady nature of in-cylinder heat transfer. This work advanced the technology of surface thermocouples, but the proposed model required experimentally determined engine-specific constants.

LeFeuvre *et al.* [54] presented another spatially-averaged heat transfer correlation, but stated the importance of velocity and temperature measurements within the boundary layer in order to develop physics-based boundary layer models in engines. Borgnakke *et al.* [55] continued the development of heat transfer models by including the effects of turbulence, which improved the accuracy. Borgnakke *et al.* [51] yet presented another model that showed improved accuracy over the past correlations of Woschni [50, 51], Annand and Ma [53], and Poulus [56] when compared against the experimental data of Alkidas *et al.* [57].

The spatial inhomogeneity of surface temperature and heat flux required significant effort in measuring velocity, temperature, and turbulence profiles in engines in order to enhance the understanding of the gas-side physics [12]. Hot-wire anemometry were utilized in engine studies to measure the gas velocity [58, 59]. However, they were intrusive and limited by the physical constraints in accessing the in-cylinder flow.

Nijeweme *et al.* [60] investigated unsteady in-cylinder heat transfer in a spark ignition engine using experiments and modelling. They performed instantaneous heat flux measurements in the expansion stroke to find heat flowing from the wall into the combustion chamber, even

though the bulk gas temperature is higher than the wall temperature. This led to reviewing the assumptions used in modelling the boundary layer. The discrepancies were attributed to assumptions in the law-of-the-wall and Reynolds analogy. Chang *et al.* [10] took measurements of surface temperature and heat flux at seven locations at the in-cylinder head surface and the piston top surface of an HCCI engine, and presented a modified Woschni model with an improved flame propagation term. The results showed small spatial variation that contradicted the findings of Annand and Ma [53] and LeFeuvre [54] in Diesel engines, and Alkhidas [61] in a spark-ignition (SI) engine. Cho *et al.* [62] investigated heat transfer in homogenous and stratified charges in a spark-ignition direct-injection (SIDI) engine. Larger spatial variations of heat flux was found in the stratified mode with noticeable effects of spray impingement in cooling the piston surface during late injection at high loads. Heat transfer processes in the stratified mode were less by 30% than in the homogenous charge mode. Also, the Woschni model [50] was found to better predict heat transfer in the homogenous mode, while the Hohenberg model [52] better predicted the heat transfer in the stratified mode.

Soyhan *et al.* [63] performed a comparison study between the Woschni model [50], the Hohenberg model [52], and the Chang *et al.* model [10] in predicting heat transfer for HCCI applications. The models were compared to both experimental measurements from a Ricardo HCCI engine and simulations. The combustion compression velocity term in the Woschni model was not relevant in HCCI applications, and caused unrealistically high gas velocities and overpredictions of heat transfer rates. The Chang *et al.* model underestimated heat transfer and overpredicted peak pressures. The Hohenberg model better matched the measurements and simulations because it lacked a compression velocity term. Then, Rakopoulos *et al.* [64] proposed a new heat transfer model, and included a comparison study of various models including Launder

and Spalding [65], Huh *et al.* [66], Angelberger [67], and Han and Reitz [68] to published data from spark-ignition (SI) engines [61, 69, 70], from a Diesel engine of [71], and from a motored engine [72]. The results showed limited improvement in their model, but it was applicable to both SI and Diesel engines.

Most fundamental and empirical investigations into engine heat transfer in the past were limited to providing spatially-averaged heat transfer coefficients based on single-point measurements. They lack a detailed description of local convective heat transfer, and do not accurately describe the continuous spatial and temporal variations in temperature and heat flux in the near-wall regions (NWR) [39, 50, 52, 73].

2.7 Survey of Near-Wall Studies in Engines

Accurate prediction of in-cylinder heat transfer is critically dependent on understanding the thermo-viscous boundary layer region [10, 74]. However, the near-wall flow is not fundamentally understood for IC engines, and the boundary layer flows behave quite differently from steady boundary layers. Detailed insights into the transient nature of such flows in engines have been limited by experimental techniques in the past, but recent advancements in laser technology allowed for the development of less-intrusive techniques than enabled accurate near-wall measurements.

Experiments utilizing the Doppler frequency shift of light reflected from a moving particle represented the first application of laser diagnostics to velocimetry of engine flows. However, most experiments measured only one velocity component [75-78] or at most two components [76, 79] due to the limited optical access to engines in general. These Laser Doppler velocimetry (LDV) experiments contributed only to the understanding of the bulk flow and not the flow development in the boundary layers. Hall and Bracco [80] conducted the first velocity measurements in the

boundary layer at the cylinder wall of an engine using LDV. They were able to resolve velocity profiles as close as 0.5 mm in the tangential direction. The closest measurement to the wall yielded a velocity of 90% of the free-stream. The turbulence intensity was noted to increase sharply near the wall due to presumably wall-generated turbulence.

Foster and Witze [81] employed a specially-designed engine with a toroidal shaped head in order to measure velocities with LDV as close as 60 μm from the wall. Cases of low and high swirl under motored and fired operating conditions were tested at an engine speed of 300 rpm. In the low swirl motored case, a laminar-like profiles that are 700-1000 μm thick were captured with decreasing turbulence intensity close to the wall. In the high swirl motored case, boundary layers thinner than 200 μm were found with increasing turbulence intensity near the wall. The boundary layer thickness increased under firing conditions for both low and high swirl cases due to increased viscosity from the higher gas temperatures. Also, they noted that precession of the swirl center would cause changes in the free-stream velocity and the thickness of the boundary layer. More importantly, they identified both laminar and turbulent boundary layers in an engine, but under different conditions.

In another study, Pierce *et al.* [24] recorded measurements within 50 μm of a surface protruding from an engine head that mimicked the geometry of a heat transfer probe that was previously installed in the engine. They noticed the probe volume to shift towards the surface because of the effect of index of refraction gradients, which introduced unknown errors in determining the measurement location. Additionally, they recorded the first near-wall particle image velocimetry (PIV) measurements in an engine. Their PIV measurements showed a very thin low-momentum region with a profile so different than a traditional boundary layer. They attributed this non-tradition boundary layer to fluid rotation, wall-normal flow, and the transient nature of

near-wall forcing functions. Also, their results indicated the dependence of the near-wall flow on the combustion chamber geometry, and the operating conditions.

LDV experiments investigating the boundary layer in engines provided only single-point velocity measurements, and lacked the needed instantaneous spatial information to describe the behavior of boundary layer flows. Likewise, prior PIV experiments only acquired one velocity field per an engine cycle, and did not show the temporal evolution of boundary layers. This restricted the progress in near-wall boundary layer studies in engines for a while, but then advancements in digital imaging systems offered the capability to perform high-speed imaging experiments.

Alharbi and Sick [25] conducted digital μPIV measurements in a motored pent-roof engine with flat head windows at an engine speed of 800 rpm. They found poor agreement between the experimental data and the Blasius laminar profile or the turbulent power law, but better matching the Blasius solution towards the end of the compression stroke. Subsequently, Jainski *et al.* [26] compared motored measurements taken at 400-, 800-, and 1100 rpm in the same engine with the Logarithmic Law model. Results showed poor agreement between experiments and model predictions.

Recently, Greene [82] conducted a comprehensive planar near-wall velocimetry measurements in an optical reciprocating engine. It was the first near-wall velocimetry measurements to be recorded under fired operating conditions. He conducted measurements at both the in-cylinder engine head, in addition to the piston surface, and performed experiments at engine speeds of 500 and 1300 rpm. Also, he presented a unique experimental methodology that was proven to overcome some inherent experimental challenges in near-wall measurements. His high-resolution results showed different flow types in the near-wall region (NWR) including wall-

parallel flow, impinging jet-like flows, and shear flows. The effects of inviscid compression were found to affect the wall-normal flow near the surfaces.

These near-wall μPIV measurements contributed greatly towards the development of an improved heat transfer model that included various unsteady effects, which built upon previous computational work. Chen and Veshagh [83] were among the first to build a quasi-steady boundary layer model that captures spatial and temporal changes in heat flux [32]. Their model assumed a constant boundary layer profile that follows the power law, and employed the Colburn analogy that heat transfer depends only on the thermal boundary layer and free-stream velocity.

Han and Reitz [68] developed a temperature wall-function that accounted for both the increasing turbulent Prandtl number in the boundary layer, and the variations in gas density. The results showed significant gas compressibility effects on heat transfer, and negligible unsteadiness or heat release effects. Also, they found the heat flux to the wall to be proportional to the difference of logarithms of the gas and wall temperatures rather than the arithmetic difference. Unlike these results, the multi-dimensional simulations of Franco and Martorano [84] found that heat transfer was out of phase with the gas and wall temperature difference. They identified the role of near-wall vortices on enhancing heat transfer.

Additionally, Suziki *et al.* [85] developed a heat transfer model that includes the effects of molecular transport and turbulence processes, and found similarities to the Woschni equation [32]. The turbulence intensity during the intake stroke was determined from the mean gas density and mean piston speed during the intake stroke, while the turbulence generated by combustion was determined as a function of gas density and flame propagation speed. Fiveland and Assanis [86] developed a coupled combustion boundary layer model of an HCCI engine. The model showed a computed boundary layer thickness of 0.2 mm near mid-compression and almost 3 mm at the end

of compression. Also, they found that 30-35% of the cylinder mass was contained in the boundary layer at the time of ignition.

In parallel efforts, recent advancements in numerical models of engine heat transfer were able to capture aspects of the dynamical changes of temperature in the near-wall region (NWR). Schmitt *et al.* [87] investigated the unsteady velocity and thermal boundary layers during the compression stroke under engine-relevant conditions using direct numerical simulations (DNS). Results showed decreasing velocity and thermal boundary layer thickness towards the end of compression as a result of the decreasing kinematic viscosity. They found the boundary layer structure to be similar at all engine walls during compression. Also, the averaged velocity and thermal boundary layer profiles were found to deviate strongly from the law-of-the-wall.
Ma *et al.* [88] identified the shortcomings of a commonly-used algebraic equilibrium wall-function model for IC engine simulations, and developed a non-equilibrium differential wall model that provided more accurate characterization of the near-wall region irrespective of the wall distance and the piston location. Significant adverse pressure gradients due to the large vertical motion inside the cylinder (induced by tumble, swirl, and turbulence) were observed and included in the non-equilibrium wall model.

Additionally, Ma *et al.* [89] utilized experimental data of simultaneous near-wall velocity and heat-flux measurements conducted in an optical engine to assess the performance of different models in predicting the thermo-viscous boundary layer in IC engines in comparison to their non-equilibrium model. Their model was able to capture the structure and dynamics of boh momentum and thermal boundary layers, and had improved performance over previously employed correlations functions and equilibrium models. However, the lack of near-wall temperature field measurements prevented performing direct comparisons with experiments. Therefore, a significant

necessity exists in obtaining quantitative temperature characterization of the thermal boundary layer in an operating internal combustion (IC) engine.

This calls for experimental investigation of the evolution of near-wall temperature distribution in order to provide answers about the structural information of the transient thermal boundary layer flows in IC engines. Lyford-Pike and Heywood [90] initiated the efforts to investigate the thermal boundary layer, and were among the first to apply Schlieren photography in a special flow-visualization engine. Their measurements showed that the boundary layer thickness decreases during intake and increases steadily during compression and expansion to about 2 mm. It stops growing and becomes unstable during the exhaust process, separating for the cylinder wall and becoming entrained onto the bulk-gas and leaving the cylinder. Also, the thickness of the thermal boundary layer was found to vary substantially at different locations throughout the chamber. However, Schlieren photography does not provide any quantitative temperature information.

Partially satisfying the need for temperature measurements in the boundary layer of an operating IC engine, Lucht and Maris [91] reported coherent anti-Stokes Raman scattering (CARS) measurements of burned gas temperatures near the wall. Their measurements showed a distinct thickening of the thermal boundary layer during the expansion stroke despite experimental uncertainties. They resolved the temperature profile at the engine head at a varying spatial resolution of 25-50 μm. Then, Lucht et el. [92] performed single-point CARS measurements for the geometry and probe position corresponding to previous velocity data reported by Foster and Witze [81]. They were able to study the effect of swirl motion on temperature profiles, and measure wall heat transfer at the CARS measurements location. Nevertheless, single-point CARS measurements were insufficient in investigating the instantaneous thermal boundary layer profiles.

Einecke *et al.* [93] provided a technique for measuring the temperature distribution and temperature development in the unburned gas region based on two-line planar laser-induced fluorescence (PLIF) imaging of 3-pentanone. The technique was applied to turbulent combustion with inhomogeneous fuel distribution under transient conditions in SI engine combustion. A measurement precision of 4% was achieved for single-shot temperature images.

Dec *et al.* [7] characterized the development of thermal stratification (TS) in an HCCI engine using planar-imaging thermometry too. Results showed distinct hotter and colder regions with a turbulent structure late in the compression stroke. Snyder *et al.* [94] used planar laser-induced fluorescence (PLIF) measurements to investigate thermal stratification in an HCCI engine under fired operating conditions, and found similar distribution and development under motored and fired operating conditions. Dronniou *et al.* [95] analyzed the temporal evolution of thermal stratification, and found the cold turbulent structures extending from in-cylinder surfaces to be the main source of thermal stratification.

Kaiser *et al.* [96] used LIF of toluene to image spatial temperature fluctuations in the compression stroke, and noticed greater inhomogeneities confined near the walls. Peterson *et al.* [97] demonstrated the capability of high-speed LIF thermometry combined with particle image velocimetry (PIV) to capture two-dimensional simultaneous temperature and velocity measurements in an engine.

These studies laid the ground for further experimental investigations into engine heat transfer to achieve the pursued detailed characterization of boundary layer flow properties and development in IC engines. They showed the need for high spatial- and temporal-resolution to capture the dynamics and structures of the thermal boundary layer. Cundy and Sick [98] performed a higher-resolution experiment to identify boundary layer temperature field structures in IC

engines. They developed two-detection channels via beam splitter optics, and employed a single intensified camera to capture one image per cycle. They reported qualitative results showing increasing spatial and temporal temperature variations near the wall, but encountered challenges of limited signal-to-noise ratio. The averaged experimental temperature profiles in their work show high, bulk-like temperatures up to less than 1 mm from the surface.

The capacity to understand and predict engine heat transfer can be extended by investigating the in-cylinder surface temperatures. Luo *et al.* [99] used a laser-induced phosphorescence technique for quantitative measurements of in-cylinder wall temperature to study its influence on unburned hydrocarbon emissions in an optical engine. They also developed a novel dual-wavelength infrared (IR) diagnostic for surface temperature measurements offering fast response time, which was evaluated by performing simultaneous measurements with a thermocouple and laser-induced phosphorescence in an optical engine [100].

Nothing can put all this tremendous amount of work into perspective other than a quote by Borman and Nishiwaki [12]: "The problem –engine heat transfer- is a modeler's nightmare and an experimenter's agony, but is far too important to ignore. And it has not been ignored". The research effort presented in the next chapters presents results from high-speed high-resolution LIF temperature measurements and simultaneous heat flux measurements in the NWR of an operating research engine that will supplement the previously-collected PIV data of near-wall in-cylinder flow fields by Greene [82], which were utilized by Ma *et al.* [89].

Chapter 3 Experimental Methodology

Laser-based diagnostics are an attractive means to probe engine flows. Chapter 3 provides an overview on laser-induced fluorescence (LIF) thermometry, and its implementation in a reciprocating optical IC engine along with the details on the utilized laser and imaging systems.

3.1 Laser-Induced Fluorescence (LIF) Thermometry

The complexity in the unsteady flow of IC engines impose challenges on obtaining quantitative measurements of high spatial and temporal resolution, especially near the walls. However, laser-based optical imaging techniques offer many capabilities for capturing various flow properties and studying near-wall in-cylinder processes, as discussed thoroughly in [101], and they have been proven to be reliable methods for non-intrusive measurements in combustion environments.

A number of laser-based techniques that are fundamentally different have been developed and applied for temperature measurements in gas-phase flows. These include Rayleigh scattering [102], diode-laser absorption [103] coherent anti-Stokes Raman scattering (CARS) [104], and laser-induced fluorescence (LIF) [93]. Rayleigh scattering requires stable and narrow-band laser sources, and scattered laser light of surfaces, droplets, or dust presents a problem. Absorption-based measurements provide line-of-sight information, while CARS is typically restricted to single-point measurements lacking instantaneous spatial gradient information. On the other hand, many studies [7, 94, 96, 97, 105] have demonstrated the sensitivity of LIF to measure spatial distribution of temperature in engine environments.

LIF is a very sensitive laser imaging technique for species concentration, density, and temperature measurements in fluid mechanical processes, sprays, and combustion systems. It is an extremely useful technique for quantitative or semi-quantitative analysis of transient flows,

providing spatially and temporally resolved information of a desired plane, which makes it suitable to capture the dynamics of the transient flows in IC engines [106].

3.1.1 Background

LIF can be characterized as a two-step process that starts with the absorption of a laser photon, and followed by the emission of a fluorescence photon from the excited state. A laser beam can be formed into a light sheet to intersect with the fluid area of interest. For absorption, the laser wavelength (λ_L) must match an allowed energy transition of the LIF-active molecule. Only a fraction (ϕ_{LIF}) of these excited molecules emits a fluorescence photon, while the rest relax without light emission. The resulting fluorescence light from the excited molecules in the laser sheet is imaged through a selective filter onto a time-gated digital camera. An optical filter can be used to pass the mostly red-shifted fluorescence light at the emission wavelength (λ_{LIF}) towards the imaging system. An image intensifier is usually used in pulsed UV fluorescence applications to amplify the LIF signal. Only a fraction (η_{det}) of all emitted LIF-photons is detected by the imaging system and then converted to camera signal (S_f) that can be described according to equation (3-1),

$$S_f = n\, E_L\, \sigma_{abs}\, \phi_{LIF}\, \eta_{det} \tag{3-1}$$

Where S_f is the fluorescence signal per pixel, n is the number density of LIF species in the probe volume, E_L is the laser energy per cm^2, σ_{abs} is the absorption cross section, ϕ_{LIF} is the fluorescence quantum yield, i.e. the fluorescence efficiency, and η_{det} is the detection efficiency [107].

3.1.2 Detection Strategies

LIF thermometry can be performed using two different detection strategies [108]. The one-color detection captures a fluorescence image that spectrally integrates the fluorescence signal (S) originating from a volume located at position x, y, which can be characterized by equation (3-2),

$$S(x,y,T) = \eta_{det}\, E_{laser}(x,y)\, n_{tracer}(x,y)\sigma_{abs}\big(T(x,y)\big)\, \phi_{LIF}(T(x,y)) \tag{3-2}$$

Where η_{det} is the detection efficiency, E_{laser} is the laser energy, n_{tracer} is the tracer number density, σ_{abs} is the absorption cross-section, and ϕ_{LIF} is the fluorescence quantum yield. To yield temperature information, the one-color fluorescence image must be corrected for laser energy, laser profile, absorption, tracer number density, as well as other detection nonuniformities [95]. On the other hand, the two-color detection separates the fluorescence spectrum into two spectral bands referred to as the "red" and "blue" channel [97, 109, 110]. Separate LIF images are acquired for each spectral band, and the spectral ratio (i.e., $S_{ratio} = \frac{S_{RED}(x,y,T)}{S_{BLUE}(x,y,T)}$) provides a temperature-dependent LIF image that is independent of laser absorption, laser influence, and local mixture fraction inhomogeneities, as described in equation (3-3),

$$\begin{aligned} S_{ratio} &= \frac{S_{RED}(x,y,T)}{S_{BLUE}(x,y,T)} \\ &= \frac{\eta_{RED}\, E_{laser}(x,y)\, n_{tracer}(x,y)\sigma_{abs}\big(T(x,y)\big)\, \phi_{RED}\big(T(x,y)\big)}{\eta_{BLUE}\, E_{laser}(x,y)\, n_{tracer}(x,y)\sigma_{abs}\big(T(x,y)\big)\, \phi_{BLUE}\big(T(x,y)\big)} \\ &= f\big(T(x,y)\big) \end{aligned} \tag{3-3}$$

The one-color detection offers a better temperature sensitivity and precision uncertainty compared with the two-color detection. However, it requires a spatially homogeneous mixtures since it cannot distinguish between local temperature inhomogeneities and local mixture fraction inhomogeneities. On the other hand, the spectral ratio signal in the two-color detection yields higher precision uncertainties due to lower signal-to-noise ratio and lower temperature sensitivity. Peterson *et al.* [108] addressed the lack of practical analysis and comparison of LIF thermometry detection techniques in complex environments such as IC engines. Relative temperature images from the two techniques were found to match during compression and early expansion. However, the two-color technique was limited in its ability to detect thermal gradients near the end of

compression due to high precision uncertainties at high temperatures, which makes the one-color detection technique suitable for the purposes of this study due to its relatively high sensitivity.

3.1.3 Tracer Photophysics

Adding fluorescence tracer is necessary to enable LIF thermometry when the fluid of interest does not contain well-characterized LIF-active species in terms of the underlying photophysical processes that depend on excitation wavelength, gas composition, pressure, and temperature. The ideal tracer for this study should yield LIF signals that are directly proportional to temperature, and the interpretation of the measured LIF signal intensities would require a detailed knowledge of the underlying photophysical processes under operating engine environment. The choice of the target molecule for LIF thermometry influences the accessible temperature range, versatility of the technique, experimental approach, and spectroscopic evaluation procedure. Temperature measurements in engine studies have mostly used ketones as tracers because of the similarities in their chemical and physical properties to common hydrocarbon fuels in terms of evaporation, convection, diffusion, reactivity, and droplet formation [107].

Faust *et al.* [111] conducted a comparison of selected organic tracers for quantitative scalar imaging in the gas phase via LIF. Results showed that the temperature dependence of the fluorescence quantum yield of common tracers are significantly different in air than in nitrogen. LIF measurements with nitrogen as a bath gas can provide valuable information on heat transfer and mixing. However, air must be used as bath gas when combustion is of importance in engine studies. The quantum yield of most common tracers in air is in general one to two orders of magnitude lower than in nitrogen, which makes the LIF signal is much weaker. Figure 3-1 displays the relative quantum yield as a function of temperature in both nitrogen and air.

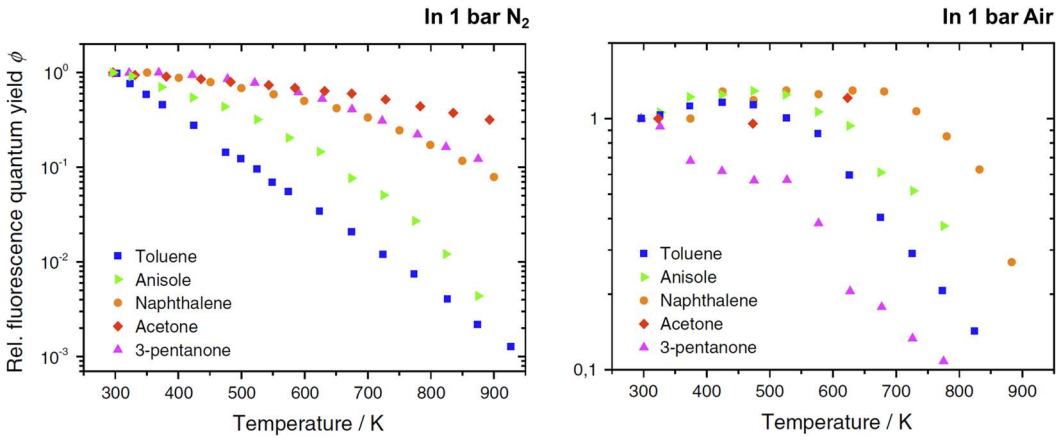

Figure 3-1. Temperature dependence of normalized fluorescence quantum yield of selected tracers excited at 266 nm [111].

The fluorescence quantum yield of toluene is strongly-dependent on temperature, and can be employed for precise temperature measurements for the purposes of this study. However, its temperature sensitivity is significantly reduced in air due to oxygen quenching that become the dominant de-excitation process. The total signal decreases only by one order of magnitude in air for the 300-900 K temperature range, while it is more than three orders of magnitude in nitrogen. Further details on the temperature- and pressure-dependence of toluene LIF can be found in [112].

3.2 Optical Reciprocating Engine

This experimental investigation is conducted in the single-cylinder Transparent Combustion Chamber III (TCC-III) engine, which is equipped with a full quartz cylinder for maximum optical access that allows for near-wall temperature measurements using LIF thermometry. It is a two-valve four-stroke spark-ignition (SI) engine featuring a pancake-shaped combustion chamber with a flat in-cylinder head and piston surface. Figure 3-2 provides a schematic of the TCC-III engine. The engine utilizes a Bowditch piston arrangement with a large piston-crown window (69.8 mm diameter). It has a geometric compression ratio (CR) of 10:1 with a clearance height of 9.5 mm at TDC.

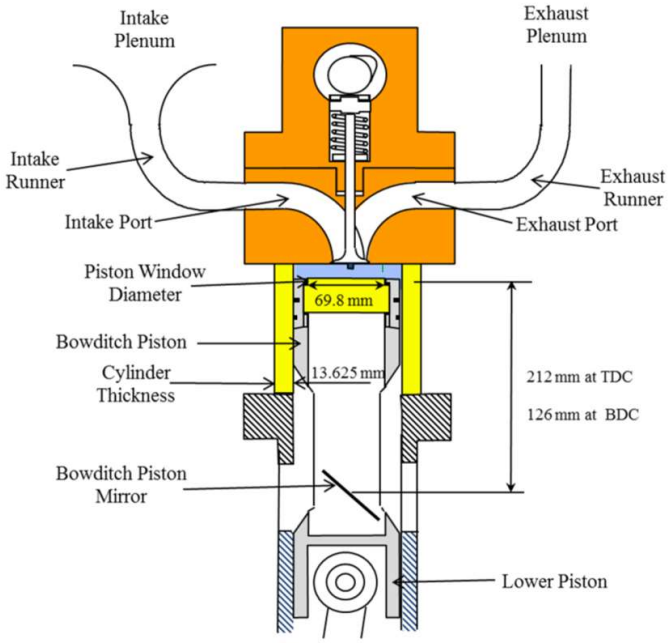

Figure 3-2. Schematic of the TCC-III engine and cylinder geometry. Quartz windows are shown in yellow.

For the current study, the laser sheet can be oriented vertically by being reflected off the Bowditch piston mirror to pass through the piston-crown window, and images of the NWR can be acquired through the cylinder liner. Relevant engine specifications are listed in Table 3-1, and additional detailed description of the engine geometry can be found in [113]. The crank-angle degree (CAD) definition assigns 0 CAD to top-dead center compression (TDCc).

Table 3-1. Specifications of the TCC-III engine.

Parameter	**Value**
Bore	92 mm
Stroke	86 mm
Connecting Rod Length	231 mm
Displacement	570 cm^3
Clearance Volume	64 cm^3
Compression Ratio (Geometric)	10:1
No. of Valves	2
Intake Valve Open (IVO)	352° CA
Intake Valve Close (IVC)	-120° CA
Exhaust Valve Open (EVO)	124° CA
Exhaust Valve Close (EVC)	348° CA
Steady-Flow Swirl Ratio	0.4

Cylinder pressure measurements are made with a transducer mounted in the cylinder head. The pressure transducer signals are digitized and recorded every 0.5 CAD for a defined set number of consecutive cycles. The intake and exhaust systems are also instrumented with pressure transducers to record the intra-cycle pressures every 0.5 CAD. Intake temperature are monitored using thermocouples mounted in the intake runner close to the cylinder head. For the current study, the intake plenum, intake runner, and exhaust runner were electrically heated to 368 K, while the cooling water was heated to 353 K to match the intake flow temperature. The engine was warmed up and transducer zero-drift adjusted to barometric standards prior to each test. At run time, the engine speed, delivered mass flow, and the average intake and exhaust pressures were controlled. In addition, a dual-thermocouple is mounted in the cylinder head, approximately 35.5 mm off center, to provide measurements of in-cylinder head surface temperatures.

And a stainless steel high-performance liquid chromatography (HPLC) pump is used to control the toluene flow. It provides a low-pulsation tracer flow to the intake pipe upstream of the intake plenum. The location upstream of the intake plenum is necessary to allow sufficient mixing time for a homogenous intake charge. The tracer seeding system is further described in [114]. Overall, engine operating conditions are very similar to those used in previous studies from this laboratory to allow for a comprehensive overall understanding of the undertaken measurements when possible.

3.3 Excitation System

The excitation system is based around a frequency-tripled, diode-pumped Nd:YAG laser (Quantronix Hawk-HP) with an optimized total power of 9 W for 266 nm at 6 kHz. A photodiode is set to capture variations in pulse-to-pulse laser energies. The output beam is sent to a prism to further reduce 532 nm light remaining from the frequency doubling process, and the 266 nm light

is then formed into a light sheet using a combination of cylindrical lenses that enters the engine via a UV mirror below the Bowditch piston. Figure 3-3 shows a schematic representation of the optical setup.

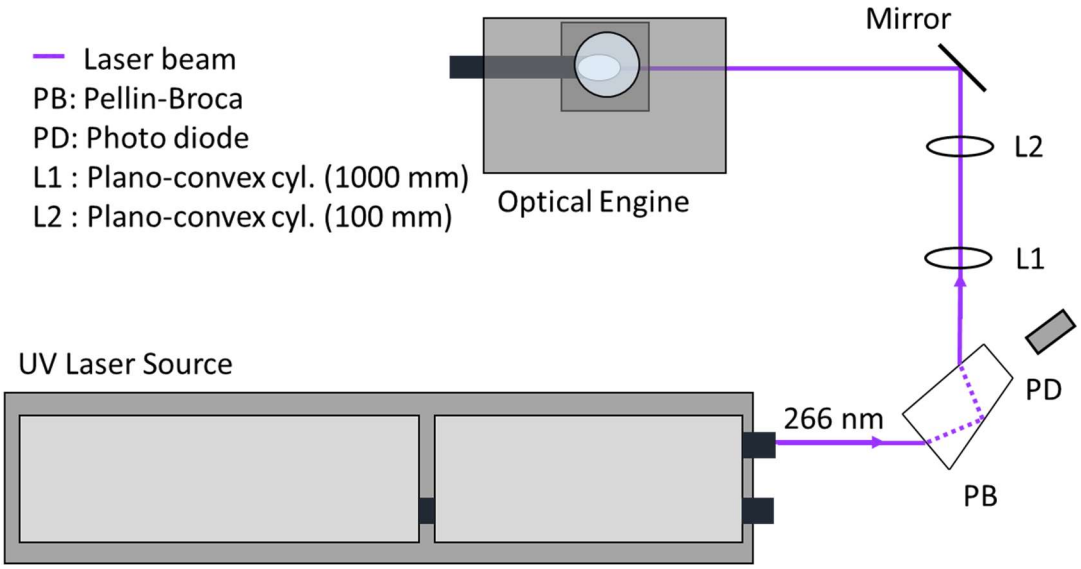

Figure 3-3. Top-view of the optical setup for LIF thermometry detection.

3.4 Imaging System

The imaging system is based around a high-speed CMOS camera (Phantom v7.3, Vision Research), which features a 14-bit image depth, 22 micro pixel, and 6,688 frames per second under full resolution. The CMOS sensor delivers a full-frame of 800 x 600 pixel^2 (4:3 aspect ratio). For this study, the camera was operated in a full resolution mode at a frame rate of 6 kHz with an exposure time of 160 µs. At this frequency and resolution, the camera can record over 20,000 images before having to stop recording to download the images. To enhance signal levels, a lens-coupled two-stage image intensifier is used (HS-IRO, LaVision) with a gain setting of 50 and a gate width of 1 µs. All triggering functions of the camera, laser and intensifier are based of the engine crankshaft encoder to ensure good synchronization with engine related events.

Chapter 4 Development of Thermal Stratification in the Near-Wall Region

This chapter investigates temperature fluctuations in the near-wall region (NWR) of an optical reciprocating engine under motored operating conditions at an engine speed of 500 RPM. It captures the development of natural thermal stratification near the in-cylinder head and piston surfaces, and presents statistical results on the evolution of temperature fluctuations in the NWR.

4.1 Experimental Methodology

Measurements of temperature distributions were conducted in the TCC-III engine, described in Chapter 3. The engine is equipped with a two-valve flat cylinder head, centrally mounted spark plug, quartz glass cylinder, and optical access is achieved through the quartz cylinder liner and the quartz flat piston window.

4.1.1 Operating Parameters

The engine was operated with dry, high-purity nitrogen used as the intake gas to avoid quenching of the fluorescence signal by oxygen. Toluene was premixed with the intake charge upstream of the intake plenum using a high-performance liquid chromatography (HPLC) pump. Operating parameters and relevant engine details are shown in Table 4-1.

Table 4-1. Engine parameters and operating conditions.

Parameter	Value
Engine speed	500 RPM
Intake pressure	40 kPa
Exhaust pressure	98 kPa
Engine oil and coolant temp.	353 K
Intake temperature	353 K
Intake valve closing (IVC)	-120 CAD
Exhaust valve opening (EVO)	124 CAD
Toluene tracer seeding	3% by vol.

4.1.2 Optical Setup

High-speed toluene PLIF thermometry was performed to capture temperature variations in a 20 × 12 mm^2 field-of-view adjacent to the cylinder head surface as shown in Figure 4-1. The Z-direction represents the wall-normal direction, i.e. distance from the in-cylinder head, with Z = 0 mm at the surface, and the X-direction represents the wall-parallel direction with X = 0 mm at the mid-point. The imaging plane is shifted about 28 mm from the spark plug. A diode-pumped Nd:YAG laser (Hawk-HP, Continuum) provided 266 nm pulsed light, and the laser beam was formed into a 1 mm thick light sheet at the measurement location by a combination of cylindrical lenses. It was reflected off a 45° mirror in the engine crankcase to pass through the quartz-bottom piston and illuminate a vertical viewing plane.

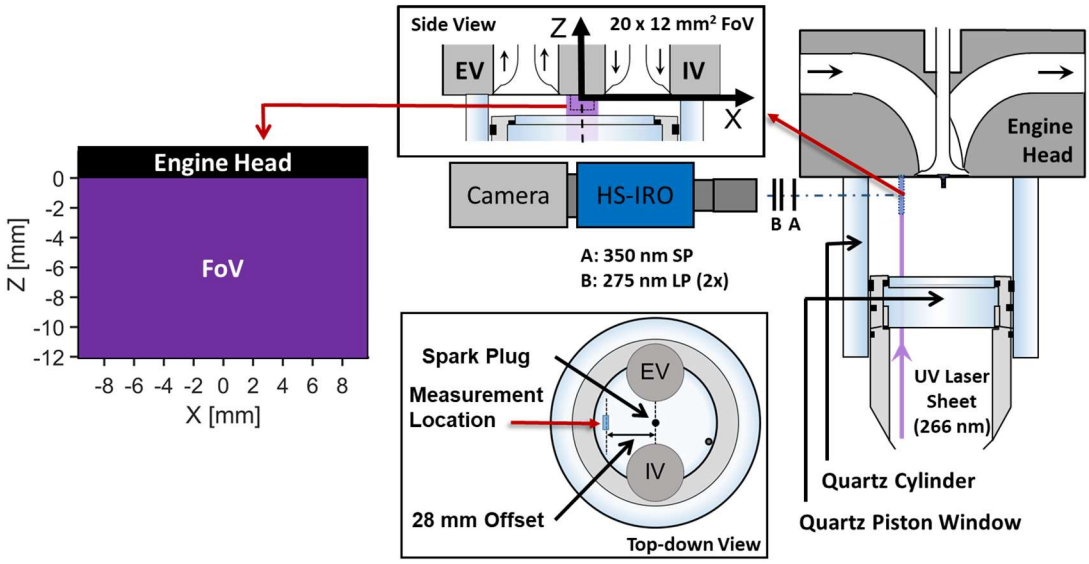

Figure 4-1. Imaging setup for one-color toluene LIF thermometry detection.

A one-color detection technique was used for the toluene-PLIF imaging using the excitation and imaging systems described in Chapter 3. Fluorescence signal was collected with a UV lens (Halle, f = 105 mm) attached to a two-stage intensified relay optics (HS-IRO, LaVision) coupled to a high-speed 14-bit CMOS camera (Phantom v7.3). The signal passed through two 275 nm long-pass (LP) filters and a 350 nm short-pass (SP) filter. An optical crank-angle encoder (AVL) was

used to synchronize the laser and camera at about 6 kHz, and timings of the laser pulse and camera acquisition were controlled by a high-speed controller (HSC, LaVision). LIF images at every 0.5 CAD were recorded for 14 consecutive cycles under motored conditions. The in-plane spatial resolution of the PLIF detection system was determined with a 1951 USAF resolution target, illuminated by visible light, to be approximately 0.25 mm.

4.1.3 Image Processing

LIF images from the one-color detection technique require substantial post-processing steps before deriving quantitative information [101]. These include corrections for variations in pulse-to-pulse laser energy, background fluorescence, tracer number density changes with crank angle, light attenuation and other image non-uniformities due to beam profile and steering [7, 96, 115, 116]. This work evaluates toluene LIF thermometry results derived from two image processing methods that are common in the literature. These methods are denoted as the "flat-field correction" (FFC) [13, 94, 96] and the "multi-step correction" (MSC) derived from [105]. Further details of each method are provided in Appendix 1.

4.1.3.1 Method 1: Flat-field correction (FFC)

Instantaneous LIF images were first normalized by reference laser energy readings and a reference toluene number density at intake valve closing (IVC). Then, a normalization by the multi-cycle mean PLIF image was carried out to correct for laser attenuation and other non-uniformities. A moving Gaussian filter to a window of 9×9 pixel^2 (0.2 x 0.2 mm^2) was applied lastly to the fluorescence images, before temperature calibration, for noise reduction. Figure 4-2 demonstrates the image processing procedure using the FFC method for an instantaneous LIF image at 0 CAD. The flat-field correction field is normalized by the spatial average intensity,

which allows for the absolute value of the LIF signal to be retained in the individual LIF images after the flat-field normalization.

The FFC method provides a clear representation of temperature variations relative to the multi-cycle mean, i.e. the ensemble average [13, 96], but it is not sufficient for any interest in the multi-cycle mean temperature field. It is recognized that the multi-cycle mean LIF image is non-uniform, and normalization may remove any temperature non-uniformities that are consistent from cycle-to-cycle (e.g., possible temperature boundary layer near solid surfaces). Hence, it is important to correct for the different non-uniformities separately using the MSC method in order to examine the multi-cycle mean temperature field, and reveal any possible temperature boundary layer near the solid surface.

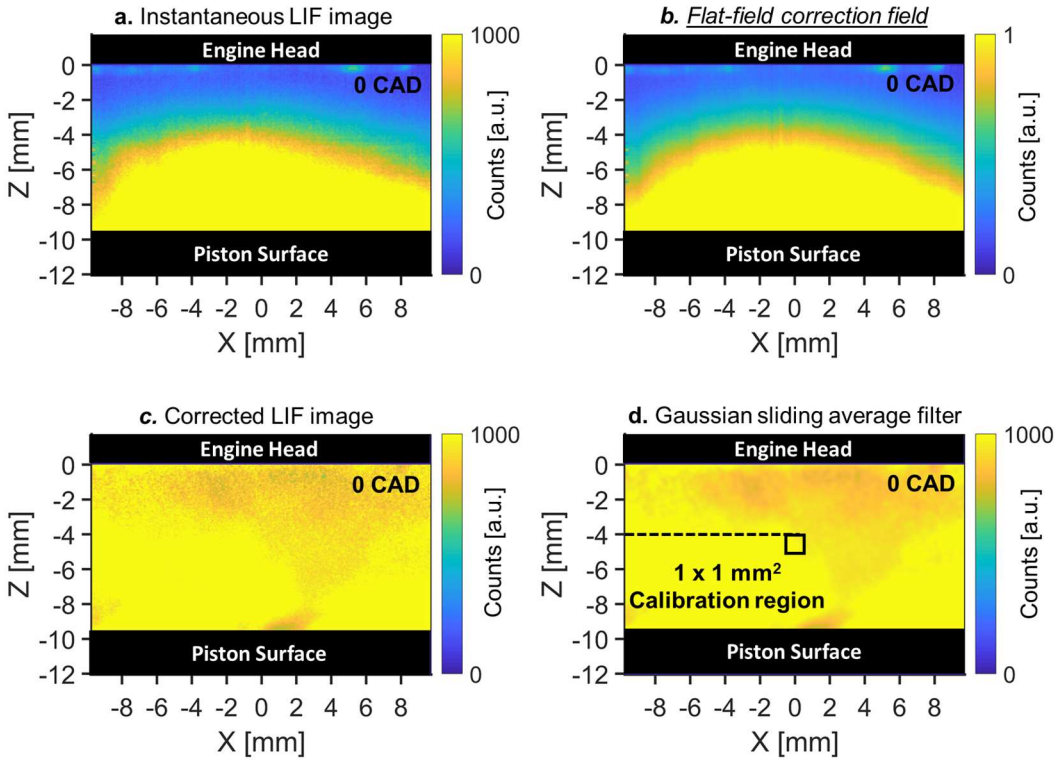

Figure 4-2. Image processing procedure for the FFC method shown for an instantaneous LIF image from cycle 7.

4.1.3.2 Method 2: Multi-step correction (MSC)

Figure 4-3 shows the post-processing steps applied to correct an instantaneous PLIF image at 0 CAD, and provides the correction fields extracted from the ensemble average image for reference. Instantaneous PLIF images were first normalized by reference laser energy readings before being normalized by a reference toluene number density at intake valve closing (Figure 4-3.a). Light attenuation was observed in the laser propagation direction. This was corrected for by evaluating the lambert-Beer law in the central vertical direction, i.e. the Z-direction, within the ensemble average PLIF images (Figure 4-3.b-c). Next, a correction field of the laser beam profile was extracted to correct for non-uniformities in the horizontal direction, i.e. the X-direction, (Figure 4-3.d-e). These steps were followed by correcting for apparent vertical strips from applying the aforementioned corrections (Figure 4-3.f-g). A moving Gaussian filter of a window size of 0.2 × 0.2 mm^2 was applied to the fluorescence images for noise reduction before calibrating to temperature (Figure 4-3.h).

The MSC method includes detailed evaluations to correct the different non-uniformities separately, but it allows to examine the multi-cycle mean temperature field and maintain any temperature non-uniformities that are consistent from cycle-to-cycle, unlike the FFC method, since it does not utilize a normalization by the multi-cycle mean.

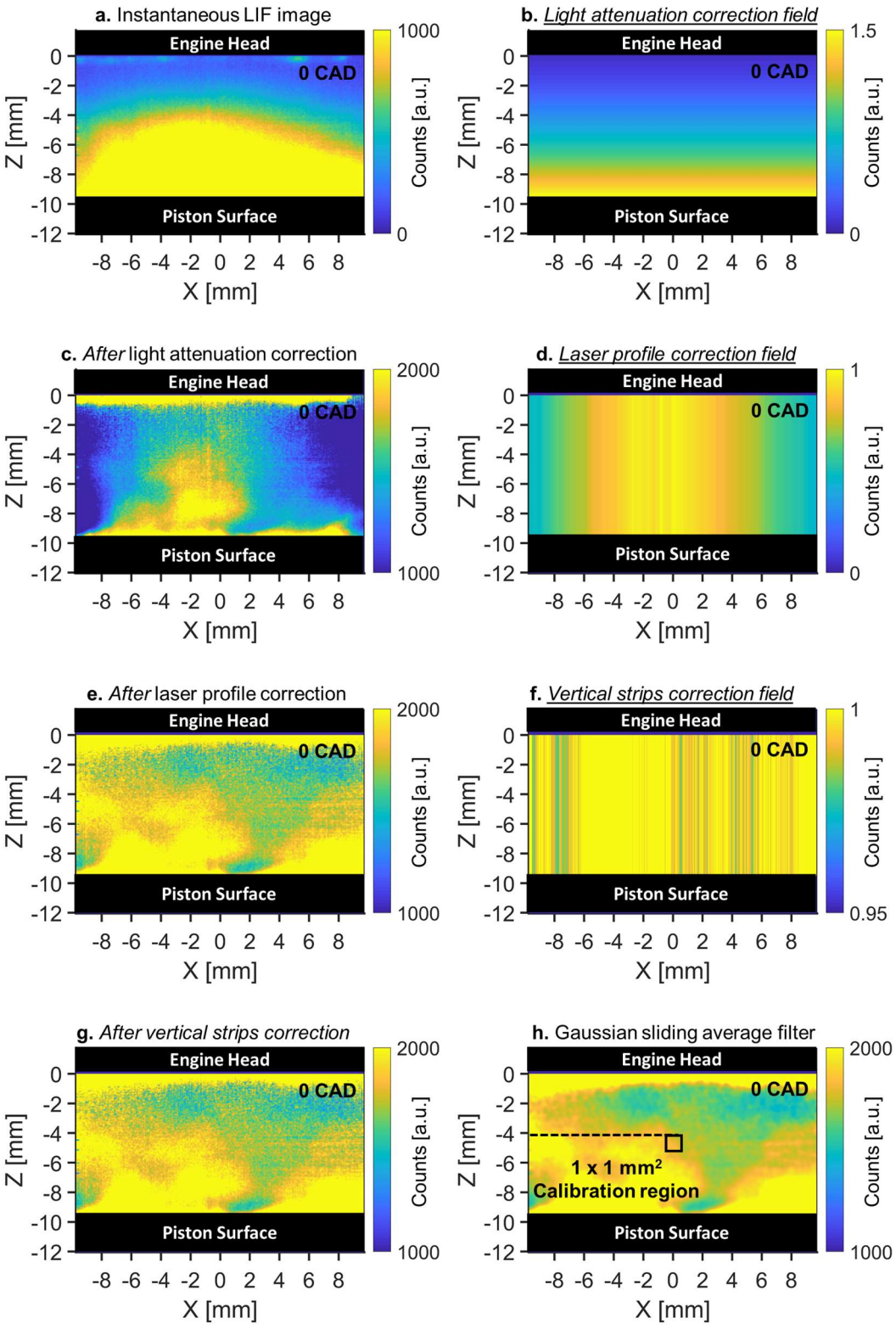

Figure 4-3. Image processing procedure for the MSC method shown for an instantaneous LIF image from cycle 7.

4.1.4 LIF Temperature Calibration

Once all the individual images have been corrected, a calibration is needed to convert PLIF intensity into temperature. For both processing method, the spatial average PLIF signal was extracted from a 1 × 1 mm^2 calibration region in the multi-cycle mean images at a distance of 4 mm from the surface, as shown in Figure 4-2.d and Figure 4-3.h. This distance was chosen to avoid the effects of the near-wall flow on the bulk gas temperature. LIF signals at each CAD from IVC to TDC were then calibrated to the predicted in-cylinder temperatures from a 1-D GT-Power simulation as shown in Figure 4-4.

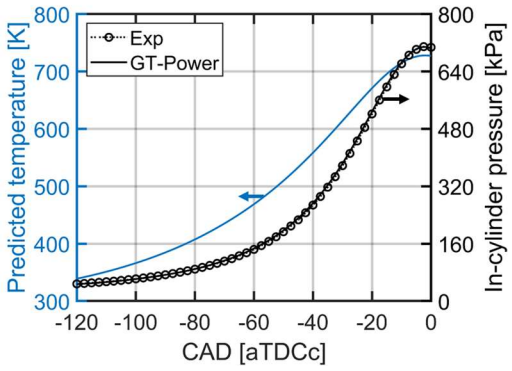

Figure 4-4. In-cylinder pressure measurements and predicted temperature and pressure from GT-Power.

The absolute accuracy of the LIF temperature measurements is primarily associated with the accuracy of the GT-Power simulation. The percent difference between simulated and experimental pressures was within 2%. This was achieved by tuning the heat transfer coefficients in the model to better represent the quartz components of the optical engine, and accounting for blow-by, i.e. cylinder leakage. Additionally, the one-color detection images will exhibit inaccuracies if the local LIF signal variations are caused by local mixture fraction in-homogeneities. The resulting LIF signal from the one-color detection cannot distinguish between temperature and concentration in-homogeneities.

The one-color image processing is very sensitive to local changes in laser profile and signal intensity. The respective calibration curve for each one-color image processing method are shown in Figure 4-5.

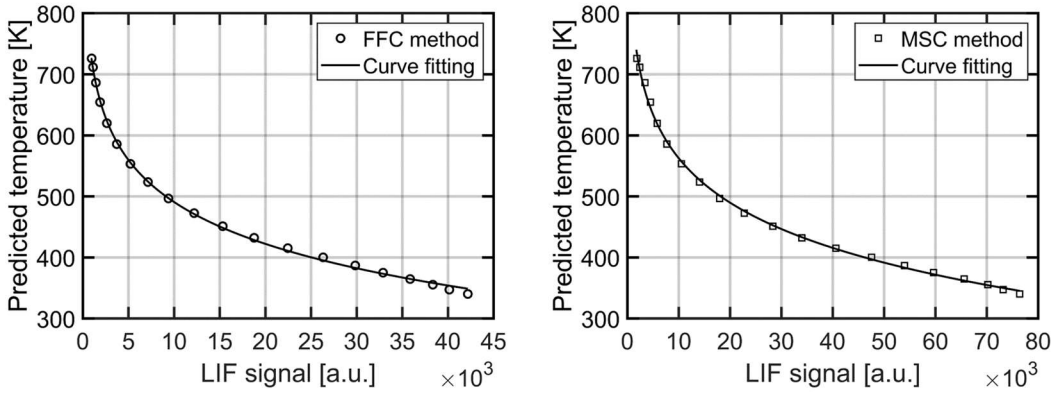

Figure 4-5. Calibration curves for FFC and MSC methods.

4.1.5 LIF Measurement Uncertainties

Random errors originating from intensifier shot noise and variations in laser intensity are the primary sources for precision uncertainty of the LIF thermometry technique [7, 96, 97, 115, 116]. The LIF uncertainty was defined as the ratio of standard deviation to the ensemble-average PLIF signal [116], and the corresponding temperature precision uncertainty was determined from the spatial standard deviation of temperature fluctuations. LIF precision uncertainty was found to be less than 10%, while the temperature precision uncertainty was determined to be within ±2 K. This was evaluated at each CAD from IVC to TDC within the 1 x 1 mm^2 calibration region, and larger precision uncertainty occurred towards TDC due to relatively lower SNR and sensitivities at higher temperatures [96, 97, 115, 116].

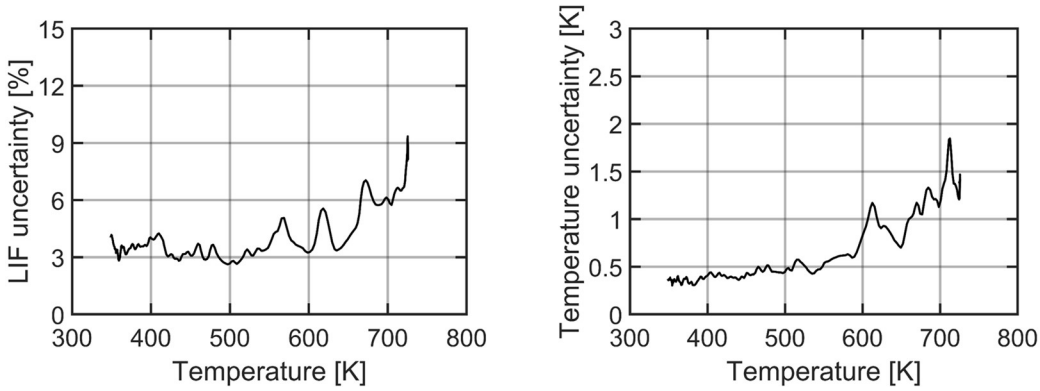

Figure 4-6. LIF precision uncertainty and respective temperature precision uncertainty.

4.2 Results and Discussion

Images from the FFC method are utilized in section 4.2.1 to investigate the development of natural thermal stratification during the compression and expansion strokes, while images from the MSC method are utilized in section 4.2.2 to examine relative temperature line profiles of the ensemble average images.

4.2.1 Development of Thermal Stratification

Once the LIF signal was calibrated to the predicted temperature, the 14-cycle ensemble-average temperature image was calculated for the FFC method. The ensemble-average temperature image was subtracted from the instantaneous temperature images to yield the temperature fluctuations distribution,

$$T'_{CAD,Cycle}(X,Z) = T_{CAD,Cycle}(X,Z) - < T >_{CAD}\ (X,Z) \tag{4-1}$$

Where $T'_{CAD,Cycle}(X,Z)$ is the temperature fluctuation about the ensemble-average, $T_{CAD,Cycle}(X,Z)$ is the instantaneous temperature, and $< T >_{CAD}\ (X,Z)$ is the ensemble-average temperature. Figure 4-7 illustrates the procedure to obtain the fluctuating T-map from the instantaneous T-Map at 0 CAD using the FFC method.

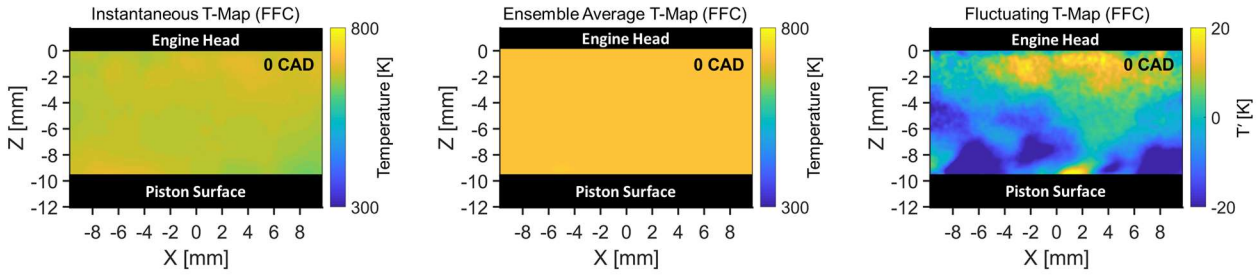

Figure 4-7. Procedure to obtain instantaneous fluctuating temperature distribution from the FFC method.

The development of thermal stratification is inspected here to investigate the formation and transport of temperature fluctuations in the NWR. Figure 4-8 and Figure 4-9 present a temporal sequence of instantaneous temperature fluctuations during the compression and expansion strokes, respectively. Images are presented for an individual cycle, which exhibits similar trends as observed visually in all 14 motored cycles.

The distribution of temperature fluctuations is homogeneous during early compression until -60 CAD, where thermal stratification starts to take place. Temperature fluctuations become first apparent near the in-cylinder head surface around -40 CAD. They persist and grow during compression, but remain mainly confined near the walls. Between -25 and 0 CAD, the temperature difference between the hot and cold regions increases, indicating a significant increase of the thermal stratification which reaches the bulk-region. Fluctuations become more predominant along the piston surface towards 0 CAD later in the compression stroke, where they appear to be transported along the piston surface by the flow in the positive x-direction.

The distribution of temperature fluctuations during expansion provides further insights on the late development of thermal stratification. Structures of temperature fluctuations appear larger in their spatial scale, and the sequence of instantaneous images captures the separation of temperature fluctuation structures from the in-cylinder head surface to the bulk-gas region. Thermal stratification decreases during late expansion, but remains noticeably higher than early

compression. It is important to mention here that the piston ring-pack is located about 4 mm from the piston top leading to a small top-land crevice volume, which could point to lesser effects of outgassing from the crevices during expansion than different engine geometries with larger crevice volume, as in [116]. The next subsections present further analysis of the temperature fluctuations extracted from all 14 cycles in a statistical manner in order to confirm trends for all cycles.

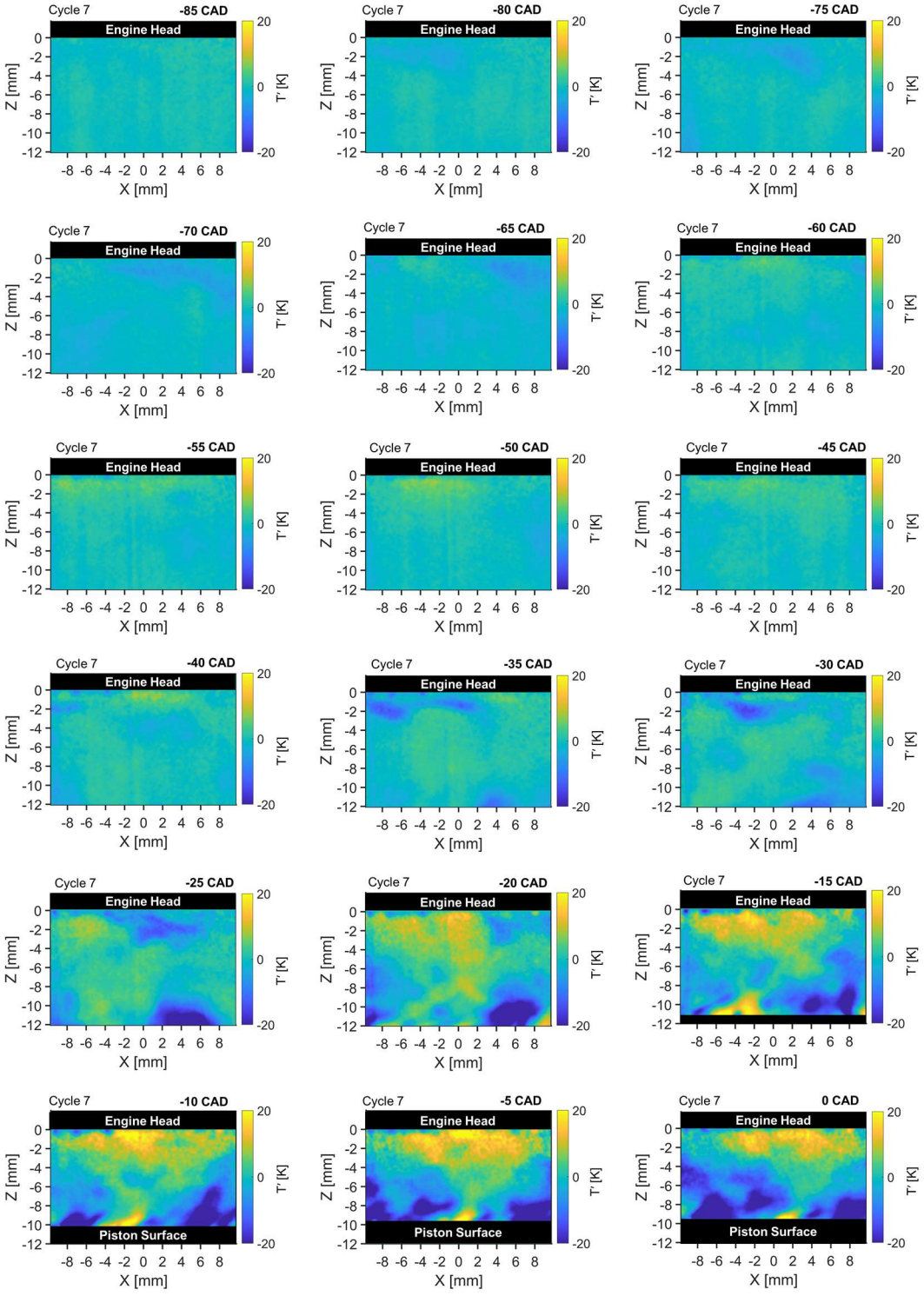

Figure 4-8. Temporal sequence of instantaneous temperature fluctuations during compression.

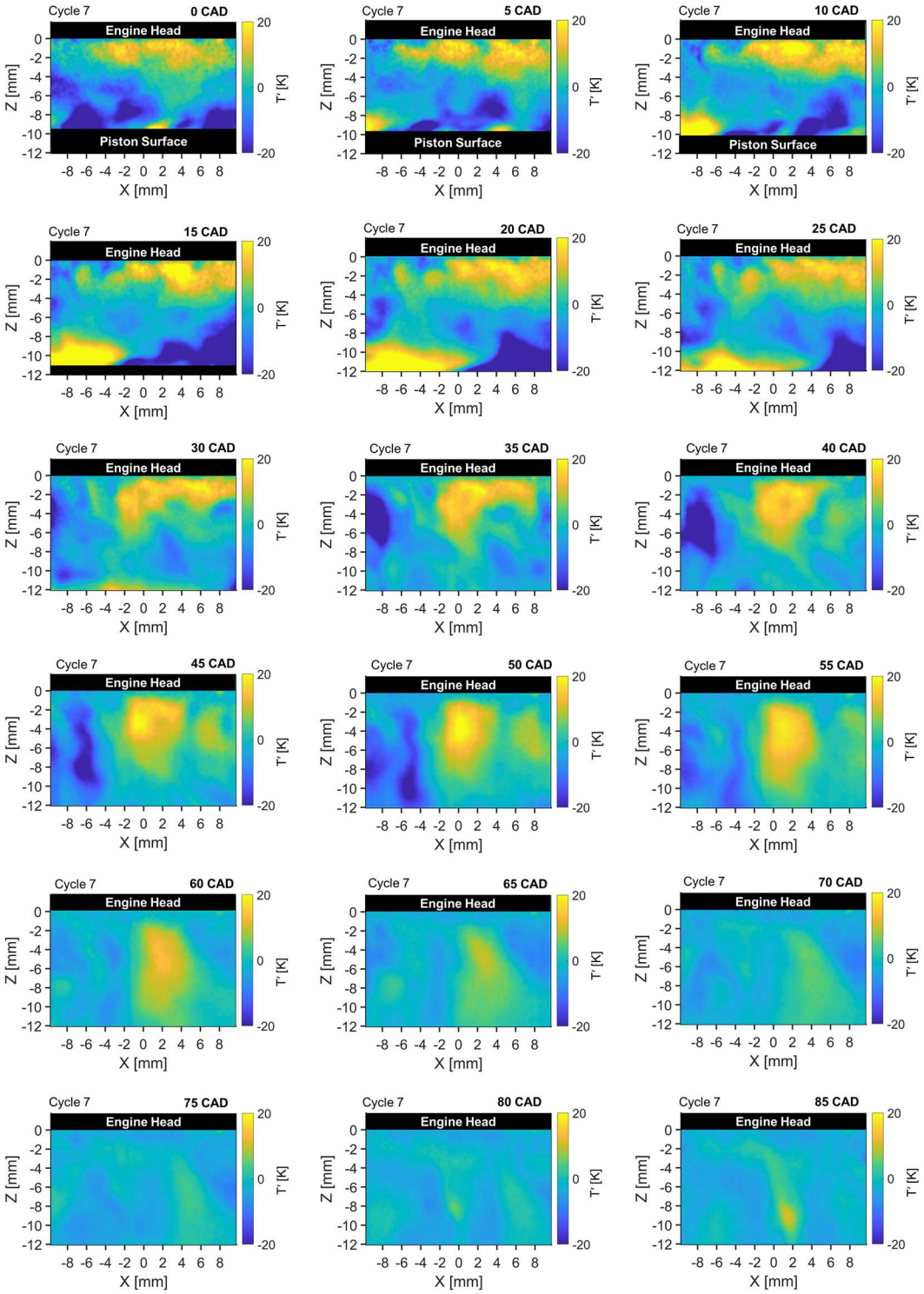

Figure 4-9. Temporal sequence of instantaneous temperature fluctuations during expansion.

4.2.1.1 Probability density functions (PDFs) of temperature fluctuations

Probability density functions (PDFs) provide a mean to quantify the thermal stratification observed in the NWR. The distribution of temperature fluctuations during compression and expansion is shown in the PDFs displayed in Figure 4-10. These PDFs represent the ensemble average curve by averaging several PDF curves that were extracted from instantaneous T-maps at a specific CAD from all 14 cycles.

The PDFs monotonically broaden with increasing compression before they start to narrow during expansion, but to a lesser extent compared to early compression. The higher peaks during early compression are due to the low temperature fluctuations in the NWR. The peak of the curve drops to reach its lowest at TDC due to significant thermal stratification that results from the increasing temperature difference between the wall and the bulk-gas region. The peak rise again during expansion as the curves narrow indicating decreasing thermal stratification within the imaging field.

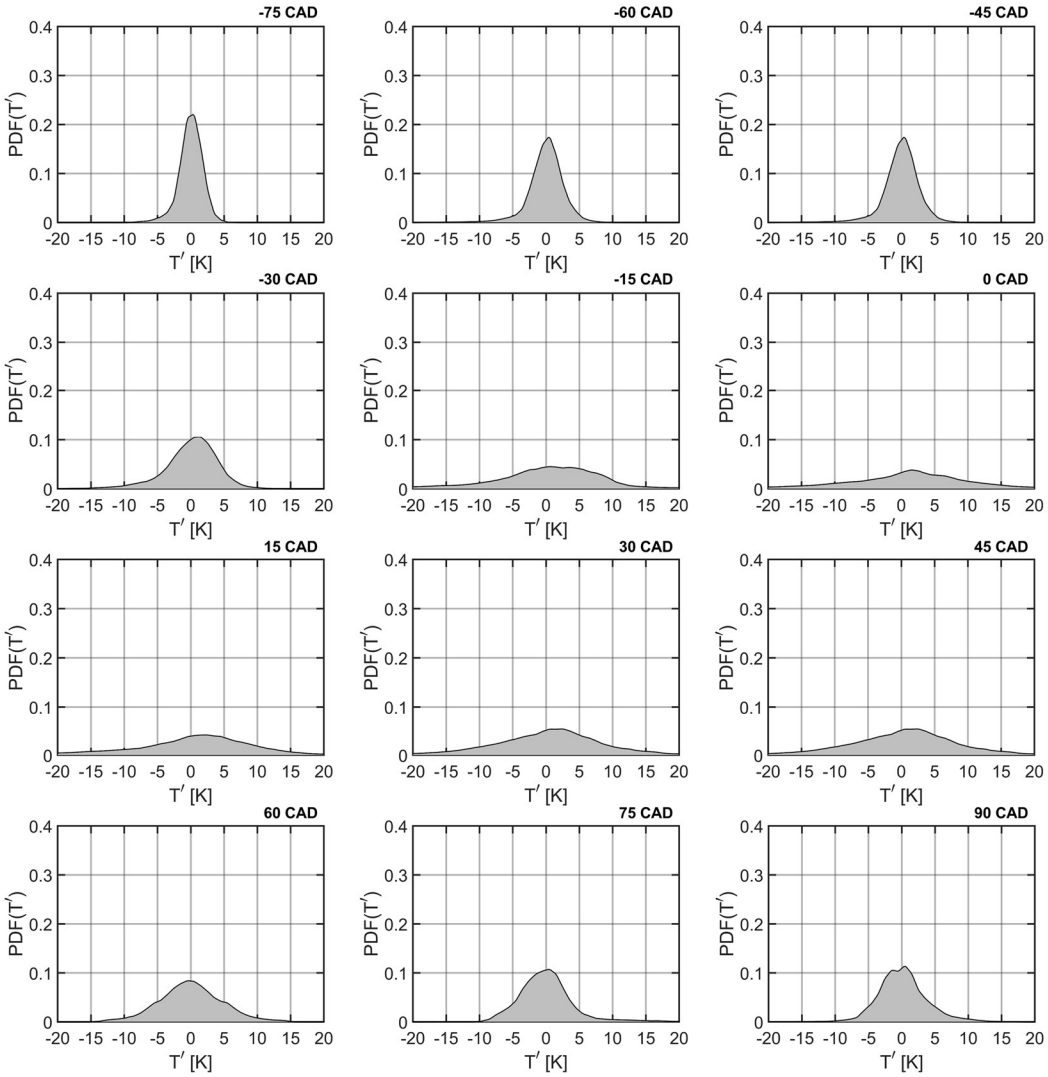

Figure 4-10. Averaged area PDFs of instantaneous fluctuating temperature.

4.2.1.2 Magnitude of the thermal stratification

Figure 4-11 presents the spatial standard deviation of temperature fluctuations ($\sigma_{T'}$), which is a useful measure to quantify the magnitude of the fluctuating thermal stratification [95]. A significant increase in the magnitude of the thermal stratification can be seen around -40 CAD, and it reaches its peak at TDC at a value above 10 K before dropping gradually during expansion due to probably the change in the convective transport with the reversal of the piston motion [13].

Expansion cools down the charge, and the downward motion of the piston could enhance mixing that homogenizes the existing thermal stratification at the end of compression.

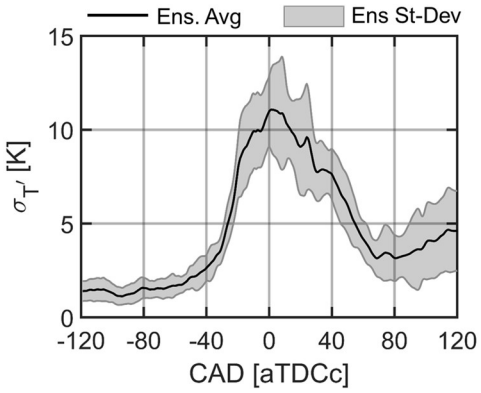

Figure 4-11. Evolution of the magnitude of the thermal stratification.

4.2.1.3 Thermal stratification at TDC

The development of thermal stratification becomes strong at TDC. This can be explained by the decrease of the piston motion that pushes cold gases toward the in-cylinder head surface, the higher temperature difference between the bulk-gas and the walls, and the potential increase of the in-cylinder turbulence. Figure 4-12 presents instantaneous temperature fluctuations from all 14 consecutive cycles at TDC. The visual inspection of these fluctuations from multiple cycles allows to evaluate the difference in their distribution from cycle-to-cycle. These images also confirm that the thermal stratification at TDC can be characterized mainly by the existence of high temperature fluctuations that are mainly confined at the in-cylinder head and the piston-top surfaces. The structures appear random in their location and dimension, but overall larger at the piston-top surface than the in-cylinder head. The randomness and differences between these consecutive cycles can be attributed to the turbulent nature of the flow and the cycle-to-cycle variations in heat transfer.

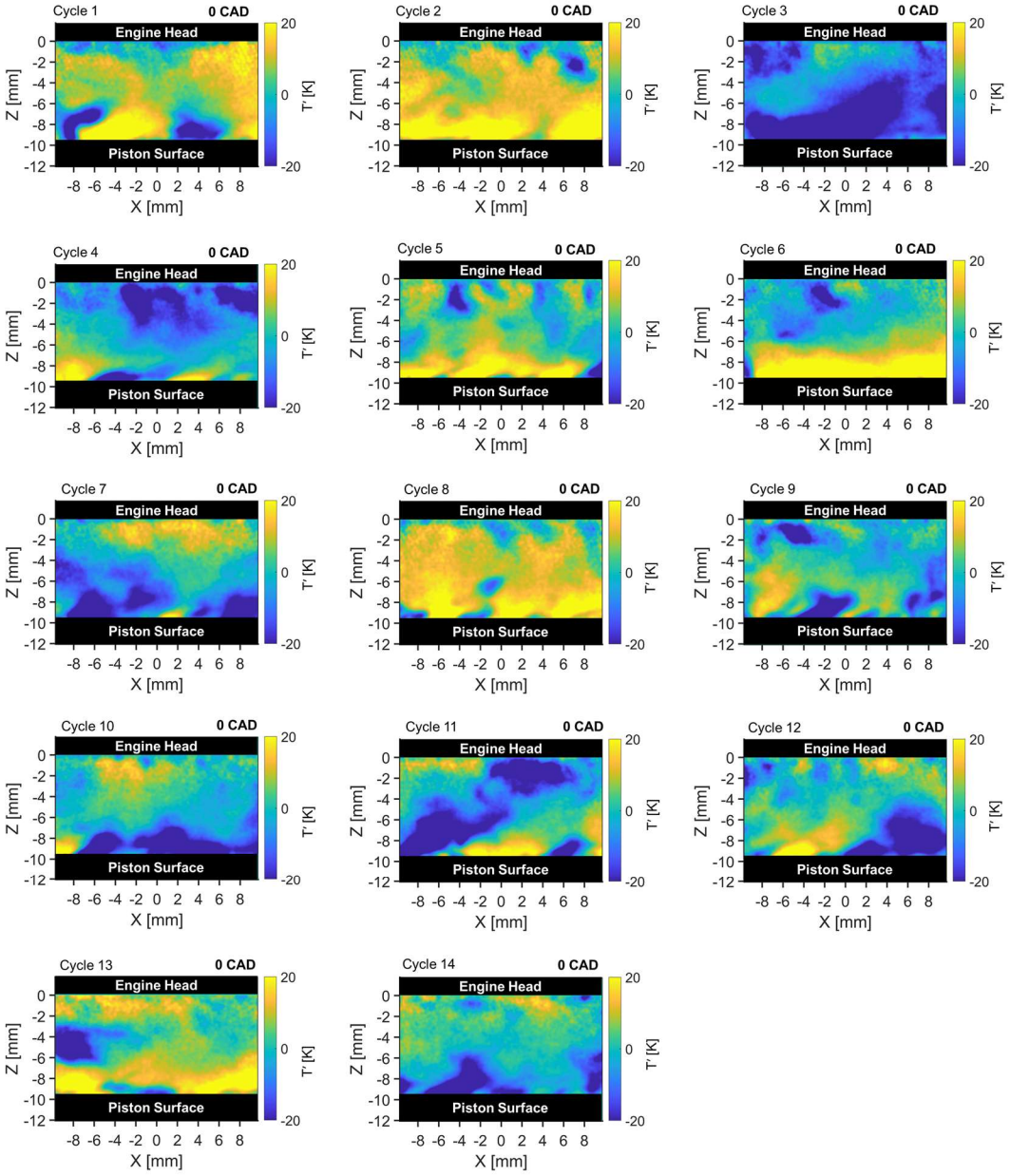

Figure 4-12. Instantaneous temperature fluctuations at 0 CAD.

As mentioned above, the near-wall temperature fluctuations above the piston top surface are larger in value and size than the fluctuations at the in-cylinder head surface. At the engine head, temperature fluctuations can be described by small structures confined within a thin region. At the piston-top surface, fluctuations can be characterized by the interaction of hotter and colder regions

of relatively larger sizes. This can be possibly explained by differences in the near-wall flow responsible for convection.

The use of standard deviation distribution of temperature fluctuations is intended to provide an indication of the repeatability of patterns observed with the previous single-cycle T-maps. The St-Dev image shown in Figure 4-13 were created by computing the temperature standard deviation of each pixel over the set of 14 images. Higher standard deviation values are located at the piston-top surface, which indicates larger cycle-to-cycle temperature fluctuations than the engine head.

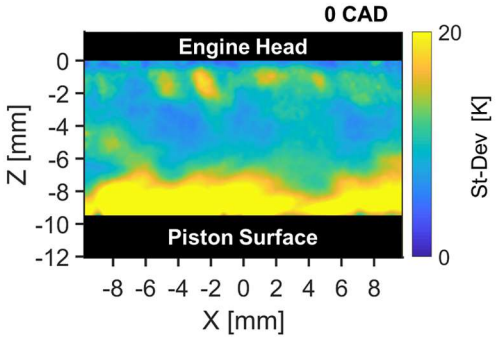

Figure 4-13. St-Dev T-maps at 0 CAD.

4.2.2 Relative Temperature Line Profile

The MSC method allows to inspect the development of the cold boundary layers near the walls by examining the relative ensemble average T-maps. Once the LIF signal was calibrated to the predicted in-cylinder temperature, the 14-cycle ensemble-average temperature image was calculated for the MSC method. The spatial average temperature ($\bar{T}$) was subtracted from the ensemble average temperature image to yield the relative ensemble average temperature image,

$$\Delta T_{CAD}(X,Z) = < T >_{CAD} (X,Z) - \overline{< T >_{CAD}} \quad (4\text{-}2)$$

Where $\Delta T_{CAD}(X,Z)$ is the relative temperature, $< T >_{CAD} (X,Z)$ is the ensemble-average temperature, and $\overline{< T >_{CAD}}$ is the spatial average temperature of the ensemble-average temperature distribution within

the field-of-view. Figure 4-14 illustrates the procedure to obtain the relative ensemble average T-map from the instantaneous T-Map at 0 CAD using the MSC method.

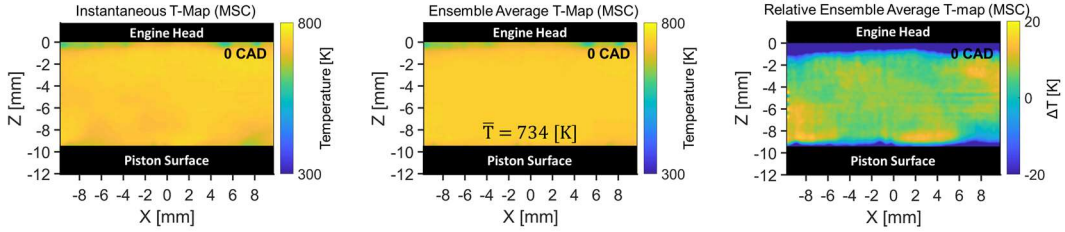

Figure 4-14. Processing procedure for getting the relative ensemble average temperature distribution.

This procedure was applied to other selected CADs around TDC to better understand the development of cold boundary layers near the walls. Figure 4-15 shows images of relative ensemble average temperature distribution from the MSC method.

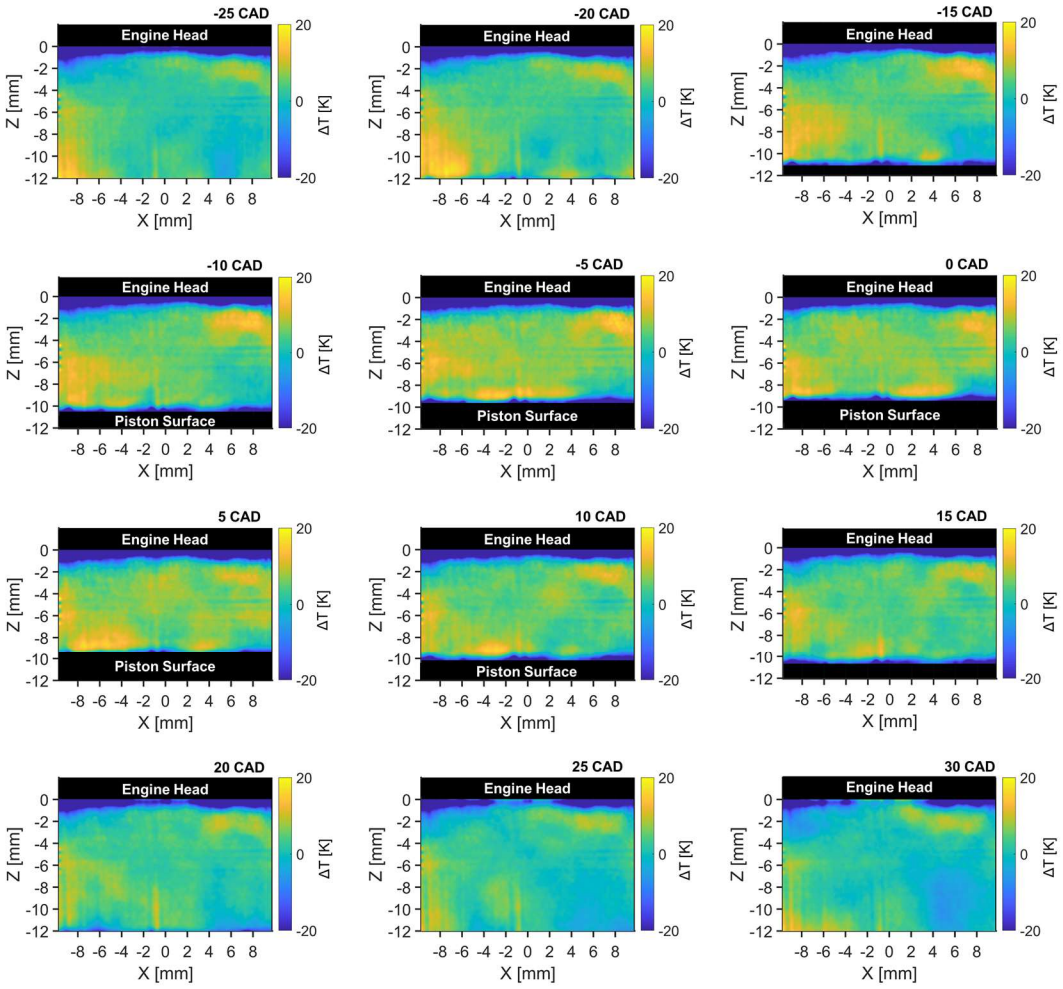

Figure 4-15. Temporal sequence of relative ensemble-average temperature distributions during late compression and early expansion.

Figure 4-16 shows plots of relative temperature profiles in the wall-normal direction, i.e. the Z-direction, derived from the images presented in Figure 4-15. Solid lines and shade represent the average and the standard deviation over the wall-parallel direction, i.e. the X-direction. All temperature profiles presented in Figure 4-16 are based on the temperature difference relative to the spatial average temperature ($\bar{T}$) of the 20 x 12 mm^2 imaging field. The little kink at Z < 0.25 mm is most likely an artifact of the pixel resolution. The line profiles show colder regions at the in-cylinder head and piston-top surfaces. The temperature difference near the in-cylinder head and the piston-top surfaces increases as the piston moves toward TDC. The difference is larger near

the in-cylinder head indicating higher wall heat transfer at the head surface than the piston-top. A temperature reversal is observed in the line profiles near the piston-top surface as the piston moves upward during compression. This reversal disappears as the piston moves downward during expansion.

These observations can also be due to the fact that the top boundary corresponds to the head's solid steel, while the bottom boundary corresponds to the piston's top quartz surface. Additionally, the temperature of the cylinder head is controlled by the coolant temperature, while the piston-bottom surface is cooled down by air jets.

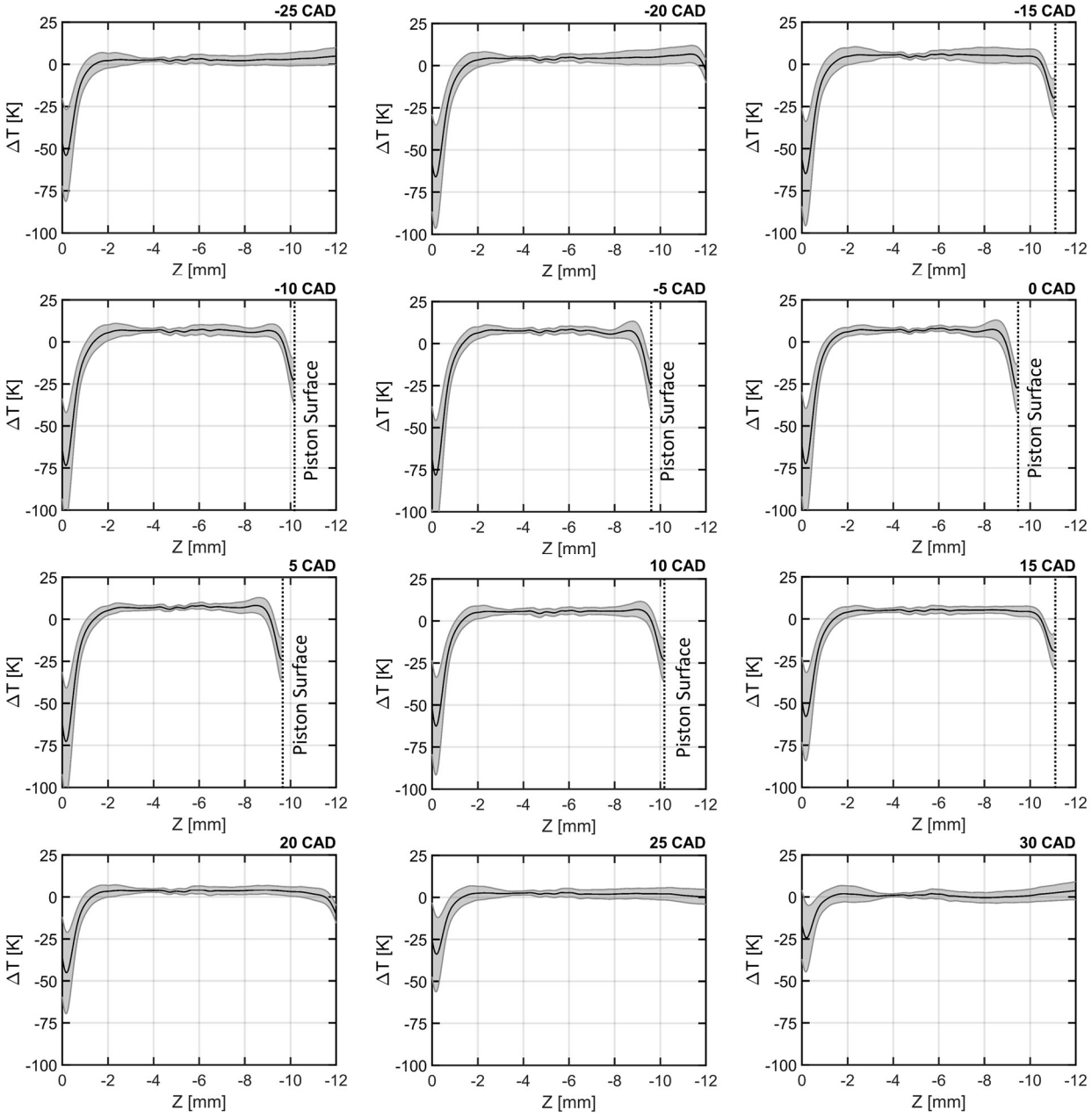

Figure 4-16. Relative temperature line profiles of ensemble temperature distributions versus the distance from the in-cylinder head surface. Dashed line indicates the piston surface.

4.3 Summary

The development of thermal stratification in the near-wall region (NWR) of the TCC-III engine was investigated under motored conditions within a 20 x 12 mm field-of-view adjacent to

the in-cylinder head surface. Visual inspection of instantaneous temperature fluctuations shows increasing thermal stratification towards TDC that drops gradually during expansion. A PDF analysis of the images provided a more quantitative evaluation of the observed trends, which were further analyzed by examining the magnitude of the fluctuating thermal stratification.

Results have shown that the thermal stratification in the NWR was primarily originating from the in-cylinder head and piston-top surfaces. It is important to note here that colder and hotter regions in the instantaneous temperature fluctuations simply represent lower and higher temperature fluctuations than the ensemble-average, respectively [117]. The development and transport of temperature fluctuations were affected by turbulence, and it requires a more in-depth analysis of the evolution of their size, possibly under varied engine conditions, in order to characterize their formation. The development of the outer boundary layer was investigated by examining the relative temperature line profiles in the wall-normal direction. These indicate increasing temperature gradients at the surfaces towards TDC that is higher at the in-cylinder head surface than the piston-top. In summary, these results demonstrate the impact of wall heat transfer and convection by turbulent in-cylinder flows on causing the development of thermal stratification in the NWR.

Chapter 5 Near-Wall Temperature Variations under Varied Engine Conditions

This chapter investigates temperature variations near the in-cylinder head surface of an optical reciprocating engine under motored and fired operating conditions at two different engine speeds of 500 and 1300 RPM. It examines the development of fluctuating thermal stratification in the near-wall region (NWR) at a measurement location corresponding to previous near-wall velocity measurements by Greene [27], and inspects the impact of the wall distance on temperature variations under varied operating conditions as the previous work on momentum characterization.

5.1 Experimental Methodology

High-speed toluene PLIF thermometry was conducted in the near proximity of the in-cylinder head surface of the TCC-III engine, described in Chapter 3.

5.1.1 Operating Parameters

Relevant engine details and the operating parameters are given in Table 5-1. The engine operated under motored and fired conditions at 500 and 1300 RPM with air used as intake gas.

Table 5-1. Engine parameters and operating conditions.

Parameter	Value
Engine speed	500 RPM, 1300 RPM
Engine bore, stroke	92, 86 mm
Intake, exhaust pressure	40, 98 kPa
Engine oil and coolant temp.	353 K
Intake temperature	353 K
Intake valve closing (IVC)	-120 CAD
Ignition timing	-18 CAD
Toluene tracer seeding	5% by vol.
Fuel, stoichiometric ratio	Propane, 1

5.1.2 Optical Setup

Measurements of temperature distributions were conducted to capture temperature variations in an 8 × 6 mm^2 field-of-view adjacent to the cylinder head surface as shown in Figure 5-1. The diagnostic is implemented using a Scheimpflug adapter that allowed using a tilted imaging setup that better enable imaging in the near-wall proximity as discussed in [89, 118, 119]. Toluene was premixed with air upstream of the intake plenum using a high-performance liquid chromatography (HPLC) pump. A diode-pumped Nd:YAG laser (Hawk-HP, Continuum) provided 266 nm pulsed light, and a laser beam was formed into a 1 mm thick light sheet at the measurement location by a combination of spherical and cylindrical lenses. It was reflected off a 45° mirror in the engine crankcase to pass through the quartz-bottom piston and illuminate a vertical viewing plane.

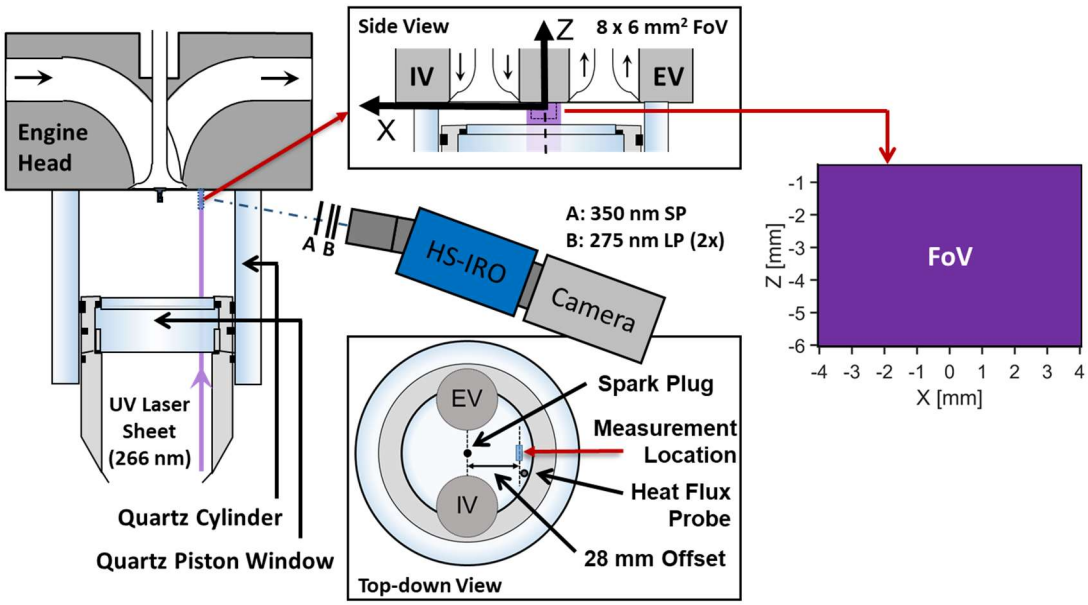

Figure 5-1. Imaging setup for one-color toluene LIF thermometry detection.

A one-color detection technique was used for the toluene-PLIF imaging with a setup similar to [7, 96, 120]. Fluorescence signal was collected with a UV lens (Halle, f = 105 mm) attached to

a two-stage intensified relay optics (HS-IRO, LaVision) coupled to a high-speed 14-bit CMOS camera (Phantom v7.3). The signal passed through two 275 nm long-pass (LP) filters and a 350 nm short-pass (SP) filter. An optical crank-angle encoder (AVL) was used to synchronize the laser and camera at about 6 kHz, and timings of the laser pulse and camera acquisition were controlled by a high-speed controller (HSC, LaVision). PLIF images at every 1.3 CAD were recorded for 73 and 145 consecutive cycles under motored and fired conditions at 1300 RPM, respectively. And images at every 0.5 CAD were recorded for 28 and 56 consecutive cycles under motored and fired conditions at 500 RPM, respectively. The in-plane spatial resolution of the PLIF detection system was determined with a 1951 USAF resolution target to be approximately 0.1 mm.

5.1.3 Image Processing

LIF images from the one-color detection technique require substantial post-processing steps before deriving quantitative information [101]. These include corrections for variations in pulse-to-pulse laser energy, background fluorescence, tracer number density changes with crank angle, light attenuation and other image non-uniformities due to beam profile and steering [7, 96, 115, 116]. Similar to image processing described in section 4.1.3, this work evaluates toluene LIF thermometry results derived from two image processing methods that are common in the literature. These methods are denoted as the “flat-field correction” (FFC) [13, 94, 96] and the “multi-step correction” (MSC) derived from [105].

The use of a tilted imaging setup utilizing a Schempflug adapter and imaging within a smaller field-of-view in the close proximity of the cylinder head, for the work presented in this chapter, introduced two issues that required changes to the image processing applied in Chapter 4. One is capturing reflections of the 266 nm laser sheet -despite the optical filters put in front of the

camera lens-, which is addressed in both correction methods by a background subtraction step. The other is capturing background fluorescence signal, indicated by the increase in LIF signal in the direction of the laser propagation, which prevented applying a correction for light attenuation and required a different assessment for the background fluorescence effects in the MSC method.

5.1.3.1 Method 1: Flat-field correction (FFC)

Instantaneous LIF images were first normalized by reference laser energy readings before subtracting the background and being normalized by a reference toluene number density at intake valve closing (IVC). Then, a normalization by the multi-cycle mean PLIF image was done to correct for laser attenuation and other non-uniformities. A moving Gaussian filter to a window of 92×92 pixel^2 (1×1 mm^2) was applied lastly to the fluorescence images before temperature calibration for noise reduction. Figure 5-2 demonstrates the image processing procedure for an instantaneous LIF image captured at 0.1 CAD under motored conditions at 1300 RPM. The flat-field correction field is normalized by maximum intensity, which allows for the absolute value of the LIF signal to be retained in the individual LIF images after the flat-field normalization. As mentioned in Chapter 4, this method provides a clear representation of temperature variations relative to the mean [13, 96], but is not sufficient for any interest in the mean temperature field.

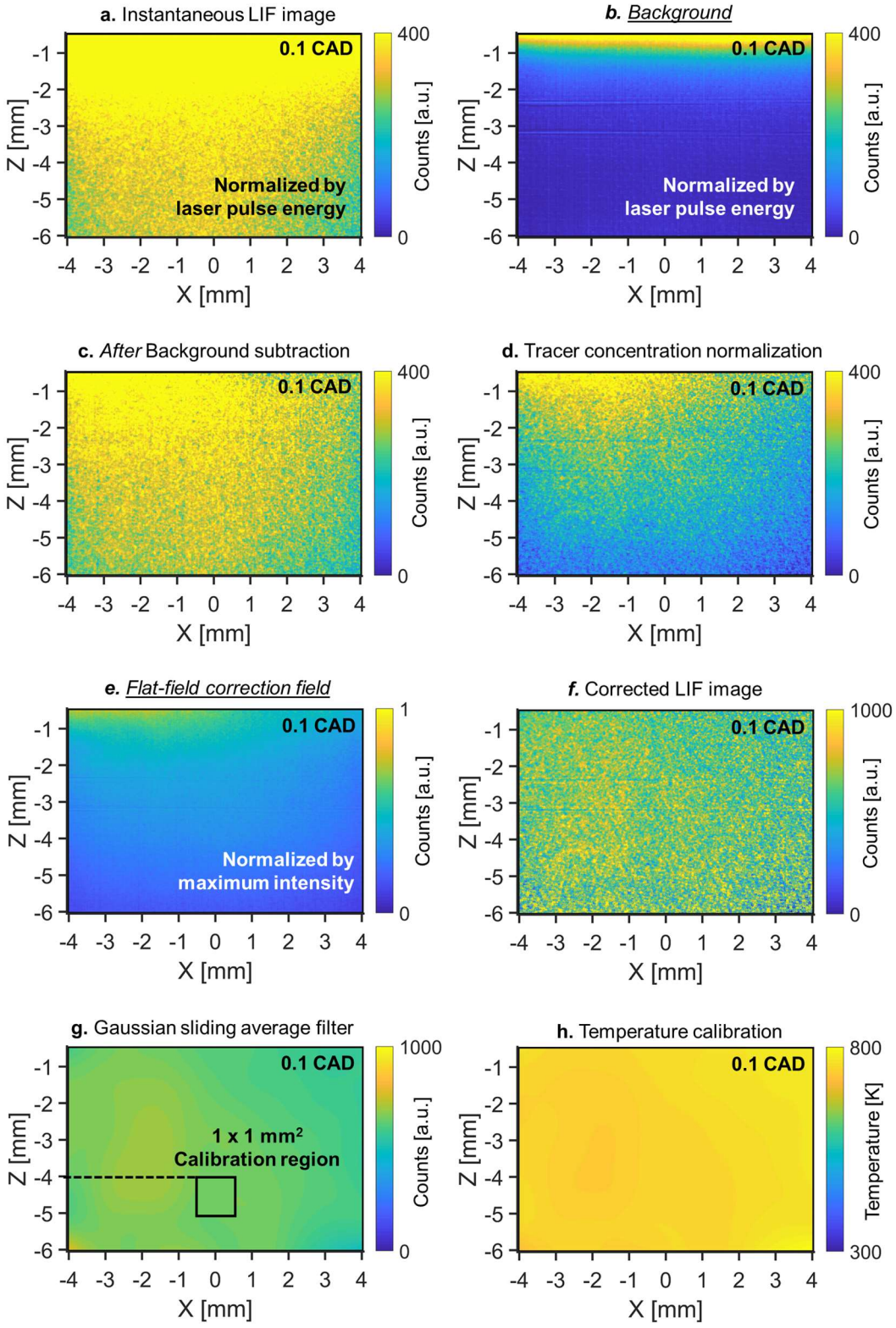

Figure 5-2. Image processing procedure for FFC method.

5.1.3.2 Method 2: Multi-step correction (MSC)

Figure 5-3 shows the post-processing steps applied to correct an instantaneous PLIF image at 0.1 CAD including temperature calibration, and provides the correction fields extracted from the ensemble average image for reference. Instantaneous PLIF images were first normalized by reference laser energy readings before subtracting the background and being normalized by a reference toluene number density at intake valve closing (Figure 5-3.a-d). Light attenuation was not observed in the laser propagation direction, but rather increasing signal towards the in-cylinder head surface caused by reflections of the laser sheet. This was corrected for by evaluating the increase in the central vertical direction within the ensemble average PLIF images, which were also used to extract a correction field of the laser beam profile to correct for non-uniformities in the horizontal direction (Figure 5-3.e-h). These steps were followed by correcting for apparent vertical strips from applying the aforementioned corrections (Figure 5-3.i-j). A moving Gaussian filter of a window size of 1×1 mm^2 was applied to the fluorescence images for noise reduction before calibrating to temperature (Figure 5-3.k-l).

It is important to note here that issues with background signal in the very near-wall proximity persisted in the corrected PLIF images from both correction methods, which prevented reporting any temperature measurements closer than 0.5 mm from the in-cylinder head surface.

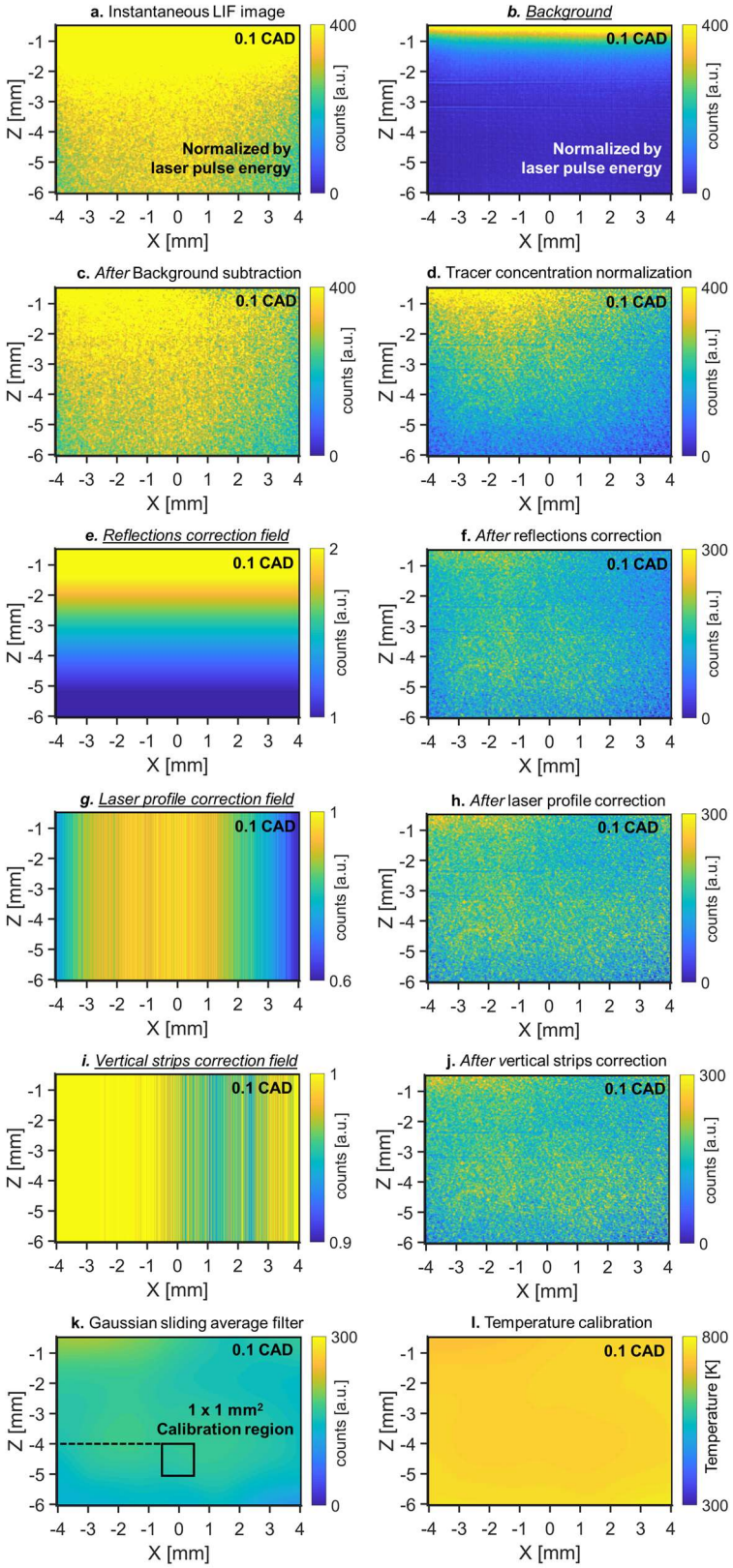

Figure 5-3. Image processing procedure for MSC method.

5.1.4 Background Signal

LIF is generally known to be background-free, i.e. no tracer means no signal. However, this is not the case when operating the engine under fired conditions due to background fluorescence from the chemically excited flame radicals. Figure 5-4 presents background images that were captured under fired conditions at 1300 RPM in the absence of the 266 nm laser sheet and toluene molecules. The first few images capture the spark event, but it is out of focus since the imaging field is about 28 mm farther away from the spark center. The later images capture increasing background fluorescence produced by the chemical excitation of OH in the flame, denoted as OH*, which peaks around 310 nm [121]. This overlaps with the emission spectrum of toluene, and preclude any corrections. Hence, no further analysis will be presented for any of the images acquired after the set ignition timing of -18 CAD.

The ignition system used for this study was of the inductive coil glow-discharge type. Details on the delivered discharge energy and duration can be found in [122], which reported an average duration and electrical energy delivered to the gap of 1.6 ms and 30 mJ, respectively. For this study, the engine was operated under fired conditions without skip firing, and misfired were observed in the recorded consecutive cycles.

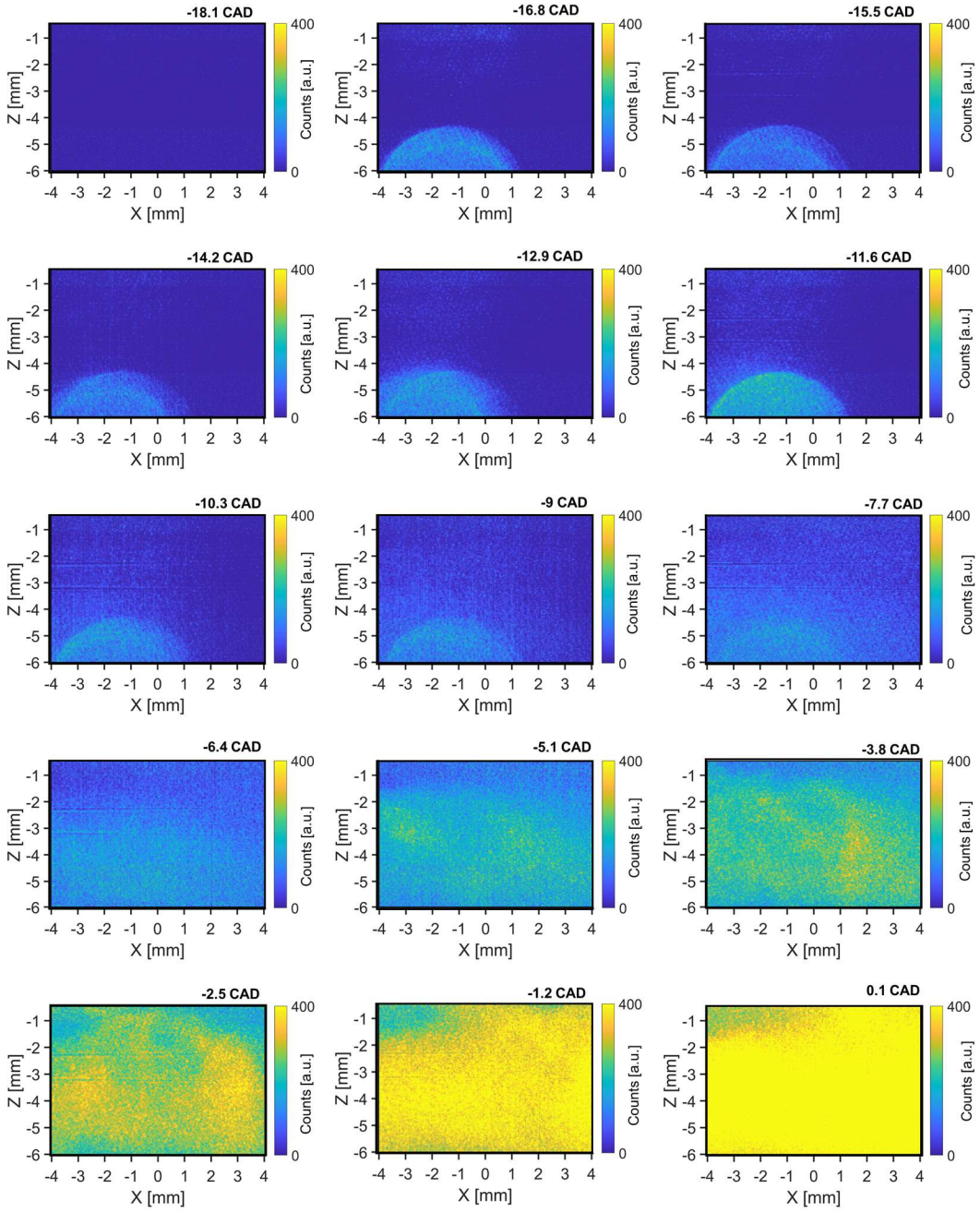

Figure 5-4. Instantaneous background signal from the combustion event at 1300 RPM without laser excitation.

5.1.5 LIF Temperature Calibration

Once all the individual images have been corrected, a calibration is needed to convert LIF intensity into temperature. For each processing method, the spatial average PLIF signal was extracted from a 1×1 mm^2 calibration region in the multi-cycle mean images at a distance of 4 mm

from the surface. LIF signals at each CAD during the compression stroke were then calibrated to predicted in-cylinder temperatures from a 1-D GT-Power simulation tuned to match the experimental pressures during compression within ±5% error, as shown in Figure 5-5. The respective calibration curve for each one-color image processing method are shown in Figure 5-6.

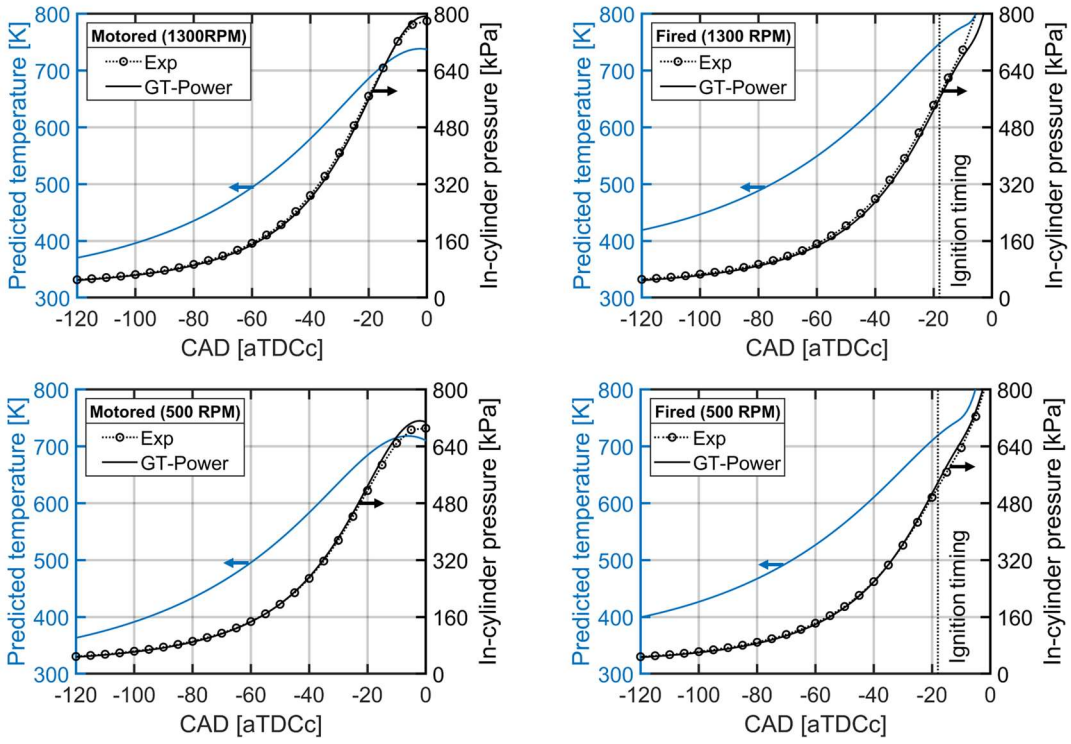

Figure 5-5. In-cylinder pressure measurements and predicted temperatures and pressures from GT-Power.

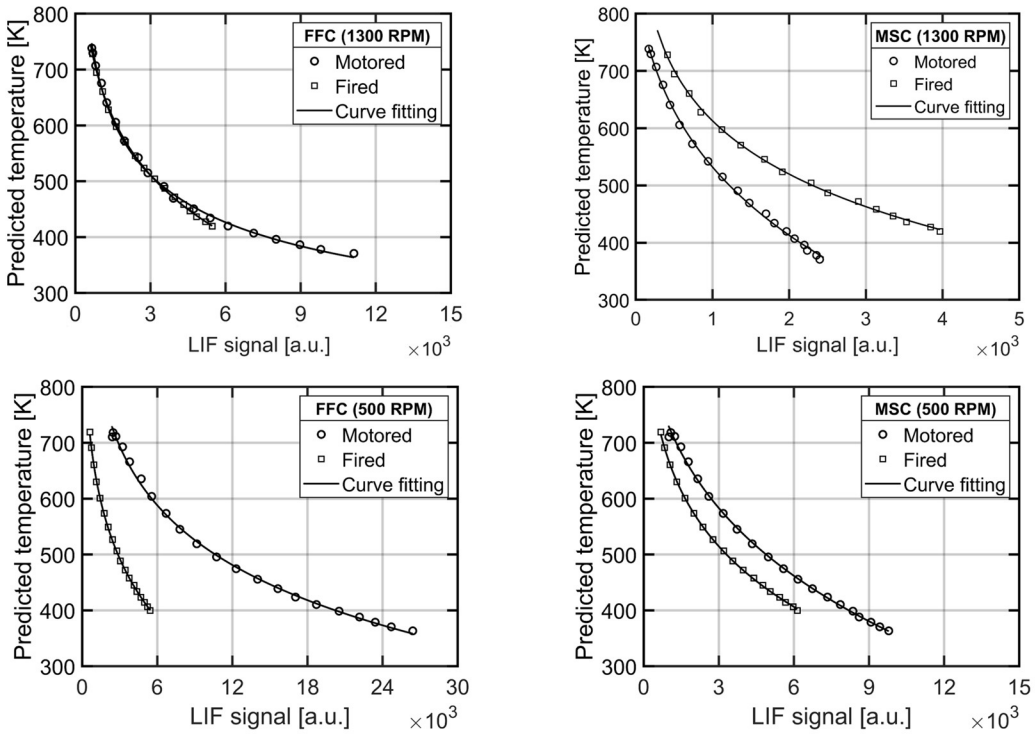

Figure 5-6. Calibration curves for the FFC and MSC correction methods under motored and fired operating conditions at 500 RPM and 1300 RPM.

Choosing the location of the calibration region to be 4 mm away from the wall was guided by the findings of parallel LES efforts with conjugate heat transfer modeling of the TCC-III engine by Wu *et al.* [123]. An analysis was performed by taking a volume average of a cylindrical section in the combustion chamber that is at varied distance (δ) away from the cylinder surfaces. The percent change of the bulk gas temperature as function of CAD and δ is shown in Figure 5-7. A wall distance of 4 mm can be determined from these results to be the extent of the influence from near-wall gases on the bulk gas temperature.

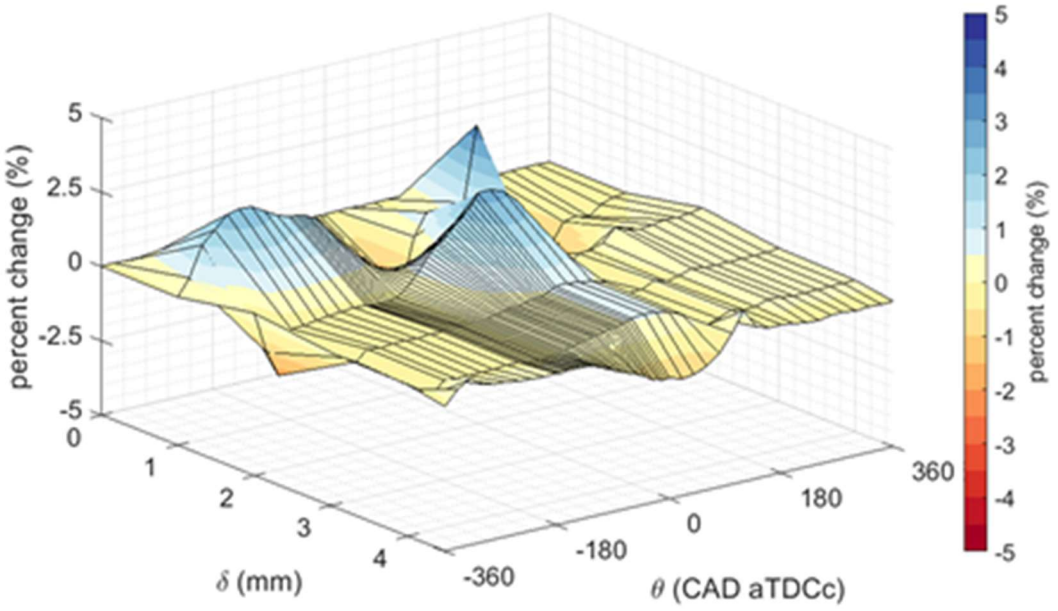

Figure 5-7. Percent change in bulk gas temperature with increasing distance δ from the engine walls (Courtesy of Angela Wu).

5.1.6 LIF Measurement Uncertainties

Random errors originating from intensifier shot noise and variations in laser intensity are the primary sources for precision uncertainty of the PLIF thermometry technique [7, 96, 97, 115, 116]. The PLIF uncertainty was defined as the ratio of standard deviation to the ensemble-average PLIF signal [116], and the corresponding temperature uncertainty was determined from the spatial deviation of temperature fluctuations. PLIF precision uncertainty was found to be around ±7.5% within the calibration region, while the temperature uncertainty was within ±1 K, as can be seen in Figure 5-8. This was evaluated for the FFC method, and larger precision uncertainty occurred as expected closer to TDC due to relatively lower SNR and lower sensitivities at higher temperatures [96, 97, 115, 116].

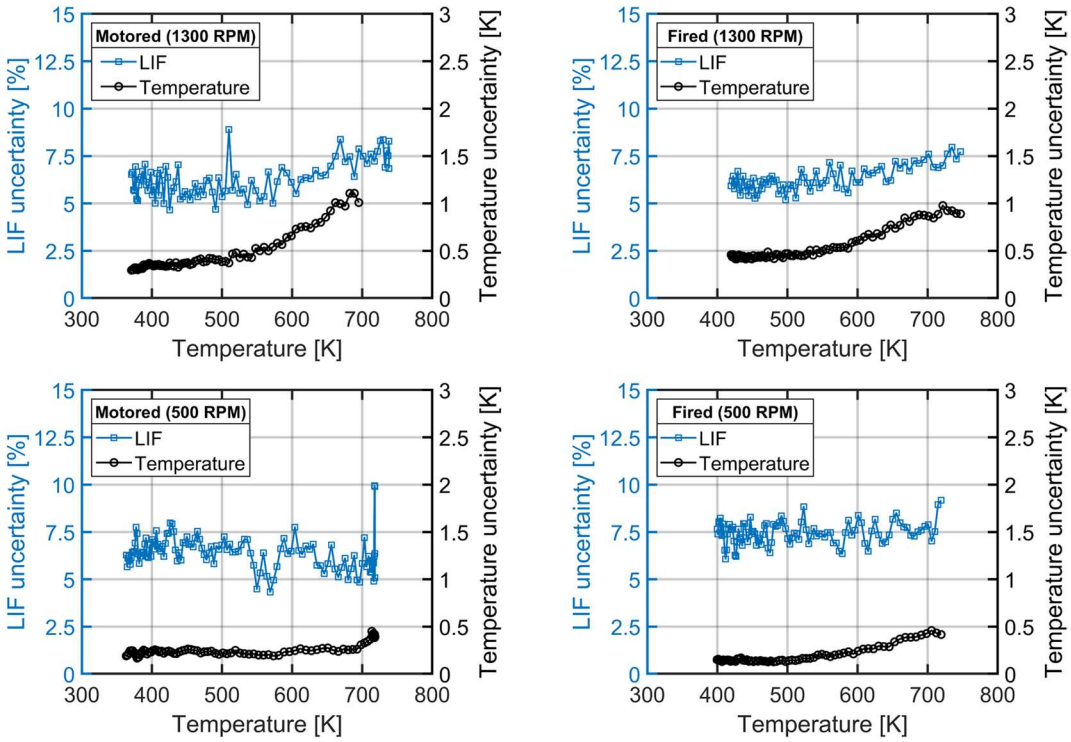

Figure 5-8. LIF precision uncertainty and respective temperature precision uncertainty.

5.2 Results and Discussion

This section examines temperature variations near the in-cylinder head surface in terms of the rise of temperature relative to the surface temperate, the development of fluctuating thermal stratification, line profiles of temperature fluctuations and relative temperatures, in addition to integral length scales based on spatial correlations of relative temperatures.

5.2.1 Temperature Rise during Compression

Temperature fluctuations are expected to increase during compression due to the increasing temperature difference between the in-cylinder flow and the cooled walls [124]. Figure 5-9 shows the rise of the gas temperature in the NWR under motored and fired conditions for two engine speeds at 500 RPM and 1300 RPM, with the respective temperature of the in-cylinder head surface at the heat flux probe location. The gas temperature represent the spatial average value of the 8 x 6 mm^2 imaging field, extracted from the ensemble average temperature distribution using the FFC

method. The surface temperature under motored conditions at both engine speeds about the same as the coolant temperature of 353 K. but it is higher than the coolant temperature by 30 K and 20 K at 1300 RPM and 500 RPM, respectively, due to higher peak temperatures from the combustion event under fired conditions.

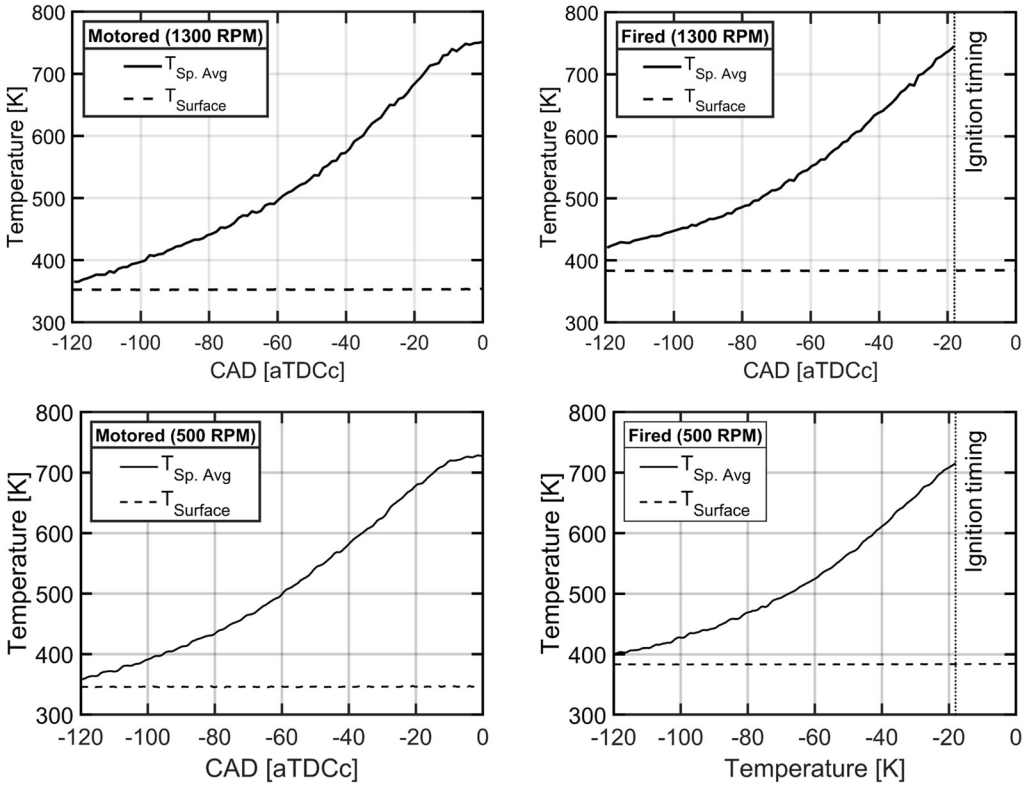

Figure 5-9. Rise of temperature during compression with the respective surface temperature under motored and fired conditions at 500 and 1300 RPM.

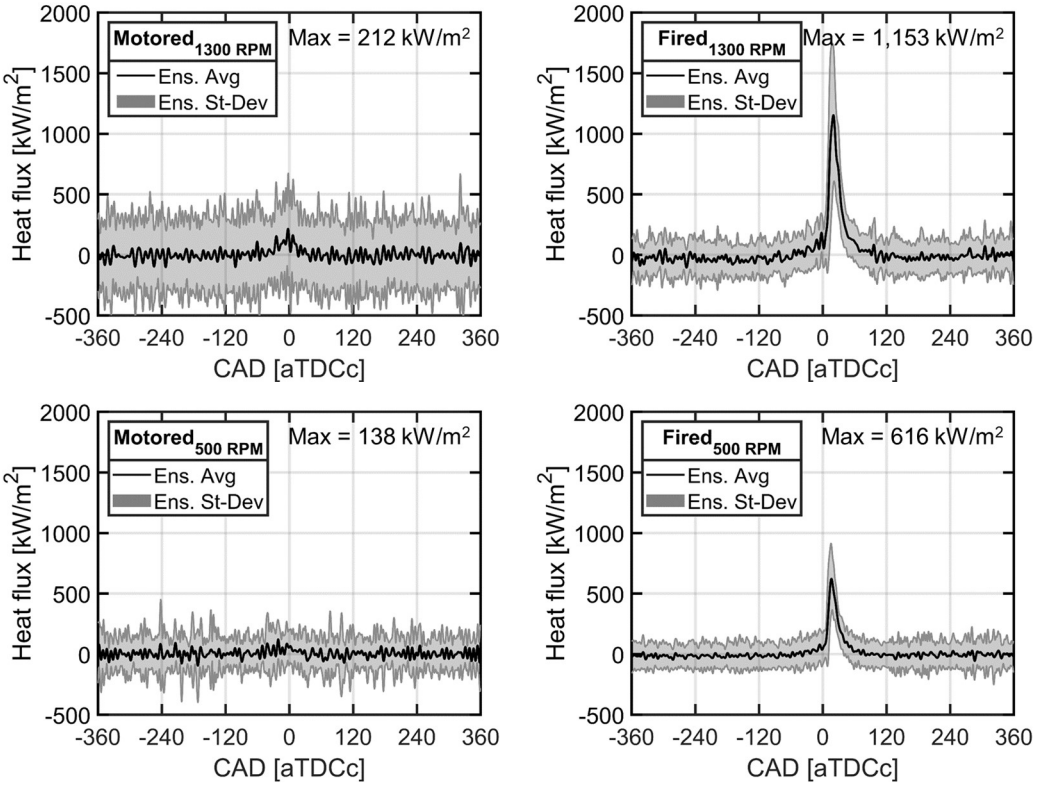

Figure 5-10 presents the heat flux measurements under the different operating conditions. The solid black line represents the ensemble average of all recorded consecutive cycles. For motored conditions, the peak heat flux at 1300 RPM is high than the peak at 500 RPM due to possibly a stronger turbulence, while the heat flux under fired conditions is larger than that under motored conditions because of the combustion event. This is consistent with the previous heat flux measurements reported in [125].

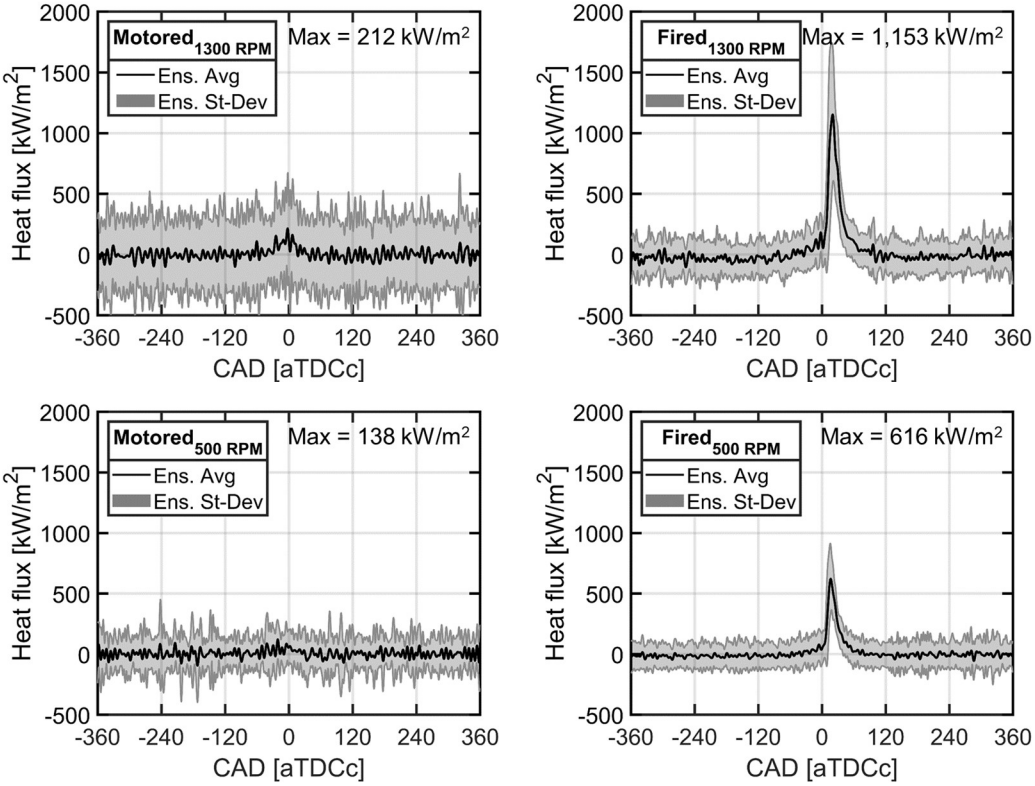

Figure 5-10. Heat flux measurements under motored and fired conditions at 500- and 1300 RPM. Peak heat flux

The work presented in this chapter investigates the development of thermal stratification during compression using LIF thermometry, which is limited up to the ignition timing of -18 CAD [aTDCc] under fired conditions. The heat flux measurements reported above do not indicate any significant differences in the range of -120 to -18 CAD for the considered operating conditions.

5.2.2 Development of Thermal Stratification

Once the LIF signal was calibrated to the predicted temperature, the ensemble-average temperature image was calculated for the FFC method. The ensemble-average temperature image was subtracted from the instantaneous temperature images to yield the temperature fluctuations distribution, which is evaluated in this section. Figure 5-11 illustrates the procedure to obtain the

fluctuating T-map from the instantaneous T-Map at 0.1 CAD under motored conditions at 1300 RPM using the FFC method.

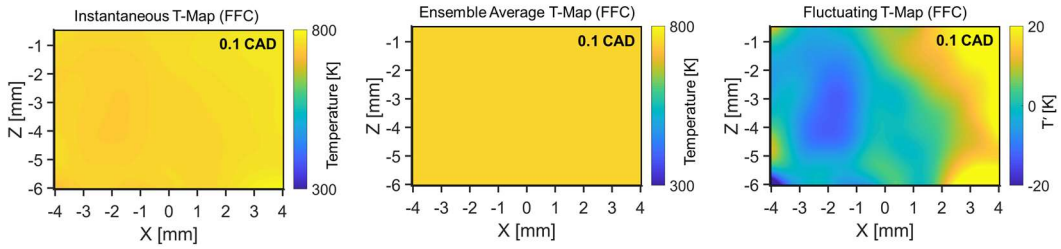

Figure 5-11. Procedure to obtain instantaneous fluctuating temperature distribution from the FFC method.

The development of instantaneous temperature fluctuations during the compression stroke under motored conditions is illustrated in Figure 5-12 for both engine speeds. Images are presented for three selected CADs from a single cycle. It shows larger increasing thermal stratification towards TDC at 1300 RPM than at 500 RPM. This is evident by the increasing number of fluctuating temperature regions and their temperature difference. Figure 5-13 presents instantaneous temperature fluctuations under fired conditions. The single-shot images show the evolution of temperature fluctuations during the compression stroke for both engine speeds, which will be quantified next by the use of probability density functions and spatial standard deviations.

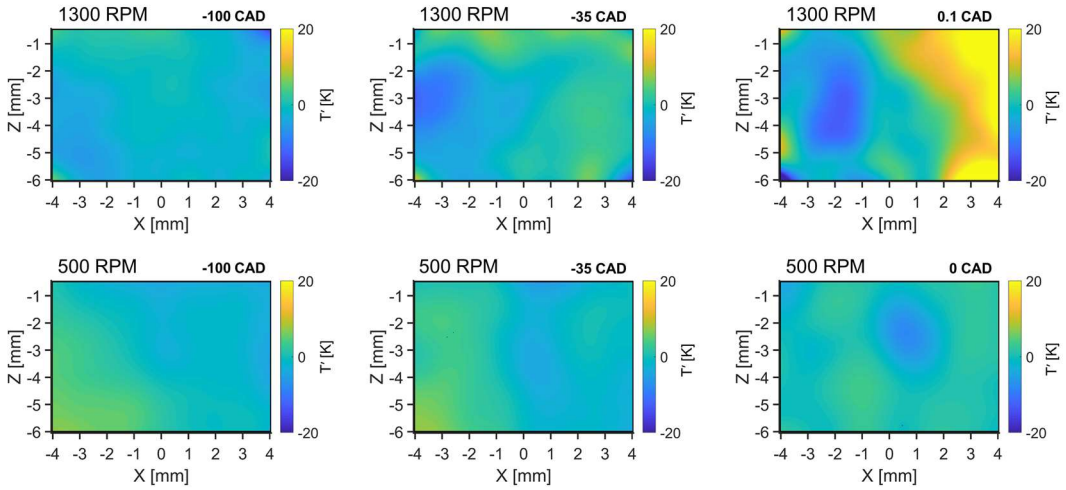

Figure 5-12. Instantaneous temperature fluctuations under motored conditions at 500 and 1300 RPM.

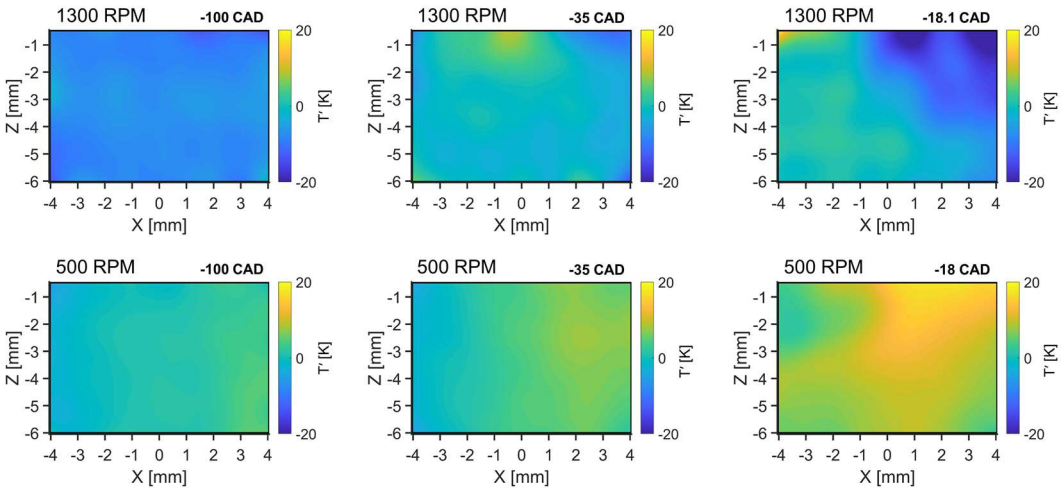

Figure 5-13. Instantaneous temperature fluctuations under fired conditions at 500 and 1300 RPM.

5.2.2.1 Probability density functions (PDFs) of temperature fluctuations

Temporal sequences of temperature fluctuations presented above are useful to visualize the spatial development of thermal stratification. Probability density functions (PDFs) can be used to better quantify the findings for better comparison of the different operating conditions. The PDFs of temperature fluctuations are plotted in Figure 5-14 and Figure 5-15 for the three selected CADs under motored and fired conditions, respectively. The curves were extracted from instantaneous temperature fluctuation distributions, and then ensemble averaged. In general, the curves transition from narrow distribution with pronounced peaks during early compression to wide distributions at the end of compression due to increasing wall heat losses. In addition, the rise in temperature and pressure during compression results in a reduction of the kinematic viscosity, which strongly affects the evolution of turbulence [126]. The decreasing kinematic viscosity results in higher velocity gradients around smaller flow structures, and thus in increased dissipation during compression. The trend is found to be similar under motored and fired conditions. The peak is higher at 500 RPM than at 1300 RPM, which indicates lower temperature fluctuations at the lower engine speed. At 1300 RPM, the evolution of the PDFs appear similar under motored and fired

conditions. This is not the case at 500 RPM. The peak is lower under motored conditions at -100 CAD indicating higher thermal stratification than fired conditions, but it is higher under motored conditions at -35 CAD indicating lower thermal stratification than fired conditions.

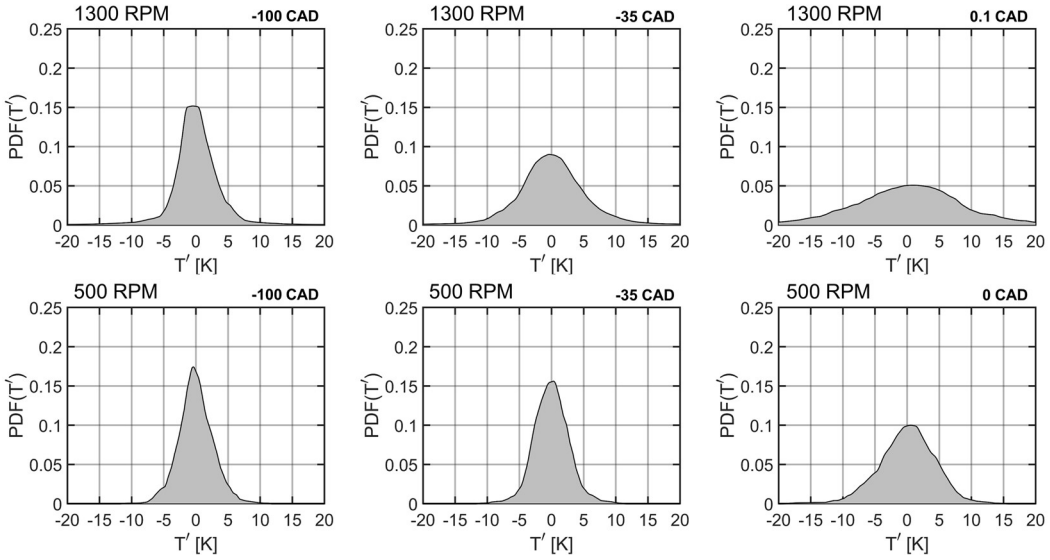

Figure 5-14. Averaged PDFs of temperature fluctuations under motored conditions at 500 and 1300 RPM.

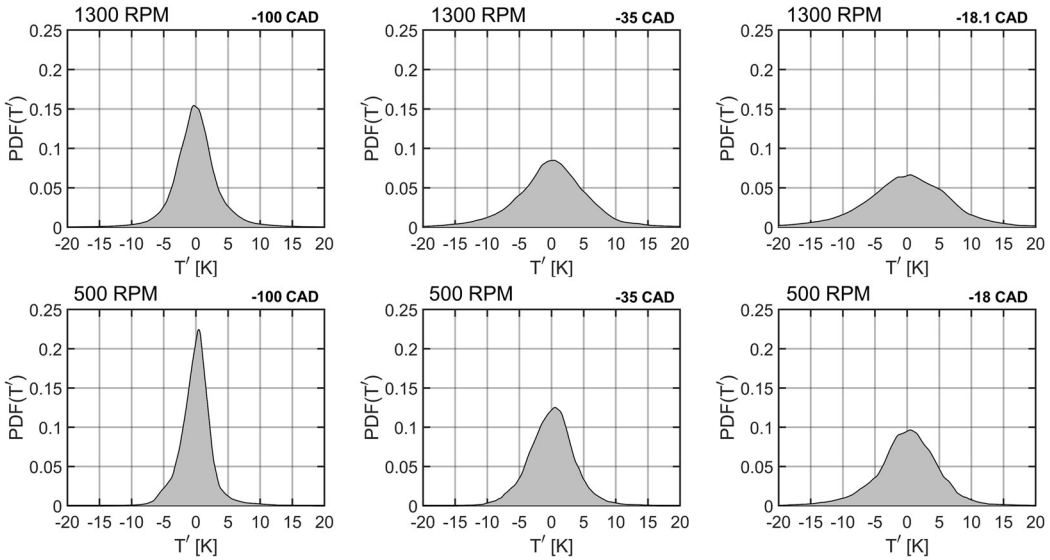

Figure 5-15. Averaged PDFs of temperature fluctuations under fired conditions at 500 and 1300 RPM.

5.2.2.2 Magnitude of the thermal stratification

The spatial standard deviation of temperature fluctuations can be used as a quantitative measure to evaluate the magnitude of the thermal stratification. Figure 5-16 presents the evolution of the magnitude of the thermal stratification under the different operating conditions. The spatial standard deviation of temperature fluctuations was extracted from all instantaneous images at each specific CAD and then ensemble averaged. This describes the fluctuating thermal stratification due to random penetration of turbulent cold structures into the NWR [105]. The magnitude of thermal stratification remains around 2.5 K during early compression for all cases except under motored conditions at 1300 RPM. At 1300 RPM, the magnitude of thermal stratification exhibits an early rise under motored conditions that reaches 5 K by -40 CAD and about 9 K at 0 CAD, while it starts to rise at later in the compression stroke at -80 CAD under fired conditions reaching about 6 K at the ignition timing of -18 CAD. At 500 RPM, the magnitude of thermal stratification starts to rise earlier under fired conditions at about -60 CAD than the stratification under motored conditions that starts to rise at -40 CAD. In a nutshell, thermal stratification is higher at 1300 RPM than 500 RPM. It is higher under motored conditions than fired conditions at 1300 RPM, but the opposite case is true at 500 RPM. These differences can be attributed to differences in turbulent convective transport of colder near-wall gases, and warmer wall under fired conditions [94].

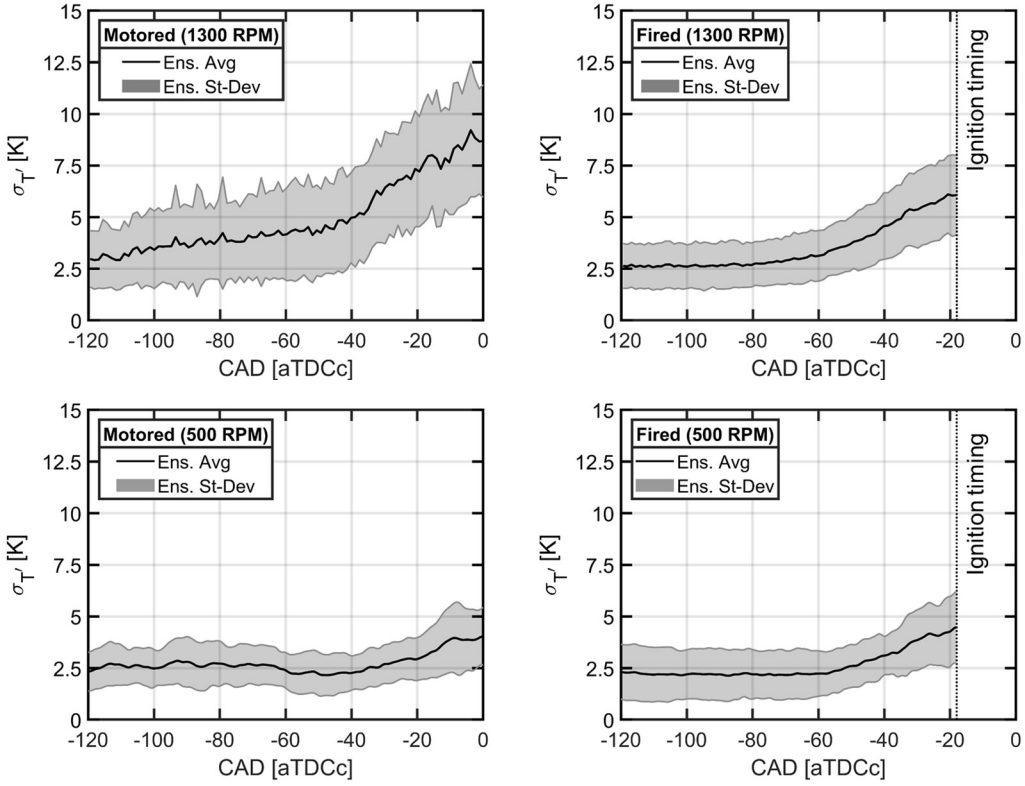

Figure 5-16. Evolution of the magnitude of the thermal stratification.

5.2.3 Temperature Fluctuations Line Profiles

The profiles of the temperature fluctuations in the wall-normal direction can be inspected for their variation with increasing distance from the wall during the compression stroke. Temperature fluctuations are plotted versus the distance from the cylinder head in Figure 5-17 and Figure 5-18 under motored and fired conditions, respectively. These were extracted from the instantaneous temperature fluctuations, and were averaged over the wall-parallel direction before the ensemble averaging. The solid line represent the ensemble average, while the shade represent the ensemble standard deviation of the fluctuations line profiles. Under motored conditions, a clearly recognized maximum can be recognized near the wall at 1300 RPM with a peak increasing from about 15 K at -100 CAD to 30 K at 0.1 CAD. The temperature fluctuations further away from the wall are also increasing towards TDC, which is not observed at 500 RPM as the fluctuations

appear to remain constant with a slightly more recognized maximum near the wall later in the compression stroke at 0 CAD. Under fired conditions, there is no significant increase in the width of the ensemble standard deviation with increasing compression, but a maximum of more than 10 K becomes apparent near the wall at the ignition timing of -18 CAD.

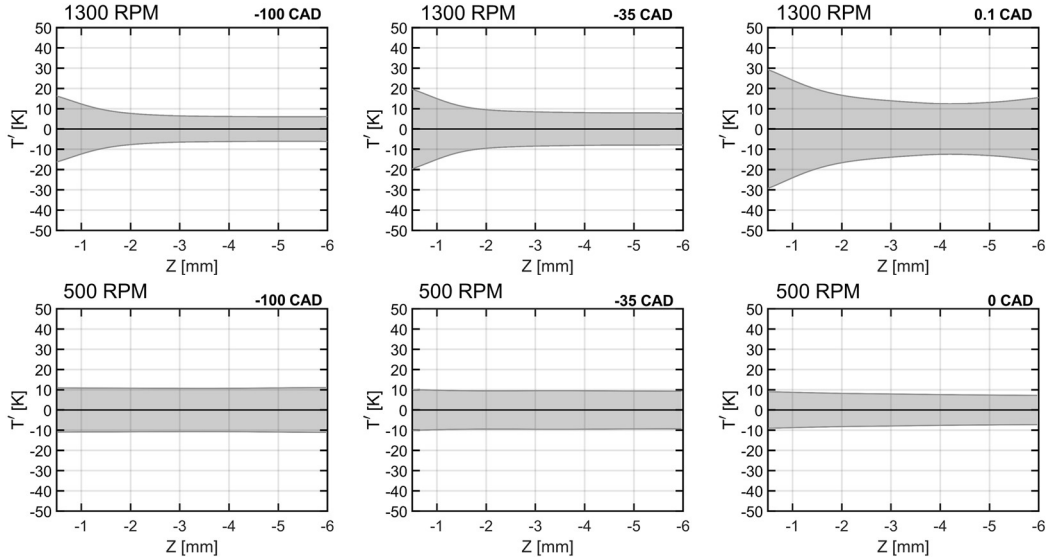

Figure 5-17. Line profiles of temperature fluctuations under motored conditions at 500 and 1300 RPM.

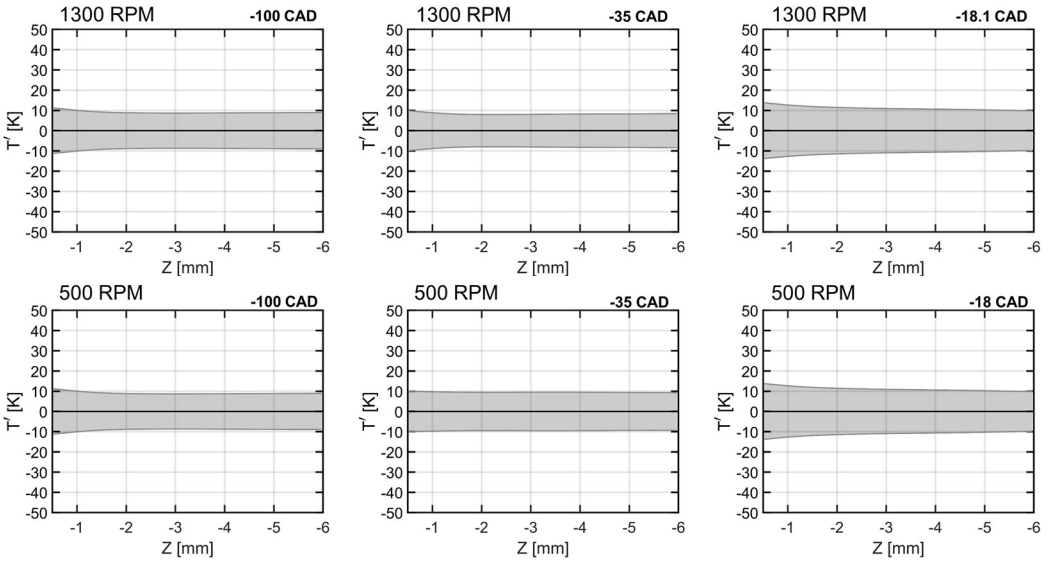

Figure 5-18. Line profiles of temperature fluctuations under fired conditions at 500 and 1300 RPM.

5.2.4 Relative Temperatures Line Profiles

The ensemble average temperature distribution from the MSC method can be used to investigate the temperature distribution that is consistent from cycle-to-cycle at any specific CAD. Figure 5-19 and Figure 5-20 present the relative ensemble temperature distributions under motored and fired conditions, respectively. Temperatures are reported relative to the spatial average value of the imaging field-of-view to reveal the development of the cold boundary layers near the wall.

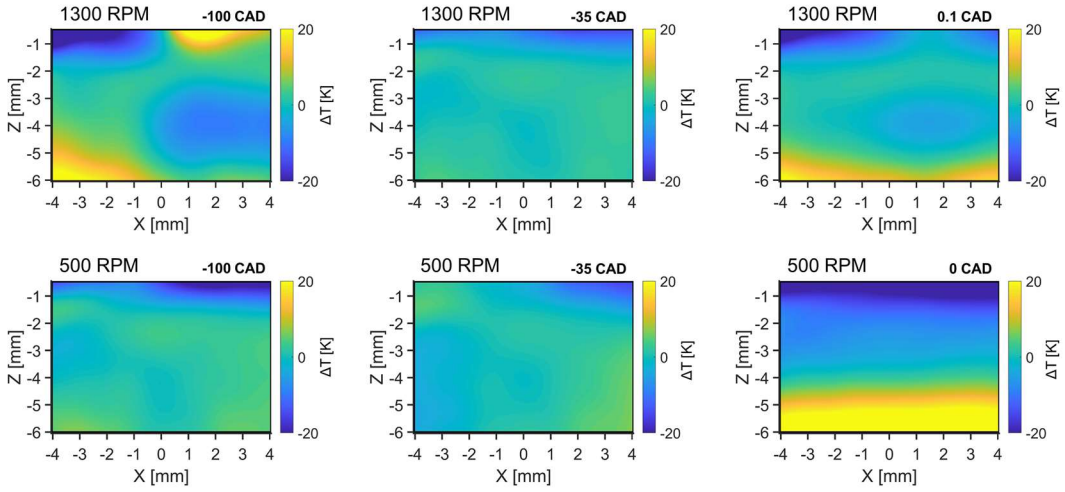

Figure 5-19. Relative ensemble average temperature distribution under motored conditions at 500 and 1300 RPM.

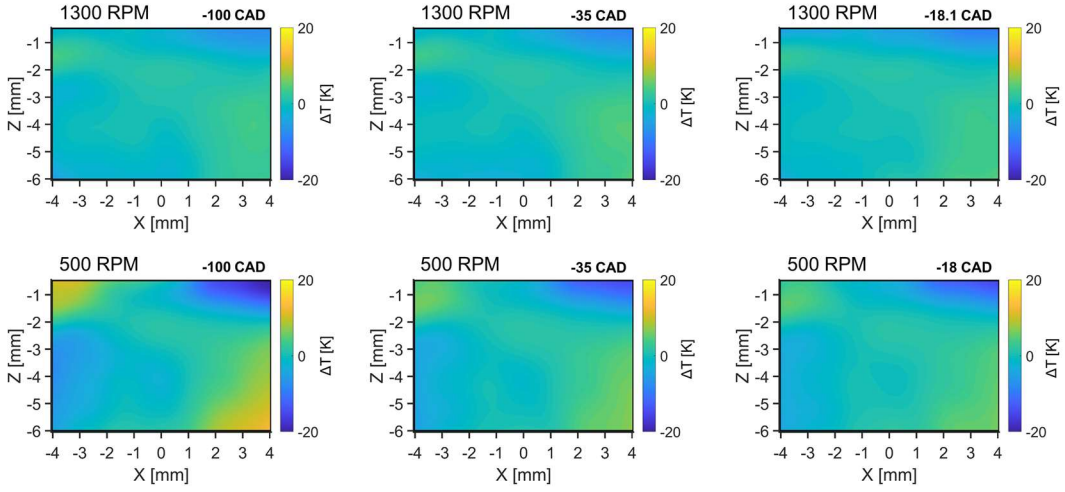

Figure 5-20. Relative ensemble average temperature distribution under fired conditions at 500 and 1300 RPM.

Figure 5-21 and Figure 5-22 show plots of relative temperature profiles in the wall-normal direction, i.e. the Z-direction, derived from the images presented in Figure 5-19 and Figure 5-20, respectively. Solid lines and shades represent the average and the standard deviation over the wall-parallel direction, i.e. the X-direction. All temperature profiles presented here are based on the temperature difference relative to the spatial average temperature of the 8 x 6 mm^2 imaging field. All of the line profiles show colder regions at the in-cylinder head surface. A temperature reversal is observed under motored conditions in all of the line profiles at the engine speed of 1300 RPM under motored conditions, and near the wall at -100 CAD at the engine speed of 500 RPM under fired conditions. A hot region is clearly recognized near the end of the imaging field, i.e. $Z < -4$ mm, at 0 CAD under motored conditions at both engine speeds. The rest of the line profiles exhibit a relatively more stable behavior with nearly 0 K temperature difference in the region farther away from the wall, i.e. $Z < -2$ mm.

Under motored conditions, the temperature difference near the in-cylinder head surface increases towards TDC at 1300 RPM to reach over -10 K at 0 CAD. The behavior is different at 500 RPM as the difference decreases from about -15 K at -100 CAD to -10 K at -35 CAD, before it increases to reach about -25 K at 0 CAD. The difference near the wall is higher at 500 RPM, and the shade is relatively narrower at 500 RPM indicating less variation over the wall-parallel direction. Under fired conditions, the temperature difference near the in-cylinder head surface is similar at both engine speeds, and it increases slightly as the piston moves towards TDC to reach -5 K at 0 CAD. The standard deviation is relatively lower at 1300 RPM, which indicates less variation in over the wall-parallel direction. Interestingly, the temperature difference near the wall is lower under fired conditions than motored conditions, possibly due to warmer walls.

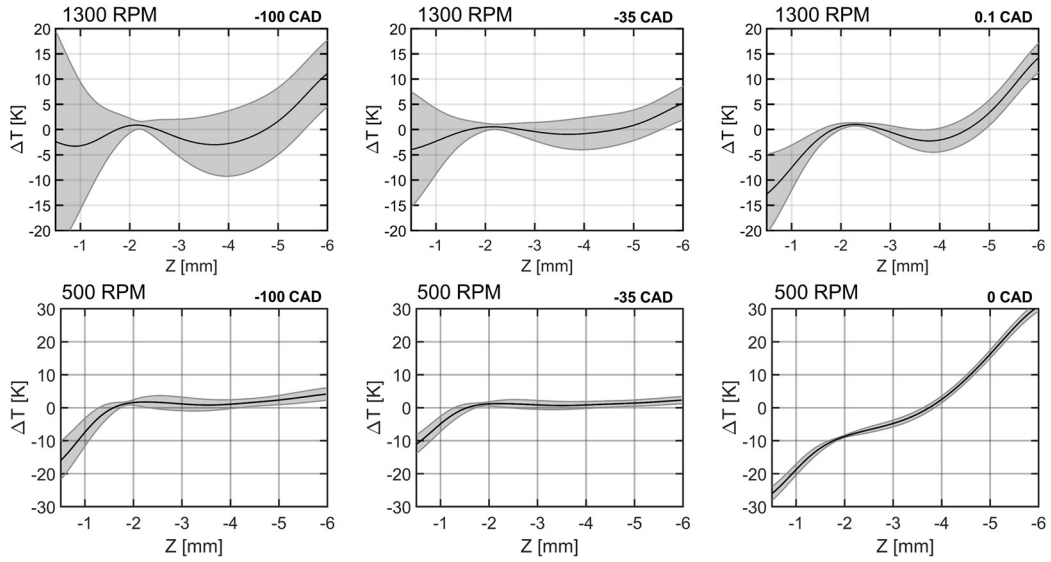

Figure 5-21. Line profiles of relative temperatures under motored conditions at 500 and 1300 RPM.

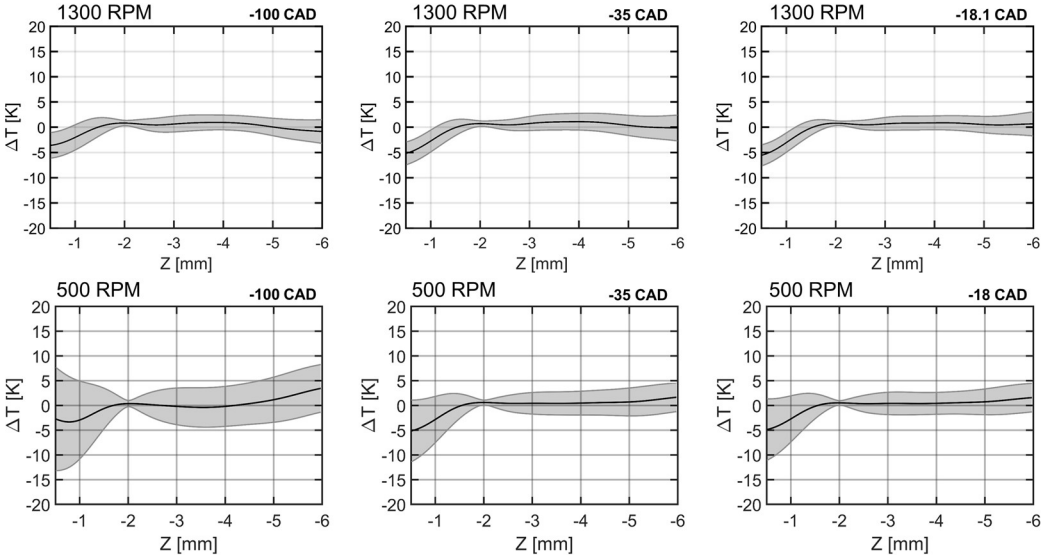

Figure 5-22. Line profiles of relative temperatures under fired conditions at 500 and 1300 RPM.

5.2.5 Integral Length Scale

This section investigates the integral length scales (L_T) of relative temperature (ΔT). Once the LIF images have been calibrated to temperature, the spatial average temperature, denoted by ($\bar{T}$), is subtracted from the instantaneous temperature distribution to yield the relative temperature distribution, as demonstrated in Figure 5-23.

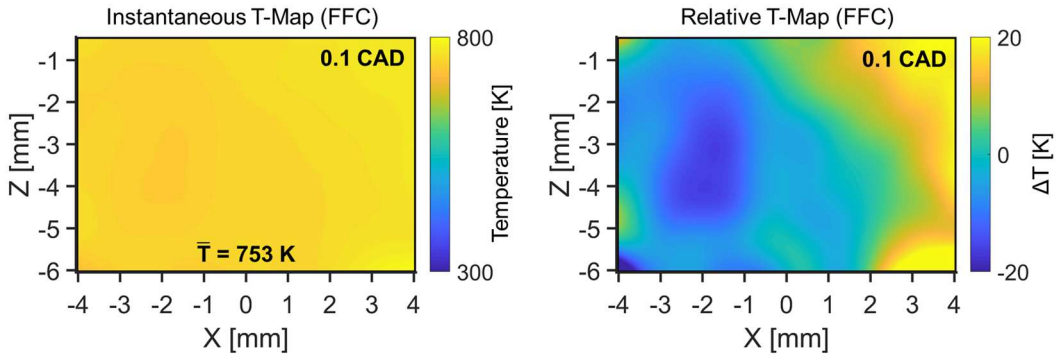

Figure 5-23. Procedure to obtain instantaneous relative temperature distribution from the FFC method.

The integral length scale at a single point is computed by extracting relative temperatures in the wall-normal direction, and calculating its spatial correlation (R) in a single-sided direction using the following equation (5-1) at each specific X location, which was adopted from [127],

$$R = \frac{< \Delta T(Z_o)\, \Delta T(Z_o + \Delta Z) >}{\sqrt{< \Delta T^2(Z_o) >< \Delta T^2(Z_o + \Delta Z) >}} \tag{5-1}$$

Where Z_o is the correlation point, ΔZ is the correlation distance, ΔT is the relative temperature, and the brackets represent the ensemble average over the consecutive cycles. The spatial correlation curves were fit with a stretched exponential decay function with non-linear least square method to achieve a zero-crossing point for all the spatial correlation curves following the equation (5-2),

$$f(Z) = e^{-AZ^B} \tag{5-2}$$

Where A and B are the fitting coefficients. Figure 5-24 presents examples of the spatial correlation curves for -100, -35, and 0.1 CAD along with the fit function at several distances from the wall along the vertical line of $X = 0\, mm$. The fit function was then integrated as in equation (5-3) to obtain the integral length scale using the trapezoidal method,

$$L_T = \int_0^{\infty} f(Z)\, dZ \tag{5-3}$$

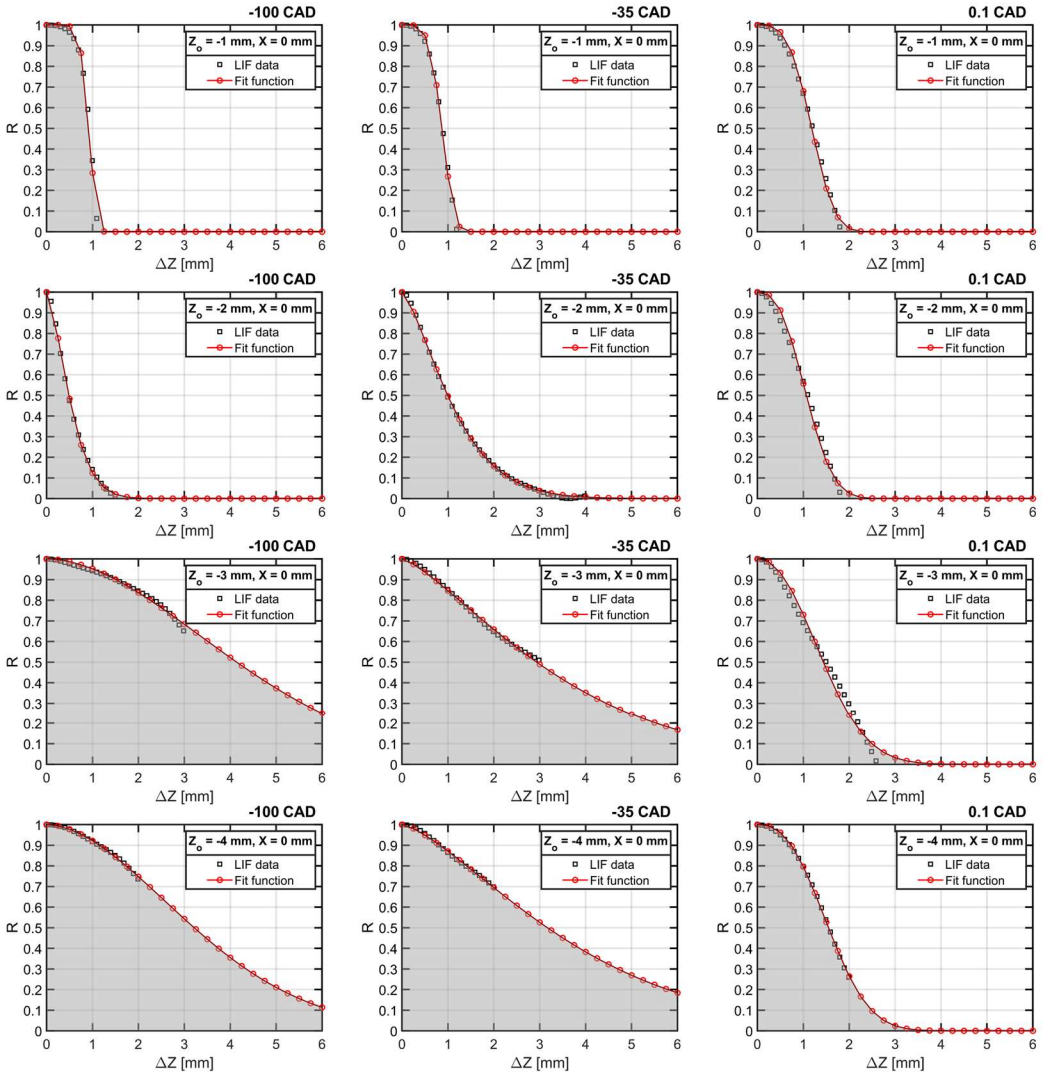

Figure 5-24. Spatial correlations along with stretched exponential decay fits for several points at difference distances from the wall for three selected CADs under motored conditions at 1300 RPM.

Figure 5-25 and Figure 5-26 present the integral length scale distributions under motored and fired operating conditions, respectively, along with plots their line profiles versus the wall-normal direction for a clear comparison. The line profiles represent the average value of the integral length scales over the wall-parallel direction, and the standard deviation is represented by the shade. The values farther away from the wall (Z < -4 mm) are not shown due to decreasing number of statistically independent sample points as the correlations points approach the end of the imaging field-of-view.

The temperature integral length scales behave differently with increasing wall distance for the considered engine operating conditions, but their distributions become more homogenous towards TDC. They appear to decrease monotonically with increasing compression, except under motored conditions at 500 RPM. Under motored conditions, the length scales are relatively small near the wall at 1300 RPM and they start to get larger after a distance of about 2 mm farther from the wall. Under fired conditions, the length scales exhibit a clear increase in the near-wall proximity at -100 before they decrease farther away for Z < -1 mm. The length scales decrease towards TDC as they become more uniform and similar, but they remain marginally larger under at the lower engine speed.

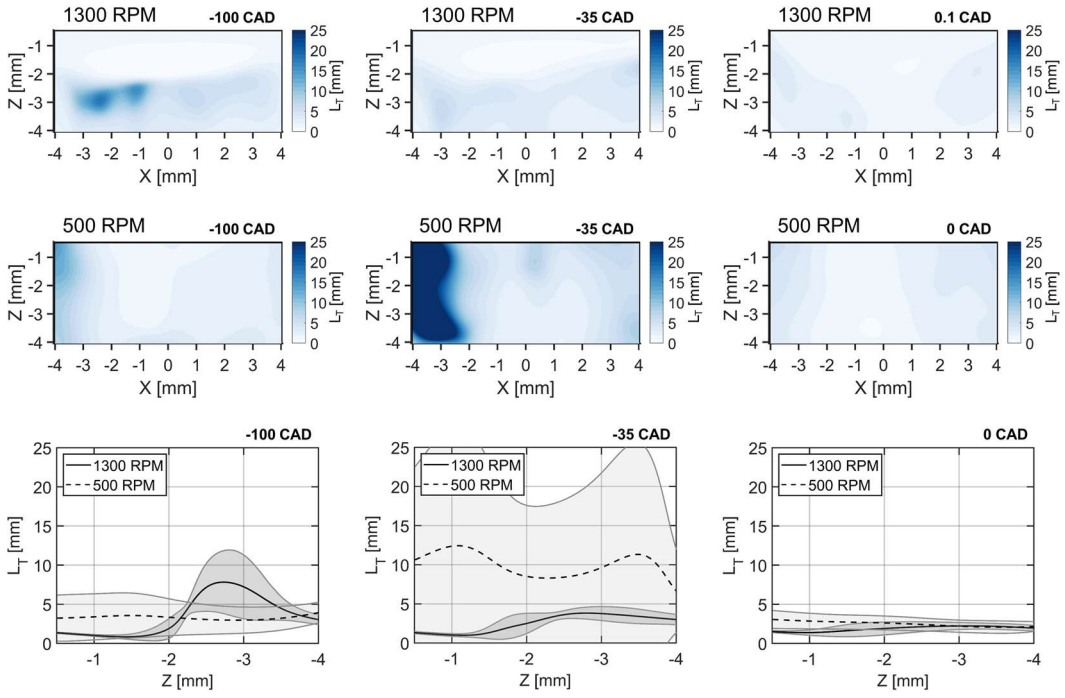

Figure 5-25. Integral length scales of relative temperatures under motored conditions at 500 and 1300 RPM. Line profiles of the integral length scales versus the wall-normal direction are shown on the bottom row.

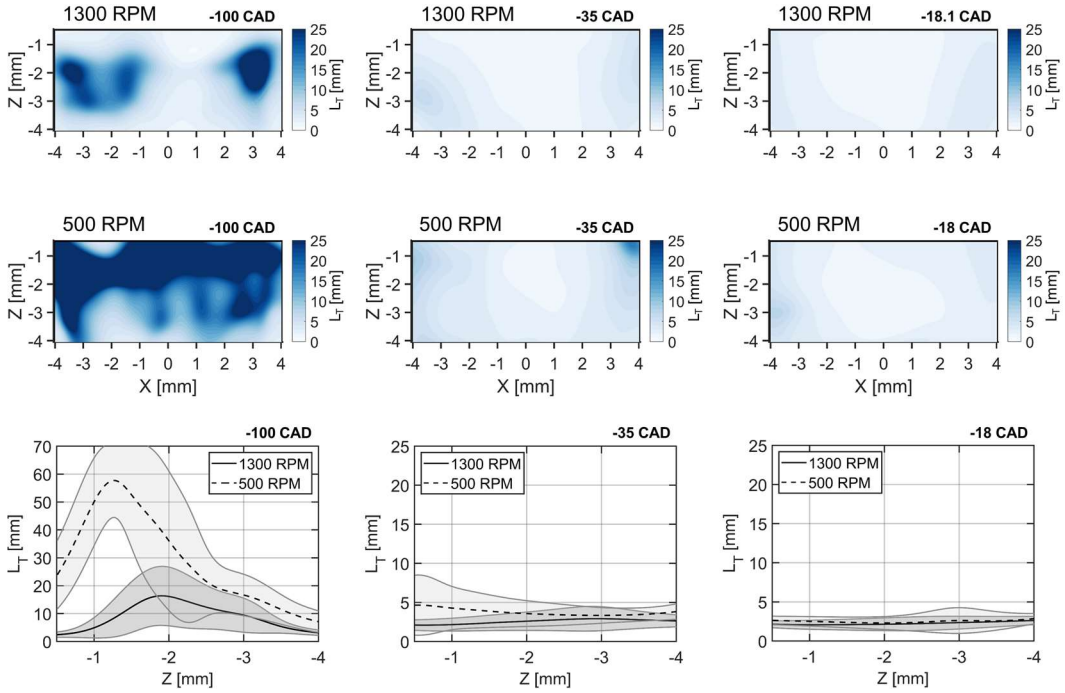

Figure 5-26. Integral length scales of relative temperatures under fired conditions at 500 and 1300 RPM. Line profiles of the integral length scales versus the wall-normal direction are shown on the bottom row.

5.3 Collaborative Assessment of Temperature Variations in the NWR

This section investigates near-wall temperature fluctuations in collaboration with parallel efforts in numerical conjugate heat transfer (CHT) modeling of the TCC-III engine by Angela Wu. A commercial CFD software (CONVERGE v.2.4.18) was used to perform large eddy simulation (LES) under motored conditions, and CHT modeling was used to obtain the surface temperature at the fluid-solid interface. Details of the numerical model setup can be found in [123].

In this collaborate assessment, temperature fluctuations are defined about the multi-cycle mean, following common practice in literature. These fluctuations increase during compression as a result of increasing temperature difference between the in-cylinder flow and the cooled walls [124]. Figure 5-27 shows the rise of the gas temperature in the NWR under motored and fired conditions, alongside the temperature of the in-cylinder head surface at the heat flux probe

location. These temperatures are the spatial average value of the multi-cycle mean temperature distributions extracted from the 8 × 6 mm^2 field-of-view. Numerical results are in a good agreement with measurements under motored conditions in terms of capturing the temperature rise in the NWR and predicting the surface temperature, mainly due to the inclusion of the CHT model.

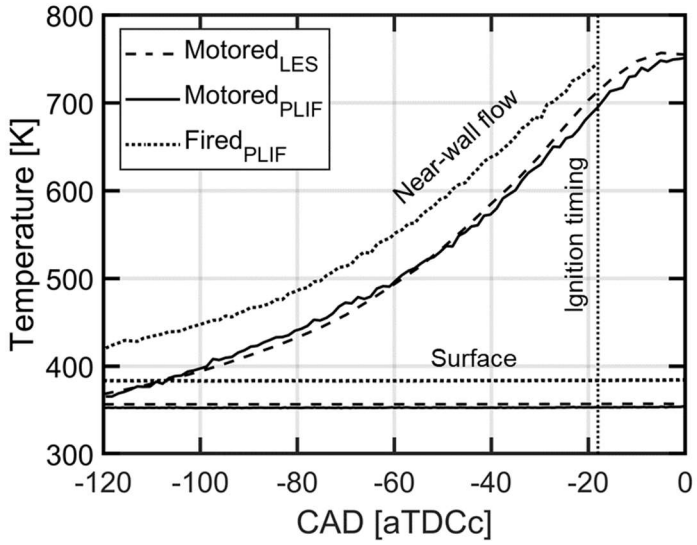

Figure 5-27. Temperature rise in the NWR during compression under motored and fired conditions.

Figure 5-28 presents instantaneous images of temperature fluctuations during the compression stroke, and each row represents a temporal sequence of a single-cycle, with the first row being results from LES, and second and third rows are LIF results under motored and fired conditions. The spatial coordinates in this collaborative effort have been changed to match the coordinates of previous near-wall velocity measurements of the TCC-III engine by Greene [27]. The distance in the wall-parallel and wall-normal directions are denoted by x_{Head} and y_{Head}, respectively. The wall- Instantaneous temperature fluctuations are valuable to examine since they affect the combustion phasing and maximum peak release rate [115, 116, 128]. Increasing thermal stratification towards TDC is evident by the increasing number of fluctuating temperature regions and their temperature difference. Numerical results do not capture any significant stratification in

the NWR during early compression, but show higher temperature fluctuations during late compression.

The repeatability of patterns observed in the instantaneous images is assessed by inspecting the multi-cycle standard deviation (not shown) [7]. Multi-cycle standard deviation values increase with compression due to increasing fluctuations, and the regions of the largest cycle-to-cycle temperature fluctuations, as outlined by the dashed lines on Figure 5-28, are closer to the in-cylinder head surface where high thermal gradients are expected to occur. The dashed lines represent 65% of the maximum multi-cycle standard deviation value at each CAD. This further confirms the unsteadiness of the thermal boundary layer at the in-cylinder head as observed in [115].

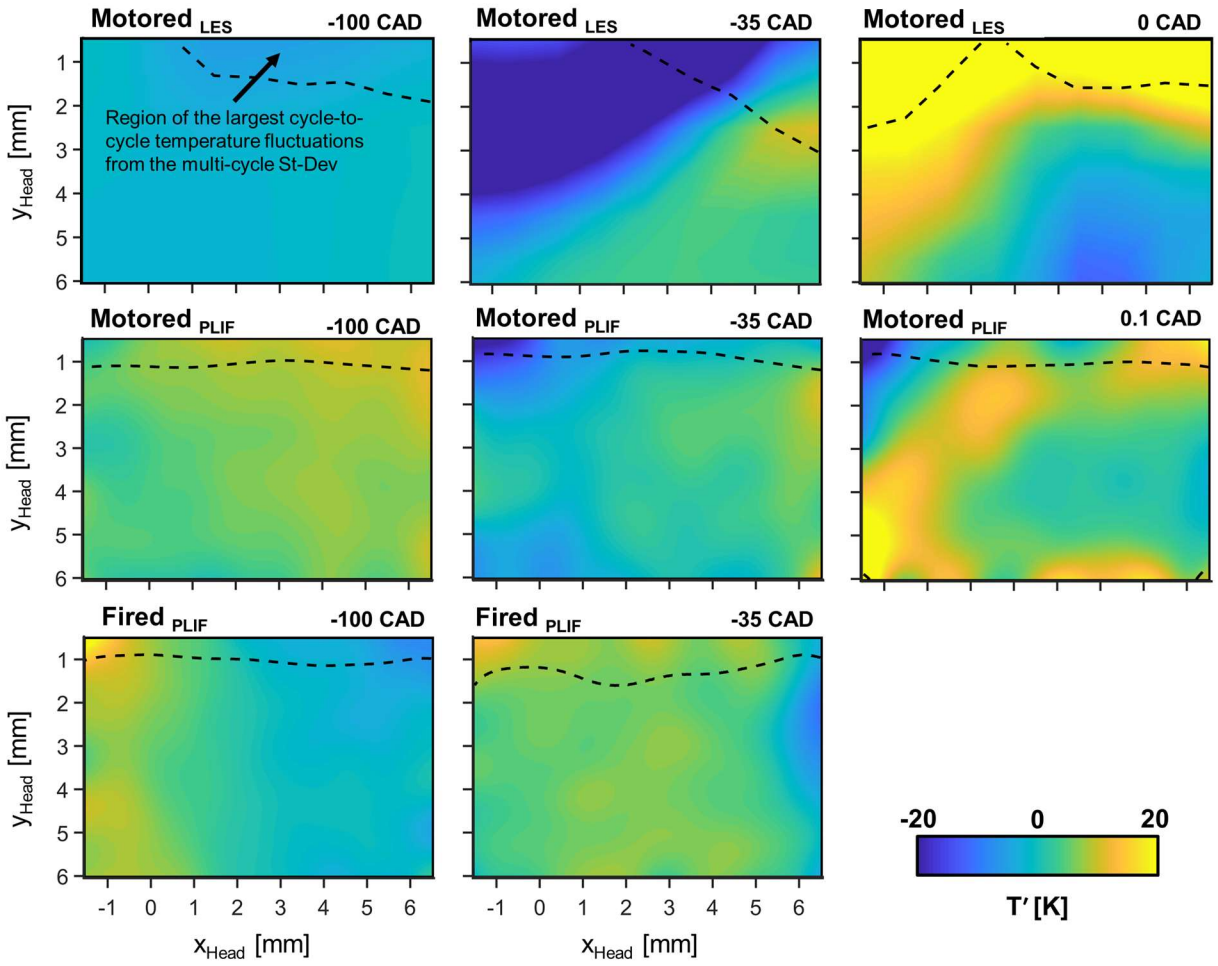

Figure 5-28. Temporal evolution of thermal stratification in the NWR during compression under motored and fired conditions. Regions of the largest cycle-to-cycle temperature fluctuations, indicated by the highest multi-cycle St-Dev, are confined in-between the in-cylinder head surface and the dashed lines.

Temperature fluctuations about the multi-cycle mean include effects of turbulence and CCV [129]. To further assess their cyclic variability, Figure 5-29 presents probability density functions (PDFs) of near-wall temperature fluctuations for multiple consecutive cycles. While these PDFs describe temperature fluctuations in the NWR, they reveal similar effects of compression on in-cylinder temperature as reported in [126]. The PDF (T′) transitions from narrow distributions with pronounced peaks during early compression, indicating low temperature fluctuations, to wide and dispersed at the end of compression due to increasing wall heat losses. The curves appear to be skewed and multimodal as a result of interaction with colder near-wall fluid in the NWR [7, 126].

The spread of fluctuating temperatures appears to be similar under motored and fired conditions. Numerical results follow the same trend but show less fluctuations than measurements during early compression.

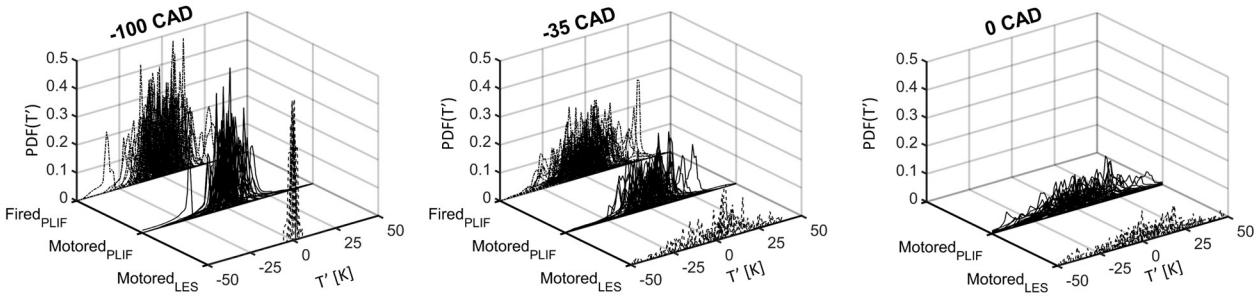

Figure 5-29. PDFs of fluctuating temperature in the NWR (each curve represents a single cycle).

Thermal stratification is expected to develop across the in-cylinder core region during late compression, when the bulk-gas temperature has risen well above the wall temperature [7, 128]. However, stratification in the NWR is likely to develop earlier during compression because of closer interaction with colder gases. Figure 5-30 presents the spatial standard deviation of fluctuating temperatures in the NWR. It quantifies the magnitude of the fluctuating thermal stratification ($\sigma_{T'}$) during compression caused by random penetration of turbulent cold structures into the NWR [7]. Lines and shaded areas represent the multi-cycle mean and standard deviation values, respectively. Experimental results exhibit early fluctuations in the compression stroke with a gradual rise towards TDC. Fluctuating stratification is higher under motored conditions than fired, which could be due to differences in turbulent convective transport of colder near-wall gases. Numerical results show minimal fluctuations early in the compression stroke, but a steep rise after -90 CAD leading to higher fluctuations than measurements during late compression.

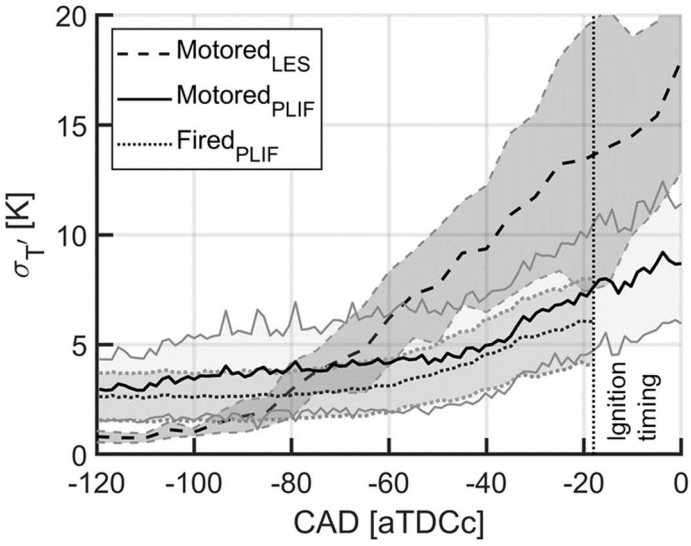

Figure 5-30. Evolution of fluctuating thermal stratification in the NWR.

Spatial correlation analysis of temperature fluctuations in the NWR is valuable for validating wall heat transfer models. It provides insights into the spatial scale of fluctuating temperature structures [7] and describe near-wall thermal gradients [126, 130]. Moreover, it could be used to identify the extent of the wall boundary effect [127].Figure 5-31 presents single-sided, two-point spatial correlation coefficients of temperature fluctuations in the wall-normal direction for the correlation point y_{Head} = 0.5 mm, following the method described in [127]. Lines and shaded areas represent the average and standard deviation over the wall-parallel direction (x_{Head}).

Results show strong correlations in the near-wall proximity where the largest cycle-to-cycle temperature fluctuations are confined, but they experience an initial drop outside of the buffer layer, identified in [89, 119]. Correlations under fired conditions are stronger, indicating larger integral length scales and less thermal gradients in the NWR compared to motored conditions. This is commensurate with velocity measurements that show higher fluctuations in the NWR for fired operation [119], which would help to decrease thermal gradients through mixing enhancement. Also, they vary less in the wall-parallel direction, indicated by the shaded areas, in contrary to the

motored conditions. Correlations from LES experience a stronger initial drop within the NWR, at the same wall distance, pointing to smaller temperature length scales in the simulations compared to the measurements.

In general, these correlations remain statistically dependent within the NWR, which necessitates a larger imaging field to extract meaningful integral length scales for cross-comparison with DNS results reported by Schmitt *et al.* [124, 130]. Their work investigated fluctuations around the spatial mean, and revealed decreasing temperature length scale towards the wall at TDC due to increasing thermal gradients.

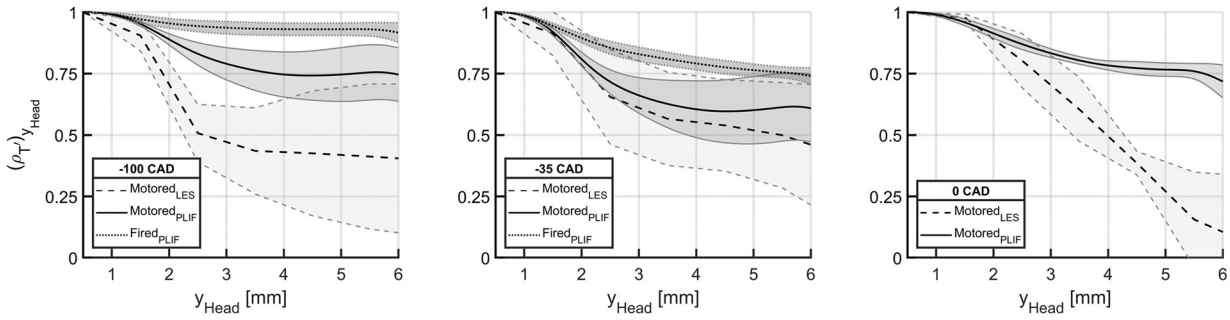

Figure 5-31. Two-point spatial correlations of temperature fluctuations in the wall-normal direction. Lines and shaded areas represent the average and spatial standard deviation values in the wall-parallel direction, respectively.

This collaborative effort investigated near-wall temperature fluctuations in the TCC-III engine using a combined LIF thermometry and numerical CHT modeling approach. Instantaneous fluctuating temperature fields showed good agreement between numerical and experimental results in terms of increasing thermal stratification towards TDC. Largest cycle-to-cycle temperature fluctuations were identified closer to the in-cylinder head surface indicating the unsteadiness of the thermal boundary layer. PDFs of near-wall temperature fluctuation provided an assessment of the cyclic variability, in addition to capturing the effects of compression on temperature fluctuations. Thermal stratification under motored and fired conditions were not

significantly different before ignition timing. Lastly, spatial correlations of temperature fluctuations in the wall-normal direction provided an indication of their spatial scales. It revealed strong correlations in the near-wall proximity that remained statistically dependent in the NWR. Interestingly, these correlations are higher under fired conditions, compared to motored conditions, indicating larger temperature length scales, when defined based on fluctuations about the multi-cycle mean. This could be due to higher bulk-gas temperatures and velocity fluctuations under fired operating conditions as observed in previous near-wall PIV measurements of the TCC-III engine.

5.4 Summary

The development of thermal stratification near the NWR of the TCC-III engine was investigated under motored and fired conditions at two different engine speeds of 500 and 1300 RPM, within an 8 x 6 mm field-of-view adjacent to the in-cylinder head surface. Visual inspection of instantaneous temperature fluctuations shows increasing thermal stratification towards TDC that is more predominant under motored conditions and at the higher engine speed. A PDF analysis of the images provided a more quantitative evaluation of the observed trends, which showed similar development of temperature fluctuations under motored and fired operating conditions. The magnitude of the fluctuating thermal stratification was also examined for the different cases. The earliest development of stratification was observed under motored conditions at 1300 RPM, then under fired conditions at the same speed. This is opposite to the stratification at 500 RPM that increased earlier under fired operation than motored conditions. Line profiles of temperature fluctuations in the wall-normal direction peaked near the in-cylinder head surface, with a clearly defined maximum under motored conditions at 1300 RPM that increased with increasing compression. The development of the outer boundary layer was investigated too by examining the

relative temperature line profiles, with respect to the spatial average temperature of the imaging field, in the wall-normal direction. These show increasing temperature differences near the in-cylinder head surface towards TDC. Largest differences were observed under motored conditions at the lower engine speed. Additionally, integral length scales of relative temperatures were inspected in the wall-normal direction. They were found to decrease towards TDC as they become more uniform and similar, but appeared larger in general at the lower engine speed. The findings of this work enabled the collaborate assessment of temperature fluctuations in the NWR with parallel efforts in numerical conjugate heat transfer (CHT) modeling of the TCC-III engine by Angela Wu. The noticed mismatches between measurements and simulations could be attributed to several modeling factors and experimental inaccuracies. The LES results are dependent on the wall heat transfer models, the subgrid scale model, the numerical scheme, and the grid resolution, while the LIF temperature measurements are influenced by the accuracy of the temperature calibration, and any background fluorescence signal due to reflections. However, the overall trend in the spatial correlations of experimental temperature fluctuations in the NWR was well captured in the LES.

Chapter 6 Conclusions and Future Work

Understanding engine heat transfer can reduce net carbon emissions while enabling the design of more efficient engines with advanced operational strategies. This requires a significant investigation into the transient thermal boundary layer effects in order to accurately characterize the heat transfer processes associated with the NWR. This work utilized a laser-based imaging diagnostic to reveal the development of thermal stratification at two measurement locations near the cylinder head surface of the TCC-III engine using high-speed toluene LIF thermometry.

In summary, the first measurements investigates the development of thermal stratification under motored operating conditions within a 20 x 12 mm^2 field-of-view. Temperature fluctuations first appear near the in-cylinder head causing increasing temperature inhomogeneities during compression that reach its maximum at TDC and persist to a lesser extent in the expansion stroke. Temperature fluctuations from multiple consecutive cycles at TDC show evident cycle-to-cycle variations that are the largest near the piston surface. Line profiles of relative temperatures in the wall-normal direction reveal colder regions near the walls with increasing temperature difference towards TDC that are larger near the cylinder head surface.

The second part of this work investigates temperature variations under motored and fired operating conditions at two different engine speeds within an 8 x 6 mm^2 field-of-view, corresponding to previously-collected near-wall velocity measurements as reported in [119]. Results show increasing temperature fluctuations during compression with similar development under motored and fired conditions that is larger in magnitude at the higher engine speed. Largest cycle-to-cycle variations in temperature fluctuations are identified near the wall that are most evident under motored conditions at the higher engine speed. Line profiles of relative temperatures

reveal lower temperature differences near the wall under fired operating conditions. Integral length scales of relative temperatures in the wall-normal direction decrease towards TDC as they become more uniform and homogenous in their distribution.

The near-wall temperature measurements presented in this thesis provide unique insights into the spatial and temporal temperature variations in the NWR of an operating reciprocating engine, which were enabled by rigorous experimental effort and attentive post-processing steps. Temperature images are obtained from high-speed toluene LIF measurements using the one-color detection technique, and the calibration procedure is based on predicted in-cylinder temperature from an engine simulation software (GT-Power). Precision uncertainty is assessed within a 1 x 1 mm^2 calibration region, and found to be within ±2 K. These measurements add to the continuous effort to extend the fundamental understanding of near-wall engine heat transfer, and aid in achieving a more comprehensive characterization of the NWR by complementing the previously-collected velocity measurements.

The scope of this work was focused on investigating the overall development of thermal stratification in the NWR under varied engine operating conditions, but there remains tremendous valuable possibilities to further analyze these near-wall temperature measurements. Thermal stratification could be examined differently by being based on variations in relative temperatures instead of temperature fluctuations, which would reveal the spatial temperature variations driving the instantaneous heat flux rather than the cyclic variations. The analysis could also inspect single-cycle thermal stratification separately to identify important characteristic patterns than are not clear in the ensemble average. Also, integral length scales could be explored in the wall-parallel direction to study the anisotropy in the temperature variations.

Additionally, temperature variations are caused by the increasing temperatures during the compression stroke, and are strongly influenced by velocity fluctuations and the evolution of turbulence. The findings of this work can be explored in-depth with the local flow fields from the previously-collected near-wall velocity measurements to further assist in characterizing the turbulent heat flux close to the wall.

Moreover, the near-wall temperature measurements can be used as a basis to develop or improve existing engine wall heat transfer models by comparing the experimental findings to numerical predictions. Such comparisons allow to effectively improve LES turbulence models in internal combustion engines by identifying possible sources of discrepancy and potential improvements. The near-wall temperature measurements of this work were examined against the predictions of LES with conjugate heat transfer modeling of the TCC-III engine by Wu *et al.* [123] to assess the capability of LES models and mesh resolutions to capture temperature variations in the NWR. Disagreements in the simulated temperature fields were attributed to the choice of the subgrid scale model and the grid resolution, in addition to shortcomings in the Han and Reitz heat transfer model that was developed with a RANS turbulence model. Similarly, these measurements provide useful insights that can be used to validate direct numerical simulations (DNS) in engine-like geometries. The findings of this work agree in general with the results reported in [131] despite differences in geometries and operating conditions, where increasing pressure during compression was found to have a strong effect on the flow leading to increasing temperature gradients at the walls and smaller turbulent length scales due to a reduction in the kinematic viscosity.

On the other hand, physical insights from numerical methods could guide experimental investigations by possibly identifying any errors that must be taken into future consideration. Primary errors of the LIF temperature measurements are associated with the accuracy of the

calibration procedure and the post-processing steps to correct the LIF images, besides any local LIF signal variations due to inhomogeneous toluene mixture that cannot be distinguished using the one-color detection method utilized in this work. Also, numerical methods offer volumetric information of the whole engine cylinder while the laser-based experimental methods are generally limited to the two-dimensional imaging plane.

Improvements to the experimental methodology are certainly required to disentangle the issue of background fluorescence due to reflections and allow for highly-resolved temperature measurements in the very near-wall proximity. Suppression of such background signals in the LIF images might require improved techniques in planar laser imaging, such as the Structured Laser Illumination Planar Imaging (SLIPI) where the laser sheet is spatially modulated. Other improvements include using the two-color detection technique to avoid any bias in the one-color measurements from mixture inhomogeneities. However, two-color images exhibit relatively large precision uncertainties and would require higher signal-to-noise levels in order to detect thermal gradients at high temperatures.

Future work should consider performing simultaneous measurements of near-wall velocity and temperature fields to provide full characterization of the boundary layer effects. That would entail many experimental challenges including synchronization, laser sheets alignments, and setting up multiple high-resolution imaging systems in a limited space close to the engine cylinder. In addition, the studies of near-wall engine flow could be significantly extended with simultaneous spatial measurements of the surface temperature.

Lastly, these measurements could be further verified by examining the development of thermal stratification under varied loads and conditions. Exploring higher engine speeds and loads is restricted by the operating limits of optical engines, and it would require improvements in terms

of engine design and the optical components to further push these limits. It would also be of interest to the engine research community to extend the investigation of near-wall LIF temperature measurements for different engine geometries and combustion modes including spark-ignition (SI) or compression-ignition (CI) engines with direct injection (DI) and more complex piston geometry. This would allow examining the impact of temperature variations in the NWR on inhomogeneous mixtures in their tendency to ignite, and possibly indicating regions with favorable conditions to ignite first.

Appendix A Image Processing

Appendix A provides further details of the image processing procedure used in Chapter 4. LIF images at every 0.5 CAD were recorded for 14 consecutive cycles under motored conditions at an engine speed of 500 RPM. The image processing procedure is derived from two image processing methods, denoted as the "flat-field correction" (FFC) [13, 94, 96, 116] and the "multi-step correction" (MSC) methods [105, 116].

A.1 Instantaneous LIF Image

The instantaneous LIF image can be considered to be a function of the crank-angle degree (CAD), the engine cycle, and two spatial coordinate position, $I_{\{CAD = M, Cycle = N\}}(X, Z)$, where I is the signal intensity count of the image at the coordinate position (X, Z), at M CAD from cycle N. The coordinate position (X, Z) can be termed a pixel. For the purpose of this Appendix, we will consider the case of an instantaneous LIF image at 0 CAD [aTDCc] from cycle 7, $I_{\{CAD = 0, Cycle = 7\}}(X, Z)$, shown in Figure A- 1.

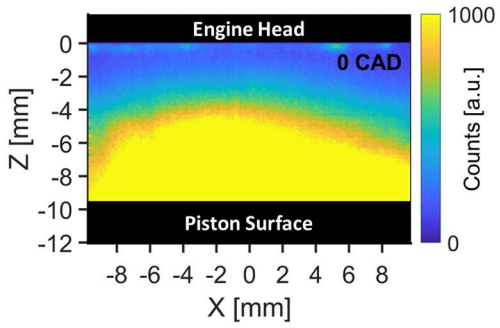

Figure A- 1. Instantaneous LIF image at 0 CAD from cycle 7.

A.2 Normalization by the Laser Pulse Energy

The instantaneous LIF image is first normalized by a reference laser energy reading from a photodiode device placed near the laser beam path. Figure A-2 shows values of laser energy readings at 0 CAD for 14 consecutive engine cycles, normalized by their average value.

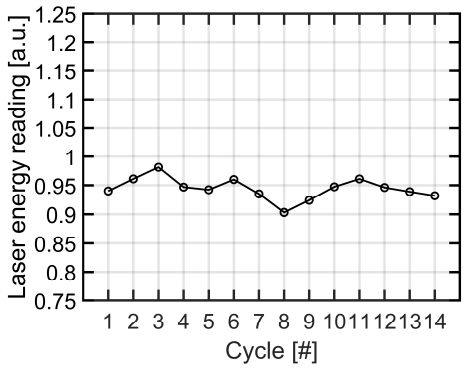

Figure A- 2. Normalized laser pulse energy readings at 0 CAD for 14 consecutive engine cycles. Each pulse laser energy reading corresponds to an instantaneous LIF image.

Each instantaneous LIF image is divided by its respective laser energy reading, to correct for variations in pulse-to-pulse laser energy, using equation (A-1),

$$I_{LP\,\{CAD=M,Cycle=N\}}\,(X,Z) = \frac{I_{\,\{CAD=M,Cycle=N\}}\,(X,Z)}{LP_{\,\{CAD=M,Cycle=N\}}} \tag{A-1}$$

Where $I_{LP\,\{CAD=M,Cycle=N\}}\,(X,Z)$ represents an instantaneous LIF image after the normalization by the laser pulse energy, $I_{\,\{CAD=M,Cycle\quad\}}\,(X,Z)$ is an instantaneous LIF image, and $LP_{\,\{CAD=M,Cycle\quad\}}$ is the reference laser energy reading corresponding to the instantaneous LIF image.

A.3 Tracer Concentration Correction

After normalization by the laser pulse energy, the instantaneous LIF image is corrected for changes in tracer number density during the compression and expansion strokes. Figure A-3 shows

the tracer number density from intake valve closing (IVC) to exhaust valve opening (EVO), assuming a fixed tracer mass between the valve events, normalized by its maximum value at TDC.

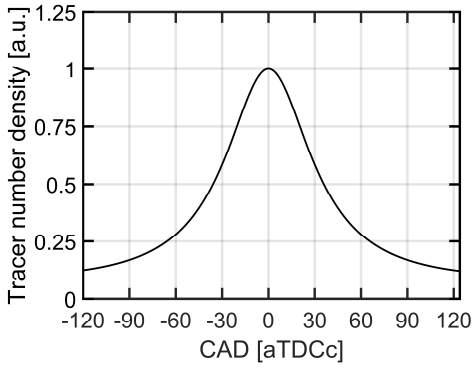

Figure A- 3. Normalized tracer number density from IVC to EVO.

Each instantaneous LIF image is divided by its respective tracer number density value to apply the tracer concentration correction, using equation (A-2),

$$I_{TC\ \{CAD=M,Cycle=N\}}\ (X,Z) = \frac{I_{LP\ \{CAD=M,Cycle=N\}}\ (X,Z)}{TC\ _{\{CAD=M\}}} \tag{A-2}$$

Where $I_{TC\ \{CAD=M,Cycle\ \ \}}\ (X,Z)$ represents the instantaneous LIF image after the tracer concentration correction, $I_{LP\ \{CAD=M,Cycle\ \ \}}\ (X,Z)$ is the instantaneous LIF image after the normalization by the laser pulse energy, and $TC\ _{\{CAD=M\}}$ is the reference tracer number density corresponding to the instantaneous LIF image. The next image processing steps are specific to the correction method used.

A.3.1 Flat-field correction (FFC) Method

The FFC method utilizes a multi-cycle mean LIF image normalization to correct for laser attenuation and other image nonuniformities. The flat-field correction field at each specific CAD can be found using equation (A-3),

$$I_{FFC\ \{CAD=M\}}\ (X,Z) = \frac{< I_{TC\ \{CAD=M\}}\ (X,Z) >}{\overline{< I_{TC\ \{CAD=M\}} >}} \tag{A-3}$$

Where $I_{FFC\,\{CAD=M\}}(X,Z)$ represents the flat-field correction field, $< I_{TC\,\{CAD=M\}}(X,Z) >$ is the ensemble-average LIF image after the tracer concentration correction, and $\overline{< I_{TC\,\{CAD\quad\}} >}$ is the spatial average of the ensemble-average LIF image after the tracer concentration correction. The flat-field correction field is normalized by its respective spatial average value to allow the absolute LIF intensity in the instantaneous LIF image to be preserved in the corrected LIF image. Then, the instantaneous LIF image, after the tracer concentration correction, is corrected using the flat-field correction (FFC) method according to equation (A-4),

$$I_{Corrected,FFC\,\{CAD=M,Cycle=N\}}(X,Z) = \frac{I_{TC\,\{CAD=M,Cycle=N\}}(X,Z)}{I_{FFC\,\{CAD=M\}}(X,Z)} \tag{A-4}$$

Where $I_{Corrected,FFC\,\{CAD=M,Cyc\quad\}}(X,Z)$ represents the corrected instantaneous LIF image using the FFC method, $I_{TC\,\{CAD=M,Cycle=N\}}(X,Z)$ is the instantaneous LIF image after the tracer concentration correction, and $I_{FFC\,\{CAD=M\}}(X,Z)$ is the flat-field correction field. The image processing procedure for the FFC method is illustrated in Figure A-4 for an instantaneous LIF image at 0 CAD.

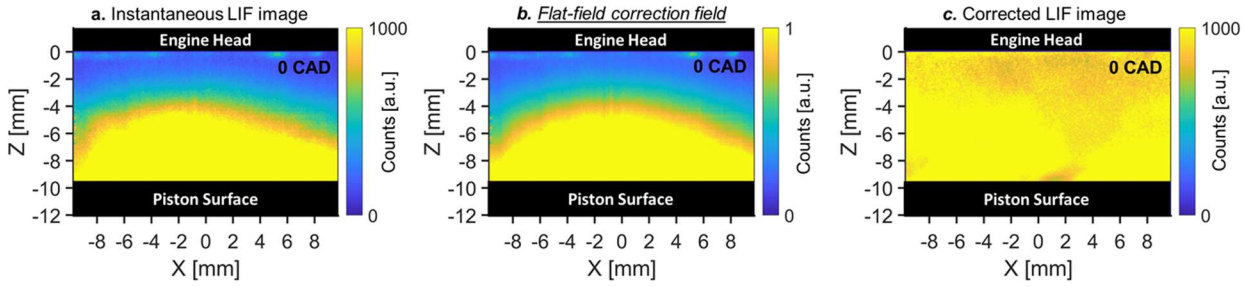

Figure A- 4. Image processing procedure using the FFC method for an instantaneous LIF image at 0 CAD from cycle 7.

A.3.2 Multi-step correction (MSC) Method

The image processing procedure for the MSC method involves the derivation of three correction fields for light attenuation, laser beam profile, and vertical strips by evaluating the ensemble-average LIF images at each CAD, after the tracer concentration correction.

First, light attenuation is examined in the laser propagation direction by evaluating the drop in the signal intensity towards the cylinder head surface in the Z-direction. The light attenuation correction field at each specific CAD can be determined by inspecting the ensemble average LIF image using equation (A-5),

$$I_{LA\,\{CAD=M\}}\,(X,Z) = \frac{\overline{< I_{TC\,\{CAD=M\}}\,(Z) >}}{\overline{< I_{TC\,\{CAD=M\}}(Z_o) >}}, -8 \le Z \le -2, Z_o = -8 \qquad \text{(A-5)}$$

Where $I_{LA\,\{CAD=M\}}\,(X,Z)$ represents the light attenuation correction field, $\overline{< I_{TC\,\{CAD=M\}}\,(Z) >}$ is the average of the signal intensity over the X-direction for the pixels at Z in the ensemble-average LIF image after the tracer concentration correction, and $\overline{< I_{TC\,\{CAD=M\}}(Z_o) >}$ is the average of the signal intensity over the X-direction for the pixels at Z_o. The light attenuation correction field is first evaluated for $-8 \le Z \le -2$ to avoid the effect of any LIF structures near solid surfaces or vignetting. Then, $I_{LA\,\{CAD=M\}}\,(X,Z)$ is extrapolated for regions near solid surfaces using an exponential fit. The light attenuation correction is applied to the ensemble-average LIF image after the tracer concentration correction using the equation (A-6),

$$I_{LA\,corrected\,\{CAD=M\}}\,(X,Z) = \frac{< I_{TC\,\{CAD=M\}}\,(X,Z) >}{I_{LA\,\{CAD=M\}}(X,Z)} \qquad \text{(A-6)}$$

Where $I_{LA\,corrected}\,(X,Z)$ represents the ensemble-average LIF image after the light attenuation correction, $< I_{TC\,\{CAD=M\}}\,(X,Z) >$ is the ensemble-average LIF image after the tracer concentration correction, and $I_{LA\,\{CAD=M\}}(X,Z)$ is the light attenuation correction field.

Secondly, the laser beam profile is examined by evaluating the fluctuations in the signal intensity along the light sheet width in the X-direction. The laser beam profile correction field at each specific CAD can be determined by inspecting the ensemble average LIF image after the light attenuation correction using equation (A-7),

$$I_{LF\ \{CAD=M\}}\ (X,Z) = \frac{\overline{I_{LA\ corrected\ \{CAD=M\}}\ (X)}}{\max(\overline{I_{LA\ corrected\ \{CAD=M\}}\ (X)})}, -8 \le Z \le -2 \qquad \text{(A-7)}$$

Where $I_{LF\ \{CAD\ \ \}}\ (X,Z)$ represents the laser fluence correction field, $\overline{I_{LA\ corrected\ \{CAD=M\}}\ (X)}$ is the average of the signal intensity over the Z-direction for the pixels at X in the ensemble-average LIF image after the light attenuation correction, and $\max(\overline{I_{LA\ corrected\ \{CAD=M\}}\ (X)})$ is the maximum value of $\overline{I_{LA\ corrected\ \{CAD\ \ \}}\ (X)}$. The laser fluence correction field is first evaluated for $-8 \le Z \le -2$, then $I_{LA\ \{CAD=M\}}\ (X,Z)$ is elongated in the Z-direction to include the regions near solid surfaces. The laser fluence correction can be applied to the ensemble-average LIF image using the equation (A-6),

$$I_{LF\ corrected\ \{CAD=M\}}\ (X,Z) = \frac{I_{LA\ corrected\ \{CAD=M\}}\ (X,Z)}{I_{LF\ \{CAD=M\}}(X,Z)} \qquad \text{(A-6)}$$

Where $I_{LF\ corrected\ \{CAD=M\}}\ (X,Z)$ represents the ensemble-average LIF image after the laser fluence correction, $I_{LA\ corrected\ \{CAD=M\}}\ (X,Z)$ is the ensemble-average LIF image after the light attenuation correction, and $I_{LF\ \{CAD=M\}}(X,Z)$ is the laser fluence correction field.

Finally, any vertical strips that become apparent as a result from the previous correction steps are examined, similarly to the laser beam profile, by evaluating the fluctuations in the signal intensity in the X-direction. The vertical strips correction field at each specific CAD can be determined by inspecting the ensemble-average LIF image after the laser fluence correction using equation (A-8),

$$I_{VS\ \{CAD=M\}}\ (X,Z) = \frac{\overline{I_{LF\ corrected\ \{CAD=M\}}\ (X)}}{\max(\overline{I_{LF\ corrected\ \{CAD=M\}}\ (X)})}, -8 \le Z \le -2 \qquad \text{(A-8)}$$

Where $I_{VS\ \{CAD=M\}}\ (X,Z)$ represents the ensemble-average LIF image after the vertical strips correction, $\overline{I_{LF\ corrected\ \{CAD=M\}}\ (X)}$ is the average of the signal intensity over the Z-direction for the pixels at X in the ensemble-average LIF image after the laser fluence correction, and $\max(\overline{I_{LF\ corrected\ \{CAD=M\}}\ (X)})$ is the maximum value of $\overline{I_{LF\ corrected\ \{CAD=M\}}\ (X)}$. The image processing procedure for deriving these correction fields for 0 CAD is illustrated in Figure A-5.

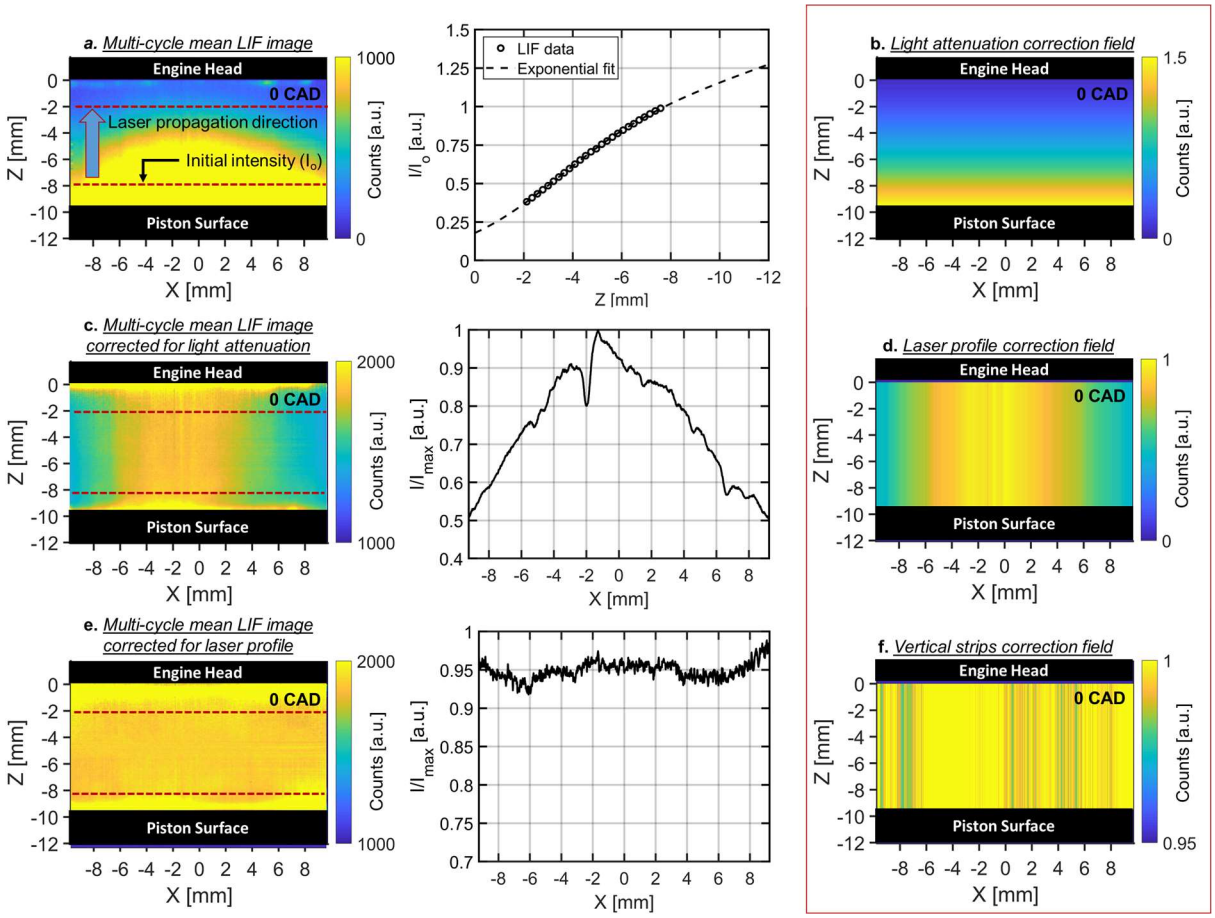

Figure A- 5. Image processing procedure for deriving the correction fields of the MSC method at 0 CAD. Each line plot is extracted from the image to its left, and is used to determine the correction field to its right.

Then, the instantaneous LIF image after the tracer concentration correction, is corrected using the multi-step correction (MSC) method according to equation (A-10),

$$I_{Corrected,MSC\,\{CAD=M,Cycle=N\}}\,(X,Z) = \frac{I_{TC\,\{CAD\quad,Cycle\quad\}}\,(X,Z)}{I_{LA\,\{CAD=M\}}\,(X,Z)\;\;I_{LF\,\{CAD=M\}}(X,Z)\;\;I_{VS\,\{CAD=M\}}\,(X,Z)} \tag{A-10}$$

Where $I_{Corrected,MSC\,\{CAD\quad,Cycle\quad\}}\,(X,Z)$ represents the corrected instantaneous LIF image using the MSC method, $I_{TC\,\{CAD=M,Cycle=N\}}\,(X,Z)$ is the instantaneous LIF image after the tracer concentration correction, $I_{LA\,\{CAD=M\}}\,(X,Z)$ is the light attenuation correction field, $I_{LF\,\{CAD=M\}}(X,Z)$ is the laser fluence correction field, and $I_{VS\,\{CAD=M\}}\,(X,Z)$ is the vertical strips correction field. The image processing procedure for the MSC method is illustrated in Figure A-6 for an instantaneous LIF

image at 0 CAD from cycle 7. The instantaneous LIF image at 0 CAD in Fig. A-5.a is normalized by the correction fields for light attenuation, laser profile, and vertical strips shown in Fig. A-6.b1-3 to yield the corrected instantaneous LIF image at 0 CAD shown in Fig. A-6.c. Each instantaneous LIF image at 0 CAD is normalized by the same correction fields, and the procedure is repeated for all other recorded CADs.

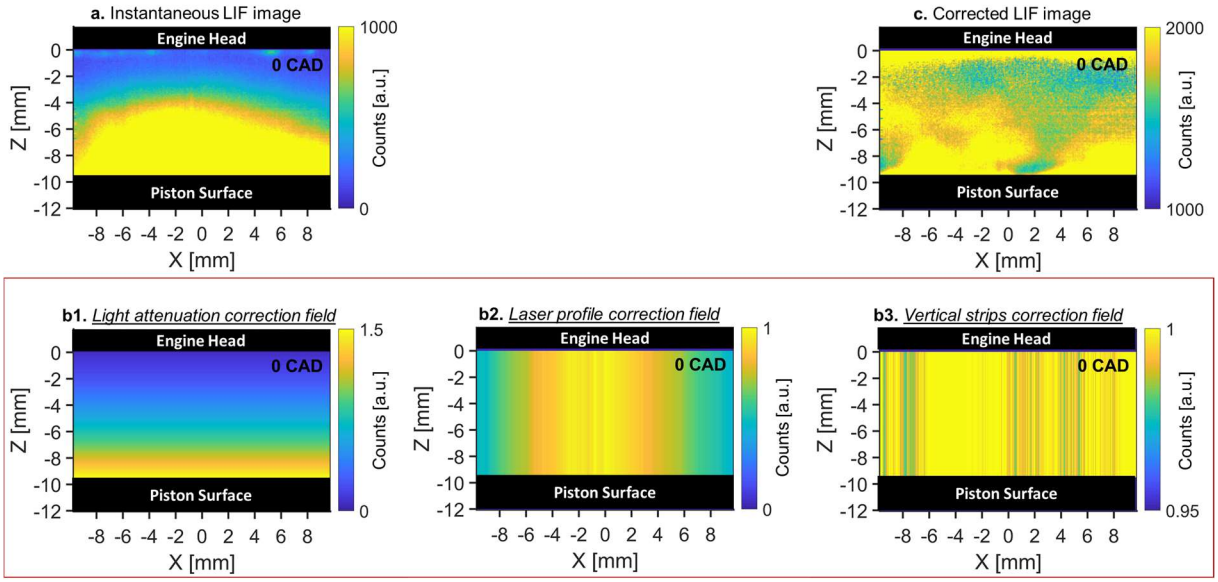

Figure A- 6. Image processing procedure using the MSC method for an instantaneous LIF image at 0 CAD from cycle 7.

Bibliography

1. Dec, J.E., *Advanced compression-ignition engines—understanding the in-cylinder processes.* Proceedings of the Combustion Institute, 2009. **32**(2): p. 2727-2742.
2. Krishnamoorthi, M., R. Malayalamurthi, Z. He, and S. Kandasamy, *A review on low temperature combustion engines: Performance, combustion and emission characteristics.* Renewable and Sustainable Energy Reviews, 2019. **116**: p. 109404.
3. Fathi, M., O. Jahanian, and M. Shahbakhti, *Modeling and controller design architecture for cycle-by-cycle combustion control of homogeneous charge compression ignition (HCCI) engines – A comprehensive review.* Energy Conversion and Management, 2017. **139**: p. 1-19.
4. Wang, Y., F. Xiao, Y. Zhao, D. Li, and X. Lei, *Study on cycle-by-cycle variations in a diesel engine with dimethyl ether as port premixing fuel.* Applied Energy, 2015. **143**: p. 58-70.
5. Zhao, F., *Homogeneous charge compression ignition (HCCI) engines: key research and development issues*. HCCI engines :key research and development issues. 2003, Warrendale, Pa.: Society of Automotive Engineers. ix, 658 p.
6. Persson, H., L. Hildingsson, A. Hultqvist, B. Johansson, and J. Ruebel, *Investigation of Boundary Layer Behaviour in HCCI Combustion using Chemiluminescence Imaging*. 2005.
7. Dec, J.E. and W. Hwang, *Characterizing the Development of Thermal Stratification in an HCCI Engine Using Planar-Imaging Thermometry.* SAE International Journal of Engines, 2009. **2**(1): p. 421.
8. Sjöberg, M., J.E. Dec, A. Babajimopoulos, and D.N. Assanis, *Comparing Enhanced Natural Thermal Stratification Against Retarded Combustion Phasing for Smoothing of HCCI Heat-Release Rates*. 2004.
9. McIlroy, A., G. McRae, V. Sick, D. L. Siebers, C.K. Westbrook, P. J. Smith, C. Taatjes, A. Trouve, A. F. Wagner, E. Rohlfing, D. Manley, F. Tully, R. Hilderbrandt, W. Green, D. Marceau, J. O'Neal, M. Lyday, F. Cebulski, T. R. Garcia, and D. Strong, *Basic Research Needs for Clean and Efficient Combustion of 21st Century Transportation Fuels*. 2006.
10. Chang, O. Guralp, Z. Filipi, D.N. Assanis, T.W. Kuo, and P. Najt, *New heat transfer correlation for an HCCI engine derived from measurements of instantaneous surface heat flux.* SAE Paper 2004-01-2996, 2004.
11. Farrell, J.T., J.G. Stevens, and W. Weissman, *A Second Law Analysis of High Efficiency Low Emission Gasoline Engine Concepts.* SAE Technical Papers, 2006.
12. Borman, G. and K. Nishiwaki, *Internal-combustion engine heat transfer.* Progress in Energy and Combustion Science, 1987. **13**(1): p. 1-46.
13. Dec, J.E., M.L. Davisson, M. Sjöberg, R.N. Leif, and W. Hwang, *Detailed HCCI Exhaust Speciation and the Sources of Hydrocarbon and Oxygenated Hydrocarbon Emissions.* SAE International Journal of Fuels and Lubricants, 2009. **1**(1): p. 50.

14. Heywood, J.B., *Internal combustion engine fundamentals*. Vol. 930. 1988: Mcgraw-hill New York.
15. Lumley, J.L., *Engines, An Introduction.* 1999.
16. *READER'S Digest Complete Car Care Manual*. 1981, The Christian Science Publishing Society. p. 16.
17. Heywood, J.B., *Internal combustion engine fundamentals*. 1988, United States: McGraw-Hill Book Company.
18. Michael, F.M. and C.H. Daniel, *Radiative Heat Transfer in Turbulent Combustion Systems*. 2016, Springer: Cham.
19. Pulkrabek, W.W., *Engineering fundamentals of the internal combustion engine*. 2004, Upper Saddle River, N.J.: Pearson Prentice Hall. xxiii, 478 p.
20. Bergman, T.L. and F.P. Incropera, *Fundamentals of heat and mass transfer*. 2011, Hoboken, NJ: John Wiley. xxiii, 1048 p.
21. Kundu, P.K., I.M. Cohen, D.R. Dowling, G. Tryggvason, and ScienceDirect, *Fluid mechanics*. Sixth edition. ed. Vol. Amsterdam ; Boston :. 2016, Amsterdam ; Boston :: Elsevier/AP.
22. Frei, W., *Which Turbulence Model Should I Choose for My CFD Application?*, in *COMSOL BLOG*. 2017.
23. Dewan, A., *Tackling turbulent flows in engineering*. 2011, Berlin, Heidelberg: Springer.
24. Pierce, J.B. Ghandhi, and J.K. Martin, *Near-Wall Velocity Characteristics in Valved and Ported Motored Engines.* SAE Paper 920152, 1992.
25. Alharbi, A. and V. Sick, *Investigation of Boundary Layer in Internal Combustion Engines using High-Speed Micro-PIV.* 6th U.S. National Combustion Meeting, 2009.
26. Jainski, C., L. Lu, A. Dreizler, and V. Sick, *High-speed micro particle image velocimetry studies of boundary-layer flows in a direct-injection engine.* International Journal of Engine Research, 2013. **14**(3): p. 247-259.
27. Greene, M.L. and E. University of Michigan. Mechanical, *Momentum Near-wall Region Characterization in a Reciprocating Internal-combustion Engine*. Vol. Ann Arbor :. 2017, Ann Arbor :: ProQuest Dissertations & Theses.
28. Angioletti, M., R.M. Di Tommaso, E. Nino, and G. Ruocco, *Simultaneous visualization of flow field and evaluation of local heat transfer by transitional impinging jets.* International Journal of Heat and Mass Transfer, 2003. **46**(10): p. 1703-1713.
29. Loureiro, J.B.R. and A.P.S. Freire, *Velocity and temperature profiles, wall shear stress and heat transfer coefficient of turbulent impinging jets.* International Journal of Heat and Mass Transfer, 2017. **107**: p. 846-861.
30. Guerra, D.R.S., J. Su, and A.P.S. Freire, *The near wall behavior of an impinging jet.* International Journal of Heat and Mass Transfer, 2005. **48**(14): p. 2829-2840.
31. Lienhard, J.H. *Heat Transfer by Impingement of Circular Free-Surface Liquid Jets*. 2005.
32. Torregrosa, A.J., P.C. Olmeda, and C.A. Romero, *Revising engine heat transfer.* Journal of Engineering Annals of Faculty of Engineering Hunedoara, 2008. **6**(3): p. 245-265.
33. Janeway, R., *Interpretation of the Indicator Card.* SAE International, 1929. **24**: p. 92-101.
34. Janeway, R., *Quantitative Analysis of Heat Transfer in Engines.* SAE International 380163, 1938. **2008**: p. 04-15.
35. Lanchester, F., *The Energy Balance Sheet of the Internal Combustion Engine.* Proceedings of the Institution of Mechanical Engineers, 1939. **141**(1): p. 289-338.

36. Eichelberg, G., *Some new investigations on old combustion engine problems.* Engineering, 1939. **148**(27): p. 463-466.
37. Pflaum, W., *Wärmeübergang bei Dieselmaschinen mit und ohne Aufladung.* M.T.Z., 1961. **22**: p. 70.
38. Eichelberg, G. and W. Pflaum, *Untersuchung eines hochaufgeladenen Dieselmotors.* Z. Ver. dtsch. Ing., 1951. **93**: p. 1113.
39. Annand, W.J., *Heat transfer in the cylinder of reciprocating internal engines.* Proc. Instn Mech. Engrs., 1963. **173**(36): p. 973-990.
40. Elser, K., *Der instationäre Wämeübergang in Diesel-motoren.* Mitt. Inst. Thermodyn. Zürich, 1954. **15**.
41. Taylor, C., *Heat Transmission in Internal-Combustion Engines.* Proc., General Discussion on Heat Transfer, Inst. Mech. Engrs., London, 1951: p. 397.
42. Taylor, C.F. and T.Y. Toong, *Heat transfer in Internal combustion engines.* ASME paper 57-HT-17, 1957.
43. Oguri, T., *On the coefficient of heat transfer between gases and cylinder walls of the spark-ignition engine.* Bulletin of JSME, 1960. **3**(11): p. 363-369.
44. Overbye, V., J. Bennethum, O. Uyehara, and P. Myers, *Unsteady heat transfer in engines.* SAE Trans, 1961. **69**(461).
45. Williams, T., *Some applications of DEUCE to Diesel Engine Design.* The Engineer, 1960. **27**: p. 60.
46. McAulay, K., T. Wu, S. Chen, G. Borman, P.S. Myers, and O.A. Uyehara, *Development and evaluation of the simulation of the compression-ignition engine.* SAE Paper 650451, 1965.
47. Chirkov, A.A. and B.S. Stefanovski, *О доминирующем способе передачи тепла в цилиндрах двигателей внутреннего сгорания.* Trudy Rostovskova Instituta Injyenyerov Fyelyeznodorovnova Transporta, 1958. **21**.
48. Zipkin, M.A. and J. Sanders, *Correlation of Exhaust-Valve Temperatures with Engine Operating Conditions and Valve Design*. 1945, DTIC Document.
49. Ku, P.M., *Factors Affecting Heat Transfer in the Internal-Combustion Engine*. 1940, DTIC Document.
50. Woschni, G., *A universally applicable equation for the instantaneous heat transfer coefficient in the internal combustion engine.* Significance, 1967. **2012**: p. 12-11.
51. Woschni, G.J., *Die Berechnung der Wandverluste und der Thermischen Belastung der Bauteile von Dieselmotoren.* Motortechnishe Zeitschrift, 1970. **30**(12): p. 491-499.
52. Hohenberg, G.F., *Advanced Approaches for Heat Transfer Calculations.* SAE Paper 790825, 1979.
53. Annand and T.H. Ma, *Instantaneous heat transfer rates to the cylinder head surface of a small compression-ignition engine.* Proc. IMechE, Part D: J. Autom. Eng, 1971. **185**: p. 976–987.
54. LeFeuvre, P.S. Myers, and O.A. Uyehara, *Experimental instantaneous heat fluxes in a Diesel engine and their correlations.* SAE-Paper 690464, 1970.
55. Borgnakke, C., V.S. Arpaci, and R.J. Tabaczynski, *A model for the instantaneous heat transfer and turbulence in a spark ignition engine.* Combustion, 1980. **2012**: p. 06-06.
56. Poulos, S.G. and J.B. Heywood, *The effect of chamber geometry on spark-ignition engine combustion.* SAE Paper 830334, 1983.

57. Alkidas, A., P. Puzinauskas, and R. Peterson, *Combustion and heat transfer studies in a spark-ignited multivalve optical engine.* Training, 1990. **2013**: p. 11-11.
58. Lancaster, D.R., *Effects of engine variables on turbulence in a spark-ignition engine*. 1976.
59. Witze, P.O., *Measurements of the spatial distribution and engine speed dependence of turbulent air motion in an ic engine.* 1977.
60. Nijeweme, D.J.O., J.B.W. Kok, C.R. Stone, and L. Wyszynski, *Unsteady in-cylinder heat transfer in a spark ignition engine: experiments and modelling.* Proceedings of the Institution of Mechanical Engineers Part D-Journal of Automobile Engineering, 2001. **215**(D6): p. 747-760.
61. Alkidas, A.C., *Heat Transfer Characteristics of a Spark-Ignition Engine.* Journal of Heat Transfer, 1980. **102**: p. 189-193.
62. Cho, K., D. Assanis, Z. Filipi, G. Szekely, P. Najt, and R. Rask, *Experimental investigation of combustion and heat transfer in a direct-injection spark ignition engine via instantaneous combustion chamber surface temperature measurements.* Proceedings of the Institution of Mechanical Engineers, Part D: Journal of Automobile Engineering, 2008. **222**(11): p. 2219-2233.
63. Soyhan, H., H. Yasar, H. Walmsley, B. Head, G. Kalghatgi, and C. Sorusbay, *Evaluation of heat transfer correlations for HCCI engine modeling.* Applied Thermal Engineering, 2009. **29**(2): p. 541-549.
64. Rakopoulos, C., G. Kosmadakis, and E. Pariotis, *Critical evaluation of current heat transfer models used in CFD in-cylinder engine simulations and establishment of a comprehensive wall-function formulation.* Applied Energy, 2010. **87**(5): p. 1612-1630.
65. Launder, B.E. and D. Spalding, *The numerical computation of turbulent flows.* Computer methods in applied mechanics and engineering, 1974. **3**(2): p. 269-289.
66. Huh, K.Y., I.-P. Chang, and J.K. Martin, *A comparison of boundary layer treatments for heat transfer in IC engines*. 1990, SAE Technical Paper.
67. Angelberger, C., T. Poinsot, and B. Delhay, *Improving near-wall combustion and wall heat transfer modeling in SI engine computations*. 1997, SAE Technical Paper.
68. Han, Z. and R.D. Reitz, *A temperature wall function formulation for variable-density turbulent flows with application to engine convective heat transfer modeling.* Int. J. Heat and Mass Transfer, 40(3), 613-625, 1997., 1997. **40**(3): p. 613-625.
69. Yang, J., P. Pierce, J.K. Martin, and D.E. Foster, *Heat transfer predictions and experiments in a motored engine*. 1988, SAE Technical Paper.
70. Nijeweme, D.O., J. Kok, C. Stone, and L. Wyszynski, *Unsteady in-cylinder heat transfer in a spark ignition engine: experiments and modelling.* Proceedings of the Institution of Mechanical Engineers, Part D: Journal of Automobile Engineering, 2001. **215**(6): p. 747-760.
71. Lawton, B., *Effect of compression and expansion on instantaneous heat transfer in reciprocating internal combustion engines.* Proceedings of the Institution of Mechanical Engineers, Part A: Journal of Power and Energy, 1987. **201**(3): p. 175-186.
72. Dao, K., O. Uyehara, and P. Myers, *Heat transfer rates at gas-wall interfaces in motored piston engine*. 1973, SAE Technical Paper.
73. Lawton, B., *Effect of Compression and Expansion on Instantaneous Heat-Transfer in Reciprocating Internal-Combustion Engines.* Proceedings of the Institution of Mechanical Engineers Part a-Journal of Power and Energy, 1987. **201**(3): p. 175-186.

74. Reuss, D.L., T.W. Kuo, G. Silvas, V. Natarajan, and V. Sick, *Experimental metrics for identifying origins of combustion variability during spark-assisted compression ignition.* International Journal of Engine Research, 2008. **9**(5): p. 409-434.
75. Asanuma, T. and T. Obokata, *Gas velocity measurements of a motored and firing engine by laser anemometry.* SAE Technical Paper 790096, 1979.
76. Rask, R.B., *Laser Doppler anemometer measurements in an internal combustion engine.* SAE Paper 790094, 1979.
77. Cole, J. and M. Swords, *An investigation of the ignition process in a lean-burning engine using conditionally sampled laser-doppler anemometry.* SAE Paper 800043, 1980.
78. Liou, T.-m., M. Hall, D. Santavicca, and F. Bracco, *Laser doppler velocimetry measurements in valved and ported engines.* Training, 1984. **2014**: p. 04-07.
79. Fansler, T.D., *Laser velocimetry measurements of swirl and squish flows in an engine with a cylindrical piston bowl.* SAE Technical Paper 850124, 1985.
80. Hall, M. and F.V. Bracco, *Cycle-Resolved Velocity and Turbulence Measurements Near the Cylinder of a Firing S. I. Engine.* SAE Paper 861530, 1986.
81. Foster, D. and P.O. Witze, *Velocity Measurements in the Wall Boundary Layer of a Spark-Ignited Research Engine.* SAE Paper 872105, 1987.
82. Greene, M.L., *Momentum Near-wall Region Characterization in a Reciprocating Internal-combustion Engine*. 2017, ProQuest Dissertations Publishing.
83. Chen, C. and A. Veshagh, *A one-dimensional model for in-cylinder heat convection based on the boundary layer theory.* Safety, 1992. **2012**: p. 03-21.
84. Franco, A. and L. Martorano, *Evaluations on the Heat Transfer in the Small Two-stroke Engines*. 1998, SAE International.
85. Suzuki, T., Y. Oguri, and M. Yoshida, *Heat Transfer in the Internal Combustion Engines*. 2000, SAE International.
86. Fiveland, S.B. and D.N. Assanis, *Development of a Two-Zone HCCI Combustion Model Accounting for Boundary Layer Effects*. 2001, SAE International.
87. Schmitt, M., C.E. Frouzakis, Y.M. Wright, A.G. Tomboulides, and K. Boulouchos, *Direct numerical simulation of the compression stroke under engine-relevant conditions: Evolution of the velocity and thermal boundary layers.* International Journal of Heat and Mass Transfer, 2015. **91**: p. 948.
88. Ma, P.C., T. Ewan, C. Jainski, L. Lu, A. Dreizler, V. Sick, and M. Ihme, *Development and Analysis of Wall Models for Internal Combustion Engine Simulations Using High-speed Micro-PIV Measurements.* Flow, Turbulence and Combustion, 2016: p. 1.
89. Ma, P.C., M. Greene, V. Sick, and M. Ihme, *Non-equilibrium wall-modeling for internal combustion engine simulations with wall heat transfer.* International Journal of Engine Research, 2017. **18**(1-2): p. 15.
90. Lyford-Pike, E.J. and J.B. Heywood, *Thermal boundary layer thickness in the cylinder of a spark-ignition engine.* International Journal of Heat and Mass Transfer, 1984. **27**(10): p. 1873-1878.
91. Lucht, R.P. and M.A. Maris, *CARS measurements of temperature profiles near a wall in an internal combustion engine.* SAE paper 870459, 1987: p. Medium: X; Size: Pages: 7.
92. Lucht, D. Dunn-Rankin, T. Walter, T. Dreier, and S.C. Bopp, *Heat Transfer in Engines: Comparison of CARS Thermal Boundary Layer Measurements and Heat Flux Measurements.* SAE Paper 910722, 1991.

93. Einecke, S., C. Schulz, and V. Sick, *Measurement of temperature, fuel concentration and equivalence ratio fields using tracer LIF in IC engine combustion.* Applied Physics B Lasers and Optics, 2000. **71**(5): p. 717.
94. Snyder, J., N. Dronniou, J.E. Dec, and R. Hanson, *PLIF Measurements of Thermal Stratification in an HCCI Engine under Fired Operation.* SAE International Journal of Engines, 2011. **4**(1): p. 1669.
95. Dronniou, N. and J.E. Dec, *Investigating the Development of Thermal Stratification from the Near-Wall Regions to the Bulk-Gas in an HCCI Engine with Planar Imaging Thermometry.* SAE International Journal of Engines, 2012. **5**(3): p. 1046.
96. Kaiser, S.A., M. Schild, and C. Schulz. *Thermal stratification in an internal combustion engine due to wall heat transfer measured by laser-induced fluorescence*. in *Proc. Combust. Inst.* 2013. NEW YORK: ELSEVIER SCIENCE INC.
97. Peterson, B., E. Baum, B. Böhm, V. Sick, and A. Dreizler. *High-speed PIV and LIF imaging of temperature stratification in an internal combustion engine*. in *Proc. Combust. Inst.* 2013.
98. Cundy, M.E. and V. Sick, *An approach to identify boundary layer temperature field structures in internal combustion engines*, in *CI/CS Spring Technical Meeting*. 2012. p. Paper # 02-001.
99. Luo, X., X. Yu, K. Zha, M. Jansons, and V. Soloiu, *In-Cylinder Wall Temperature Influence on Unburned Hydrocarbon Emissions During Transitional Period in an Optical Engine Using a Laser-Induced Phosphorescence Technique*. 2014, SAE International.
100. Luo, X., X. Yu, and M. Jansons, *Simultaneous In-Cylinder Surface Temperature Measurements with Thermocouple, Laser-induced Phosphorescence, and Dual Wavelength Infrared Diagnostic Techniques in an Optical Engine*. 2015, SAE International.
101. Sick, V., *High speed imaging in fundamental and applied combustion research.* Proceedings of the Combustion Institute, 2013. **34**(2): p. 3509-3530.
102. Orth, A., V. Sick, J. Wolfrum, R.R. Maly, and M. Zahn, *Simultaneous 2D single-shot imaging of oh concentrations and temperature fields in an si engine simulator.* Symposium (International) on Combustion, 1994. **25**(1): p. 143.
103. Kranendonk, L.A., A.W. Caswell, C.L. Hagen, C.T. Neuroth, D.T. Shouse, J.R. Gord, and S.T. Sanders, *Temperature Measurements in a Gas-Turbine-Combustor Sector Rig Using Swept-Wavelength Absorption Spectroscopy.* Journal of Propulsion and Power, 2009. **25**(4): p. 859.
104. Lucht, R.P. and M.A. Maris, *CARS Measurements of Temperature Profiles Near a Wall in an Internal Combustion Engine*. 1987.
105. Dronniou, N. and J. Dec, *Investigating the Development of Thermal Stratification from the Near-Wall Regions to the Bulk-Gas in an HCCI Engine with Planar Imaging Thermometry.* SAE Paper 2012-01-1111, 2012.
106. Miller, V.A., *High-speed tracer-based PLIF imaging for scramjet ground testing*. 2014, Stanford University.
107. Schulz, C. and V. Sick, *Tracer-LIF Diagnostics: Quantitative Measurement of fuel concentration, temperature and fuel/air ratio in practical combustion systems.* Prog. Energy Combust. Science, 2005. **31**: p. 75-121.

108. Peterson, B., E. Baum, B. Böhm, V. Sick, and A. Dreizler, *Evaluation of toluene LIF thermometry detection strategies applied in an internal combustion engine.* Applied Physics B, 2014. **117**(1): p. 151.
109. Luong, M., R. Zhang, C. Schulz, and V. Sick, *Toluene Laser-Induced Fluorescence for in-Cylinder Temperature Imaging in Internal Combustion Engines.* 2008.
110. Cundy, M., P. Trunk, A. Dreizler, and V. Sick, *Gas-phase toluene LIF temperature imaging near surfaces at 10 kHz.* Experiments in Fluids, 2011. **51**(5): p. 1169-1176.
111. Faust, S., M. Goschutz, S.A. Kaiser, T. Dreier, and C. Schulz, *A comparison of selected organic tracers for quantitative scalar imaging in the gas phase via laser-induced fluorescence.* Applied Physics B-Lasers and Optics, 2014. **117**(1): p. 183-194.
112. Schulz, C. and V. Sick, *Tracer-LIF diagnostics: quantitative measurement of fuel concentration, temperature and fuel/air ratio in practical combustion systems.* Progress in Energy and Combustion Science, 2005. **31**(1): p. 75-121.
113. Schiffmann, P., S. Gupta, D. Reuss, V. Sick, X. Yang, and T.W. Kuo, *TCC-III Engine Benchmark for Large-Eddy Simulation of IC Engine Flows.* Oil & Gas Science and Technology-Revue D Ifp Energies Nouvelles, 2016. **71**(1): p. 3.
114. Lichtl, M., *Aufbau und Einsatz eines laserin-duzierten Fluoreszenzmessverfah-rens für Temperaturfeldmessun-gen in einem optischen Motor*. 2014, Hochschule Darmstadt – University of Applied Sciences.
115. Dronniou, N. and J. Dec, *Investigating the Development of Thermal Stratification from the Near-Wall Regions to the Bulk-Gas in an HCCI Engine with Planar Imaging Thermometry.* SAE Technical Papers 2012-01-1111, 2012. **5**(3): p. 1046.
116. Peterson, B., E. Baum, B. Bohm, V. Sick, and A. Dreizler, *Evaluation of toluene LIF thermometry detection strategies applied in an internal combustion engine.* Applied Physics B-Lasers and Optics, 2014. **117**(1): p. 151-175.
117. Kaiser, S.A., M. Schild, and C. Schulz, *Thermal stratification in an internal combustion engine due to wall heat transfer measured by laser-induced fluorescence.* Proceedings of the Combustion Institute, 2013. **34**(2): p. 2911-2919.
118. Cierpka, C., S. Scharnowski, and C.J. Kähler, *Parallax correction for precise near-wall flow investigations using particle imaging.* Applied Optics, 2013. **52**(12): p. 2923-2931.
119. Greene, M.L., *Momentum Near-wall Region Characterization in a Reciprocating Internal-combustion Engine*. 2017, University of Michigan: Ann Arbor, Michigan, USA.
120. Peterson, B., E. Baum, B. Böhm, V. Sick, and A. Dreizler, *Evaluation of toluene LIF thermometry detection strategies applied in an internal combustion engine.* Applied Physics B, 2014. **117**(1): p. 151-175.
121. Frieden, D. and V. Sick, *Investigation of the fuel injection, mixing and combustion processes in an SIDI engine using Quasi-3D LIF imaging.* SAE Technical Papers, 2003.
122. Schiffmann, P., D.L. Reuss, and V. Sick, *Empirical investigation of spark-ignited flame-initiation cycle-to-cycle variability in a homogeneous charge reciprocating engine.* International Journal of Engine Research. **19**(5): p. 491-508.
123. Wu, A., S. Keum, and V. Sick, *Large Eddy Simulations with Conjugate Heat Transfer (CHT) modeling of Internal Combustion Engines (ICEs).* Oil & Gas Science and Technology – Revue d'IFP Energies nouvelles, 2019. **74**: p. 51.
124. Schmitt, M., C.E. Frouzakis, A.G. Tomboulides, Y.M. Wright, and K. Boulouchos, *Direct numerical simulation of the effect of compression on the flow, temperature and composition*

under engine-like conditions. Proceedings of the Combustion Institute, 2015. **35**(3): p. 3069-3077.
125. Ma, P.C., M. Greene, V. Sick, and M. Ihme, *Non-equilibrium wall-modeling for internal combustion engine simulations with wall heat transfer.* International Journal of Engine Research. **18**(1-2): p. 15-25.
126. Schmitt, M., C.E. Frouzakis, A.G. Tomboulides, Y.M. Wright, and K. Boulouchos. *Direct numerical simulation of the effect of compression on the flow, temperature and composition under engine-like conditions*. in *Proc. Combust. Inst.* 2015. NEW YORK: Elsevier Inc.
127. MacDonald, J.R., C.M. Fajardo, M. Greene, D. Reuss, and V. Sick, *Two-Point Spatial Velocity Correlations in the Near-Wall Region of a Reciprocating Internal Combustion Engine.* SAE Technical Paper 2017-01-0613, 2017. **1**(March).
128. Snyder, J., N. Dronniou, J.E. Dec, and R. Hanson, *PLIF Measurements of Thermal Stratification in an HCCI Engine under Fired Operation.* SAE Journal Article 2011-01-1291, 2011. **4**(1): p. 1669.
129. Funk, V. Sick, D.L. Reuss, and W.J.A. Dahm, *Turbulence Properties of high and low swirl in-cylinder flows.* SAE Technical Paper 2002-01-2841, 2002.
130. Schmitt, M., C.E. Frouzakis, Y.M. Wright, A.G. Tomboulides, and K. Boulouchos, *Investigation of wall heat transfer and thermal stratification under engine-relevant conditions using DNS.* International Journal of Engine Research, 2015. **17**(1): p. 63-75.
131. Schmitt, M., *Direct numerical simulations in engine-like geometries*. 2014, ETH Zürich.